COMPARISON OF DIFFERENT COATING PROPERTIES IN BEARING BY USING VIBRATION ANALYSIS

Thesis Submitted for the Award of the Degree of

DOCTOR OF PHILOSOPHY

in

Mechanical Engineering

By

Rameshwar Cambow

Registration Number: 41700146

Supervised By

Dr. Manpreet Singh (20360)

Department of Mechanical engineering (Professor)

Lovely Professional University

LOVELY PROFESSIONAL UNIVERSITY, PUNJAB

2024

DECLARATION

I, hereby declared that the presented work in the thesis entitled "Comparison of different coating properties in bearing by using vibration analysis" in fulfilment of degree of **Doctor of Philosophy (Ph. D.)** is outcome of research work carried out by me under the supervision of Dr. Manpreet Singh, working as Professor in the School of Mechanical engineering of Lovely Professional University, Punjab, India. In keeping with general practice of reporting scientific observations, due acknowledgements have been made whenever work described here has been based on findings of other investigator. This work has not been submitted in part or full to any other University or Institute for the award of any degree.

(Signature of Scholar)

Name of the scholar: Rameshwar Cambow

Registration No.: 41700146

Department/school: School of Mechanical engineering

Lovely Professional University,

Punjab, India

CERTIFICATE

This is to certify that the work reported in the Ph. D. thesis entitled "Comparison of different coating properties in bearing by using vibration analysis" submitted in fulfillment of the requirement for the reward of degree of **Doctor of Philosophy (Ph.D.)** in the School of Mechanical engineering , is a research work carried out by Rameshwar Cambow, 41700146, is bonafide record of his/her original work carried out under my supervision and that no part of thesis has been submitted for any other degree, diploma or equivalent course.

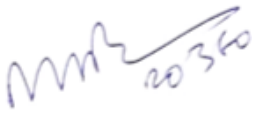

(Signature of Supervisor)

Name of supervisor: Dr. Manpreet Singh

Designation: Professor

Department/school: CAD/CAM & Mechatronics

University: Lovely Professional University

Abstract

Machines have significantly impacted the life of mankind. In a journey from stone age to Industry 4.0 in second decade of 21st century, machines have enrichened the human life in various technological aspects. With the rise in population, in turn demand, it was almost impossible to cater the needs of all without the development of industrial machines. That is why, it is getting difficult to afford the failure of machines with its rising dependency. To tackle this situation, researchers around the world developed several monitoring techniques and refined the concept of "condition monitoring" in Industry 4.0. As far as failures in the machines are concerned, mostly it occurs due to loss of usefulness of critical components like bearings, gears or transmission elements. In this work, a ball bearing is considered for research work. Although, several attempts have been made since decades by various manufacturers to improve the life of bearing by heat treatments, induction of alloys and coating for high-speed applications. Moreover, numerous techniques were also developed to monitor the condition of the running bearing based on several parameters like noise, temperature, and vibration. However, vibration signature analysis found to be preferred choice of many researchers since long for condition monitoring of bearing. But in all these methods of condition monitoring, indication of fault occurs after the origin of fault hence post failure. Though, any type of failure does not grow in fraction of time. Before failure, it is obvious that degradation in material properties must get initiated at micro level, then with continuous operation of machines under same load and conditions, material properties continue to deteriorate which get mature and leads to fault. However, traditional methods used to measure the level of these properties needs dismantling of the bearing followed by disassembly of bearing races to analyze load bearing area of the bearing, which is impractical in nature. In view of this, in this research work, an attempt has been made to develop a technique to monitor the degradation in level of material characteristics based on vibration signal analysis. As with continuous deterioration, vibration of the material bound to change at the micro level. Therefore, by continuous monitoring of its vibration signal, it would be possible to know the initiation of failure at very much incipient stage. It would also assist several researchers to calculate the remaining useful of life of the bearing accurately. Based on this approach, in this research work, five ball bearings (Model: 6205) have been considered

as its one of the widely used model for high speeds. These five bearings were coated with five different materials (Copper, Silver, Zinc Phosphate and Black Oxide) having different level of material properties. Selection of coating material has been done based on the catalogue of bearing manufacturers [11,42]. Based on manufacturer specifications in the catalogue, coating procedure has been carried out on all five bearings as per industrial standards. Additionally, these coating has been carried out on loose samples also, taken as per ASTM standards to evaluate the level of different properties of coated material. Moreover, five different properties of coatings considered in this research are: surface roughness, wear resistance, hardness, grain size and self-lubricating level, selection of these properties has been done based on the rigorous literature review [35, 36, 37 77,78,79]. It is worth mentioning that all chosen coatings are having different level of pre-defined five characteristics of material. Further, the coated bearings were installed in customized bearing set up one after another and its vibration signals were captured at the following five different speeds: 300 rpm, 600 rpm, 900 rpm, 1200 rpm and 1500 rpm. Afterwards, statistical analysis of all acquired signals has been carried out by calculating RMS, Skewness, Kurtosis, Variance, Shannon entropy, log energy and Crest factor. These statistical parameters were chosen based on its wide acceptability by many researchers for condition monitoring of bearings [220-238]. After calculating all values, results were presented in tabular form separately according to different values of properties. Like, initially all coatings were arranged in ascending order of its surface roughness value then calculated statistical values were also arranged in table accordingly. Then from table, it was analyzed that which of the statistical parameter values exhibiting same ascending order like surface roughness. In case, any statistical parameter is presenting same trend with the variation in characteristic of material, then it can be said that with the increase in particular property, its effect can be seen in responded statistical parameter. Therefore, it would be possible to detect the variation in property of material by just acquiring its vibration signal and calculating that associated statistical parameter. This is the main objective of this whole research work. Same approach has been carried out for all five properties. Although, it is important to note that, with direct statistical analysis of captured vibration signal, encouraging results were not obtained with variation in any of the five properties. Then, for in depth analysis, all signals were decomposed with

empirical mode decomposition (EMD) but irregular trends were found. Later, wavelet packet transform was applied onto the signals but inconsistency in results continued to exist. Finally, variational mode decomposition technique applied on the signals up to sixth level to generate six amplitude and frequency modulated modes. Then same statistical analysis of all six modes were carried out. This technique was able to find similar patterns (rise or fall) in at least one of the statistical parameters in at least one of the six modes with respect to variation in material properties. However, in case of more than one responded parameter in one or different IMFs at same speed, selection of most sensitive parameter has been carried out based on percentage variation in responded parameter while switching coating. Moreover, average chain index has been calculated also to select the overall most responsive statistical parameter with the change in the specific property of the material. Except hardness, all material properties have responded to following statistical parameters as presented further. However, based on the acquired results, it can be proposed that effect of variation in surface roughness level of the bearing surface can be found in IMF 4 at 900 rpm and in IMF 2 at 1200 and 1500 rpm based on Shannon entropy calculations of the acquired vibration signal. Next, change in grain size found to be linked with variation in variance in IMF 3 at 300 rpm whereas RMS in IMF 2 at 1500 rpm. Moreover, best response towards change in wear resistance was depicted by Shannon entropy in IMF 4 at 300 rpm and in IMF 3 at 600 rpm. However, at 1200 and 1500 rpm, log energy found to be best suited in IMF 4 and IMF 1 respectively in response to change in wear resistance. Lastly, similar results were found in case of self-lubricating level as ascending order of wear resistance values and self- lubricating level found to be same. Hence, degradation in properties of bearing surface can be monitored based on vibration signature analysis without dismantling the bearing.

ACKNOWLEDGEMENT

I would like to express my profound gratitude to Dr. Manpreet Singh, Professor and Head, CAD/CAM & Mechatronics department of Lovely Professional University for his contributions to the completion of my PhD thesis titled “Comparison of different coating properties in bearing by using vibration analysis.” Without his valuable guidance and suggestions, it was not possible to complete this research work.

List of Tables

List of Figures

List of Appendices

List of Symbols

R_a: arithmetical mean roughness

R_y: maximum height

R_z: ten-point mean roughness

S_m: mean spacing of profile irregularities

S: mean spacing of local peaks of the profile

t_p: profile bearing length ratio

HV: Vickers hardness number

$Al_2O_{3:}$ Aluminium Oxide

AISI 52100: Bearing Steel

SiC: Silicon carbide

$MoS_{2:}$ Molybdenum disulfide

σ^2: Variance

$\phi_k(t)$: Mode Phase

$A_k(t)$: Mode amplitude

List of Abbreviations

EMD: empirical mode decomposition

SEM: scanning electron microscope

PTFE: polytetrafluoroethylene

DLC: diamond-like carbon

PVD: Physical Vapor Deposition

CVD: Chemical Vapor Deposition

HVOF: high-velocity oxygen fuel

PECVD: plasma-enhanced chemical vapor deposition

VMD: Variational mode decomposition

IMF: intrinsic mode functions

UCI: Ultrasonic Contact Impedance

STFT: short-time Fourier transform

ROP: ratio of power

PSD: power spectral density

SSA: singular spectrum analysis

FFBP: feedforward back-propagation

DC: direct current

ASTM: American Society for Testing and Materials

ASTM-G99: Standard Test Method for Pin-on-Disk Apparatus

EN31: high carbon alloy steel

RMS: Root mean square

FT: Fourier transform

FFT: Fast Fourier transform

BSE: backscattered electrons

EDS: energy dispersive X-ray spectroscopy

EBSD: diffracted backscattered electrons

LabVIEW: Laboratory Virtual Instrument Engineering Workbench

VIs: virtual instruments

DAQ: data acquisition system

FIR: Finite Impulse Response

IIR: Infinite Impulse Response

SHM: Structural Health Monitoring

WPT: Wavelet Packet Transform

SI: System Identification

DSM: Defect Signal Mode

DSFs: Damage-Sensitive Features

LNMs: linear normal modes

THs: time histories

DWT: Discrete wavelet transforms

WBD: Wavelet packet decomposition

MRA: multiresolution analysis

EMG: electromyograms

MDL: minimum description length

MW: mother wavelet PD: partial discharge

MCCC: maximum cross correlation coefficient

IC: Information extraction

DE: distribution error

FB: foreign body ESER: energy-to-Shannon entropy ratio

MW: Morlet wavelet

db: Daubechies

EM: evaluation metric

EC: evaluation criterion

i.i.d.: identically distributed

ADMM: alternate direction method of multipliers

MCFO: Maximum Center Frequency Observation

CC: Correlation coefficient

PZT: piezoelectric

MEMS: microelectromechanical

SE: Shannon Entropy

LE: Log Energy

CNC: Computer numeric control

ZnP: Zinc Phosphate

SPs: statistical parameters

RPM: Revolutions per minute

Table of Contents

1. Introduction

A bearing is a mechanical element utilized to minimize friction among the moving components of a machine so as to facilitate the attainment of the intended motion. The term "bearing" encompasses the meaning "to support" and "to carry a burden". For instance, a bearing supports the load of a rotating fan and diminishes noise and vibration while constraining movement along a radial axis. The principal bearing functions are: to lessen friction between rotating components, to support rotating machine components and to withstand radial and thrust forces. Typically, bearings come across two types of loads: radial and thrust/axial loads. Radial load refers to the load that acts perpendicular to the longitudinal axis like in case of bicycles, fans, skateboards, food processors, etc. Axial or thrust load is a load that acts in line to the longitudinal axis. Examples include rotating tables, screw jacks, bar stools and fluid control valves. The combined load includes both the axial and radial forces exerted on a structure. For example: railway axles, mining and construction machinery, vehicle engines and gearboxes and agricultural machinery. The application of the bearing will determine whether it is subject to radial or thrust loading, or both. The essential components of bearing are shown in Figure 1.

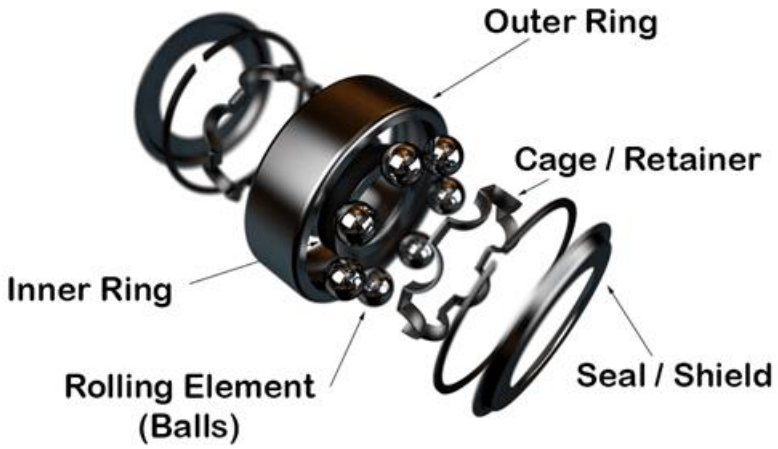

Figure 1: Parts of the ball bearing [1]

a) **Outer ring/race**: The outer ring of the bearing is the larger among two rings. There is a groove on the inner periphery of the ring to allow rotation of the balls in the

passage. The inner grooved surface of the ring is finished to extremely close tolerances and is highly polished. Typically, the outer ring is retained stationary.

b) **Inner ring/race**: The inner ring of the bearing is the smaller among two rings. It has a groove on its outer diameter that functions as a passage for the balls. It is also finished with the same high precision as the outer ring. The rotating element is the inner ring, which is affixed on the shaft.

c) **Rolling elements**: The rolling elements separate the inner and outer rings of a bearing and allow it to rotate with minimal friction. Rolling elements have a significantly smaller diameter than the inner and outer tracks. The dimensions of rolling element dimensions have to be meticulously controlled. Surface texture and dimension variations are essential characteristics. These characteristics are governed to the micro inch level. The bearings can be classified based on type of rolling element used in between the races like: balls, cylindrical rollers, spherical rollers, tapered rollers, needle rollers, etc.

d) **Cage/Retainer**: The role of the cage in bearings is to maintain a constant distance between the inner and outer rings and to separate the rotating elements, to precisely direct the rolling elements along the path during rotation and to prevent these elements from tumbling out.

e) **Shield**: The shield, a profiled sheet metal disc, is stamped and pressed into a narrow crevice on the inner edge of the outer ring's inner diameter. A deliberate space is maintained between the outer diameter of the inner ring and the shield. This intentional gap ensures that the shield doesn't come into contact with the bearing's inner ring, thereby avoiding any additional friction. Shields are specifically engineered to bar larger contaminants from infiltrating the bearing.

f) **Seal**: The seal is likewise fitted into a narrow groove located on the inner, thinner rim of the outer ring. Its inner edge features a lip structure meticulously crafted for effective sealing.

1.2 Failures modes of bearing [2]

Precision ball bearings are made to last a long time and be effective. Providing the application is initially correct, bearings need to be correctly placed, greased, and maintained in order to maximize longevity. Poor conditions for operation particularly damp or impure regions, incorrect handling techniques encourages early bearing failure.

It is crucial to pinpoint the exact cause of a bearing failure so that the proper adjustments can be made. Investigation of the failure mode can describe the reason behind the failure. Since one failure scenario could lead to another, this technique is complicated. For instance, corrosion in a ball race can produce rust, an abrasive that can wear down materials and cause a loss of preload or an increase in radial clearance. In a grease-lubricated bearing, worn debris can obstruct lubrication, leading to lubrication failure and consequent overheating. The different types of bearing failure are:

A) **Excessive load:** Premature failure is typically caused by excessive loads. Early fatigue failure can also be caused by inadequate preloading, brinelling, and tight fittings. Failure of this kind typically resembles normal fatigue. Even though extensive ball wear routes are present, excessive heat up and a fatigue region are typically seen with decreased life. To resolve this issue, decrease in load or remodeling with more potential are the two possible alternatives.

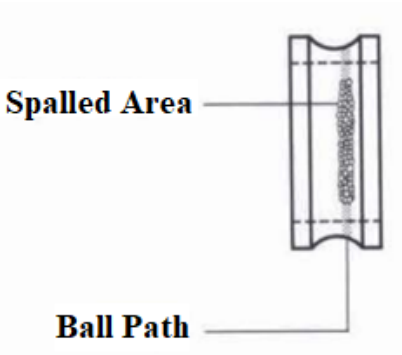

Figure 2: Failure due to excessive load

B) **Overheating:** In case of overheating, the rings, balls, and cages turn from golden to bluish as a symptom. The materials for the ring and ball gets annealed at

temperatures higher than 400°F. As a result, the hardness decreases, lowering the bearing capacity and hastening failure. In severe circumstances, rings and balls may distort. As the temperature rises, properties of lubricant also get effected hence leads to overheat. Heavy electrical heat burdens and inadequate heat paths are typical culprits along with inadequate cooling or lubrication under excessive loads and velocities. To overcome this issue, heat or excessive loading controls, proper thermal paths, and additional ventilation proves to be an effective solution.

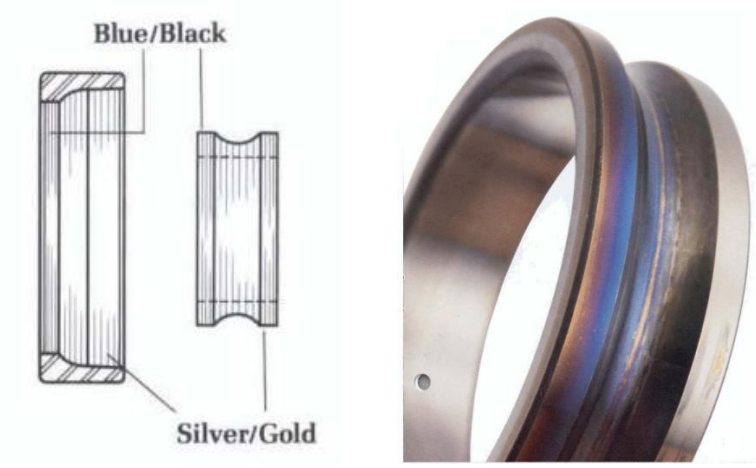

Figure 3: Discoloration of bearing elements

C) False Brinelling: Excessive external vibration indicates false brinelling, which appears as ellipsoidal signs of wear along the axis at ball location, with a brilliant finish and strong borderline, and usually encircled with a brown debris ring. When a non-rotating ball bearing is subjected to external vibration, the balls move relatively with respect to the raceway. When the bearing is not rotating, an oil film that prevents raceway erosion cannot be formed. The oxidation of wear detritus accelerates the wear process. It can be corrected by isolating bearing from external vibration or with the usage of anti-wear elements like greases or molybdenum disulfide.

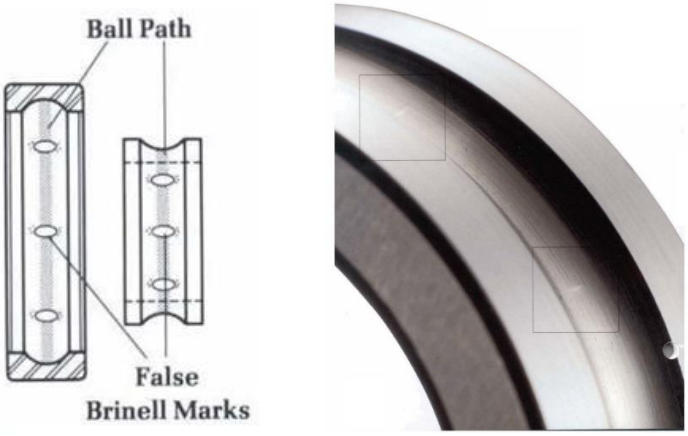

Figure 4: False Brinelling marks on bearing element

D) True Brinelling: Brinelling appears when load surpasses the elasticity of ring content. Indentations called Brinell marks can be seen in ball passages of a bearing, and it increases the intensity of vibration in the bearing. Extreme Brinell marks might lead to fatigue failure beforehand. Brinelling can also be caused by any static overflow or severe impact. For instance, a bearing can be installed onto a shaft by exerting force to the outer ring with a hammer. Dropping or damaging assembled equipment is another common cause of bearing damage. While press-fitting a bearing onto a shaft, it is advisable that only the ring that is being press-fitted should be pushed with a significant amount of force; the outer ring should not be pushed at all.

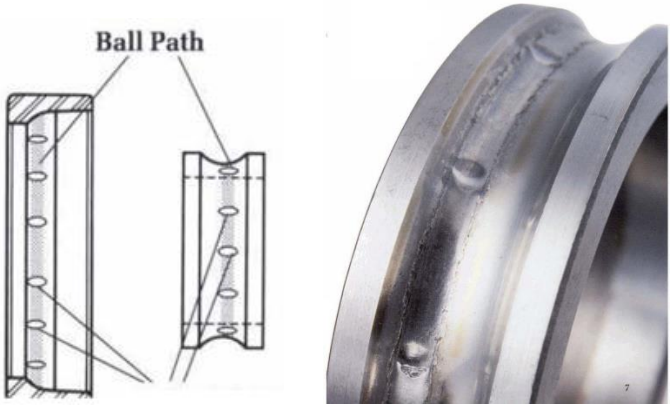

Figure 5: Ball spaced Brinell marks

E) Normal Fatigue Failure: Fatigue failure, also known as spalling, is the fracture and subsequent elimination of small, discrete particles of material from the running surfaces. The interior ring, the outer ring, and the balls are prone to spalling. This form of failure is gradual and will escalate with ongoing operation once initiated. It is consistently accompanied by a discernible rise in vibration, signaling an abnormality. The remedy involves either replacing the bearing or reconsidering the design to integrate a bearing with an extended calculated fatigue life.

Figure 6: Spalled area on bearing inner race

F) Contamination: Contamination stands out as a primary contributor to bearing failure. Because of contamination, pitting usually occurs in balls and its running passages, causing excessive vibration and wear**.** Examples of contaminants are floating dirt, grime and any coarse-grained particles that enters inside the bearing. Principal origins include soiled instruments, infected job environments, soiled hands, and external particles in lubricants or cleaning solutions. The cleanliness of shop floors, machines, jigs and fixtures, and accessories aids in the prevention of contamination losses. It is advisable to carry out grinding jobs isolated from assembly line, and store bearings in their original packaging until installation. Seals that are severely damaged or inoperable cannot protect bearings from contamination.

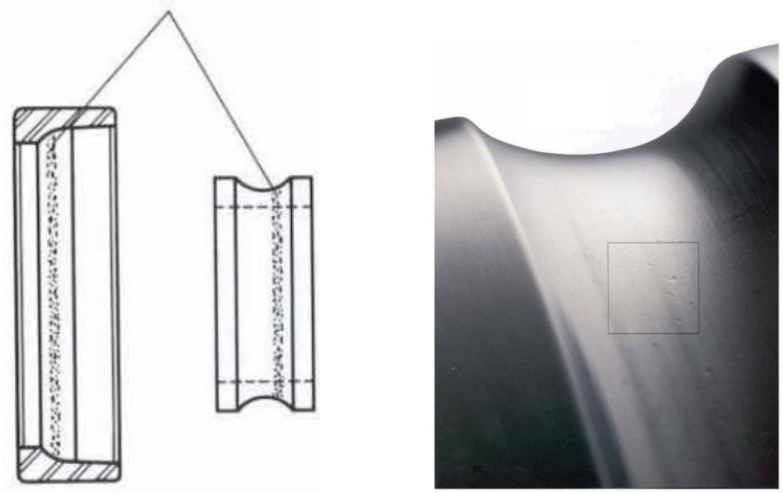

Figure 7: Bearing contamination failures

G) Lubricant Failure: Ball traces and balls that are discolored (blue/brown) are indicative of lubricant failure. The excessive wear of the balls, ring, and cages will lead to overheating and calamitous failure. To function properly, ball bearings require a constant coating of lubricant to be present between the balls, rings, cage and races. Typically, failures arise due to either constrained lubricant flow or elevated temperatures that lead to degradation in the properties of lubricant. Any measures opted to rectify inappropriate fittings, with better regulation of preloading conditions and ensuring proper cooling of shafts and casings can effectively lower bearing temperatures. and lengthen life cycle of the lubricant.

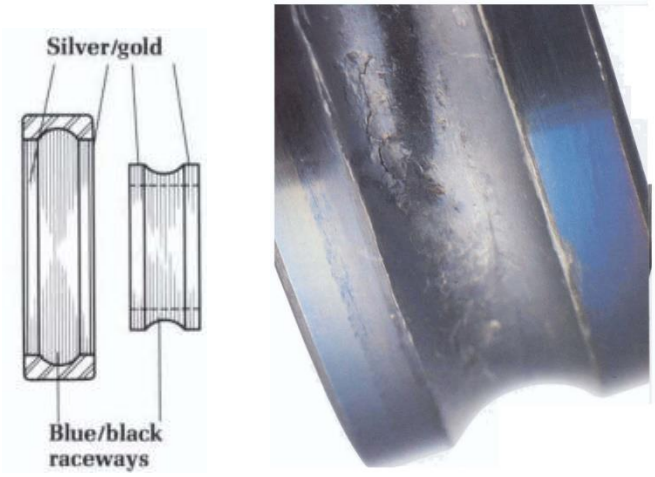

Figure 8: Excessive wear and overheating due to lubricant failure

H) Corrosion: Reddish-brown spots on the balls, raceways, cages, or bands of ball bearings indicate corrosion. This condition occurs when bearings are working in corrosive fluids or an atmosphere. Typically, rise in vibration is followed by increased wear, resulting in an increase in radial clearance or loss of preload. In extreme conditions, corrosion can cause fatigue failures to occur sooner. Use integrally sealed bearings whenever possible, and correct by rerouting corrosive fluids away from bearing zones. If the environment is unusually hostile, external seals should be considered in addition to integral seals. Utilizing stainless steel bearings is also advantageous.

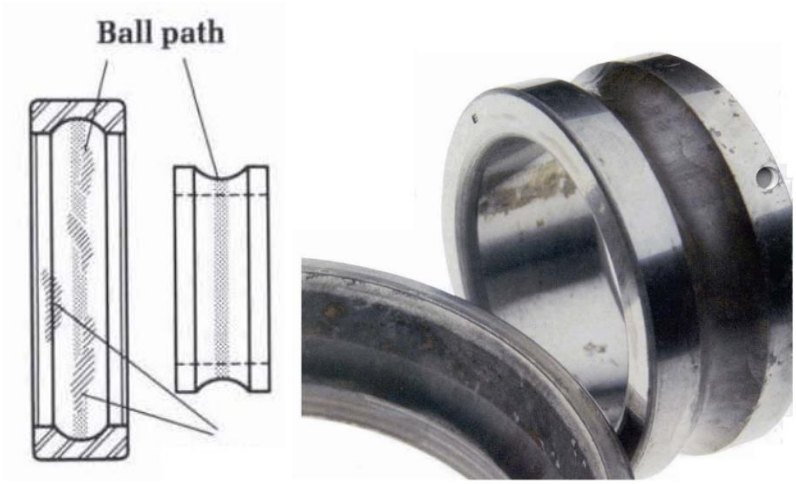

Figure 9: Corrosion attack on the metal due to hostile fluids or atmosphere

I) Misalignment: A ball wear pattern that deviates from parallelism with the raceway edges can serve as an indicator of misalignment on the non-rotating ring's raceway. An abnormal temperature rise in the bearing can be anticipated with significant wear in the cage ball-pockets if misalignment is greater than 0.001 in./in. Bends, burrs or impurities on shaft or casing shoulders, out-of-square shaft threads Concerning shaft seats and locking nuts, the most prevalent causes of misalignment are faces that are not perpendicular to the thread axis. The permissible misalignment varies widely between applications, for instance decreasing with speed. Corrective measures are using single point-turned or ground threads exclusively on non-hardened shafts, and employing ground threads solely on hardened shafts, as well

as utilizing precision grade locknuts, and inspecting shafts and housings for any deviation in the alignment of shoulders and bearing seats.

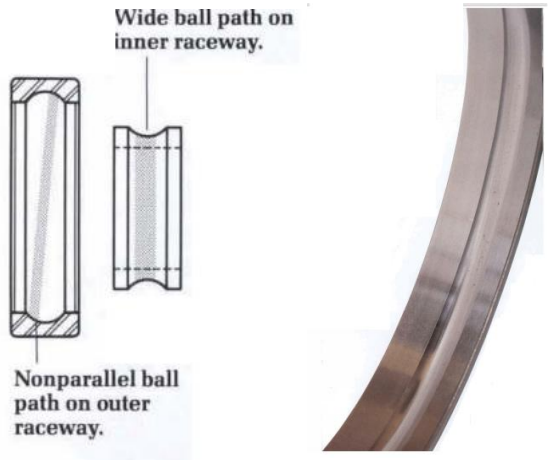

Figure 10: Misalignment causes abnormal temperature rise and premature wear

J) Loose fits: Loose fittings can result in relative movement between mating components. Fretting occurs when the relative motion between mating elements is slight but continuous. The process of fretting generates thin metallic layers that oxidizes, which results in a brown hue afterwards. This abrasive material will exacerbate the slackness. If the slackness is sufficient to accommodate significant inner or outer ring movement, the mounting surfaces will wear and heat up, leads to noise and runout issues.

Figure 11: Discoloration and scoring due to outer ring slippage in the housing

K) Tight Fits: Excessive ball worn out in the raceway base along the whole inner and outer ring circumferences is indicative of tight fit. When interference fits surpass the radial clearance at operating temperature, it results in overloading of the balls, which leads to sudden increase in temperature and a high torque. Rapid degradation and fatigue may result from continuous operation. Remedial measures include a reduction in overlapping: a improved match between bearings, shafts, and casings, considering material and operating temperature differences. Under the aforementioned conditions, a greater radial clearance will also extend bearing life.

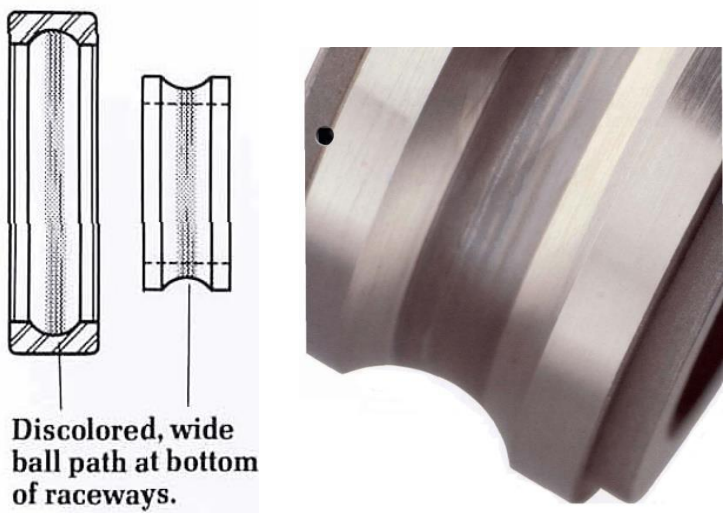

Figure 12: Discolored wide ball path at bottom of raceways

1.3 Bearing Life

Bearing life is the period during which it can be anticipated that the bearing will fulfill its intended function adequately under predefined operating conditions. Moreover, it is considered as the anticipated number of rotations a bearing can endure before displaying fatigue symptoms such as spalling or stress-related cracks.

1.3.1 Factors determining the service life of a bearing

In addition to normal wear and tear, failure in bearing can occur due to extreme temperatures, fractures, lack of lubrication, or seal or cage damage. This type of bearing

damage is frequently the result of improper bearing selection, discrepancies in the design of the adjacent parts, improper installation, or inadequate maintenance.

Figure 13: Typical symptoms of fatigue include the detachment of small, flat flakes of bearing material (flaking/spalling) [3]

1.3.2 Basic fatigue life rating L10

The fatigue life rating of a bearing is established based on the number of rotations where 90% of all bearings within a specific group achieve or surpass the calculated duration without failure. This is typically determined using a standardized formula, often referred to as the catalogue method (ISO 281), which takes into account parameters such as bearing load, rotational speed, dynamic load rating, and bearing type. As a result, the bearing's fatigue life, denoted as L_{10} or L_{10h}, is calculated as shown in equation *(3)*.

The dynamic load rating, also referred to as the basic load rating, denotes the constant load that bearings with stationary outer rings can endure for a rating life of one million revolutions (10^6 rev). A constant radial load applied to the bearing's center is considered its basic load rating, whereas a constant axial load applied in the bearing's axis of rotation is considered its basic load rating for thrust bearings. In the dimension tables, the load ratings are listed under C_r for radial bearings and C_a for thrust bearings.

The dynamic equivalent load P is defined as a constant magnitude and direction radial and axial load for radial and axial bearings respectively that exhibits mirror impact on the lifespan of the bearing according to actual forces exerted on the component. For constant or combined loads, P is determined with the help of subsequent formula [3] as shown in equation *(1)* and *(2)*

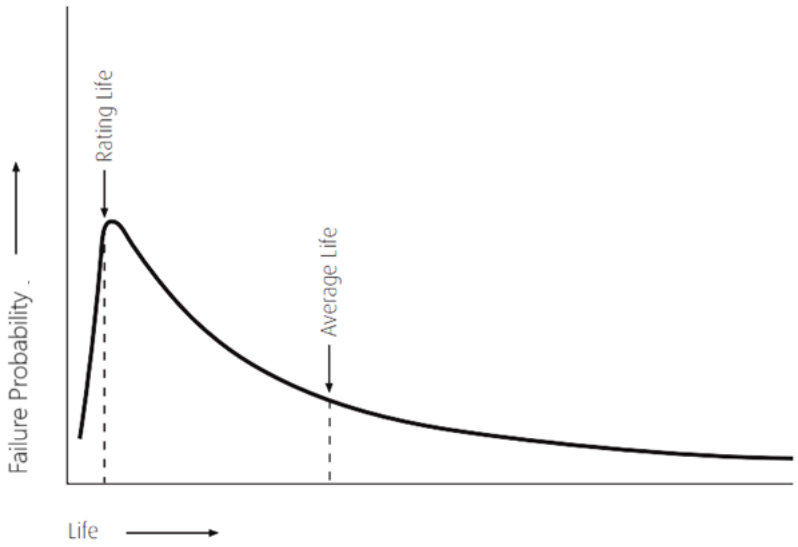

Figure 14: Failure Probability and Bearing Life [3]

$$P = X \bullet F_r + Y \bullet F_a \quad (1)$$

Other than Thrust Spherical Roller Bearing:

$$P = F_a + 1.2 \bullet F_r \quad (2)$$

L_{10}/L_{10h}: basic life rating [10^6 rotations/h]

$$L_{10} = \left(\frac{C}{P}\right)^p \text{ or } L_{10h} = \frac{10^6}{60n}\left(\frac{C}{P}\right)^p \quad (3)$$

C: Dynamic load rating [N]

P: Dynamic equivalent bearing load [N]

p: Exponent (3 for ball bearings, 10/3 for roller bearings)

n: Rotational speed [rpm]

After studying failure modes of the bearing and bearing life calculations, it is advent that each failure leads to degradation in the properties of bearing material which is affecting bearing life. For example, failure due to excessive load, normal fatigue failure,

true brinelling and contamination leads to surface irregularities and hence variation in surface roughness. Likewise, overheating, misalignment and tight fits are responsible for rise in temperature which results in reduction of hardness of the bearing element. Moreover, failures like false brinelling, corrosion and loose fits acts as catalyst to wear process hence impacting wear resistant property of bearing element. Additionally, grain size also strongly influences several mechanical properties of material like hardness, wear resistance, ductility and strength also as per Hall-Petch relationship [5]. Therefore, it can be concluded that surface roughness, hardness, wear resistance and self-lubricating level are significant properties of bearing element as most of the failures are associated with degradation in following properties of the material along with grain size variation.

Therefore, to improve the life of bearing by enhancing desirable properties of bearing elements, manufacturers have adopted different methods like heat treatment or coating of bearing elements. From the discussion on failure modes of bearing, it is clear that the properties of the material start degrading at micro level which ultimately leads to failure without getting notice until failure occurs. Therefore, it is very important to keep a check on deterioration in important properties of material like Surface roughness, Hardness and Wear resistance during its life cycle so as to predict remaining useful life of the machine element accurately. Along with these properties, one more factor must be included due to introduction of coating on bearing element, i.e., grain size. Grain size plays an important role in behavior of the material. Grain size is the dimension of the crystallites or elements that make up a solid metal. Grain size and grain boundaries are significant factors in determining the physical properties of the entire metal. In thin film deposition, the grain size will be smaller if the particles are deposited with a high quantity of energy and they exhibit a high level of migration. If migration is reduced when particulates condense on a substrate, the grain size will be greater. Density of a coating is significantly influenced by the energy and particulate size of thin film particles. Grain or particle refinement can be utilized to alter the grain boundary density. Consequently, the coating's wear resistance and resilience are enhanced. The optimal grain size for thin film coatings depends on the desired result and physical properties, particularly the intended density. Coating density typically decreases with increasing

particle size in a thin film. Therefore, for applications requiring a greater density, a film with a smaller grain size and greater migration is optimal. If less density is desired, a film with a larger particle size and lower migration would be optimal [4]. Finally, along with grain size, the significant material properties considered in this research work are surface roughness, hardness, wear resistance and self-lubricating level.

Conventionally, there are numerous techniques available to measure the above-mentioned properties of coated elements like Profilometer for surface roughness, Vickers hardness tester for coated surface hardness, pin-on-disc test for wear resistance and scanning electron microscope (SEM) analysis for grain size. However, in all these methods, machine element must be dismantled for the purpose of analysis which leads to idle time and it is impractical to measure properties of material using conventional methods at different life stages by dismantling the machine component. Therefore, researchers have developed several on-board techniques like acoustic signal analysis, thermography, motor current signature analysis, radiography, oil analysis, ultrasonic monitoring, laser interferometry and vibration analysis to monitor the status of the machinery. However, vibration signature analysis considered to be most sensitive in detecting the micro level variation in the material of machine element as it is also widely used by many researchers in detecting faults at incipient stage [6,7].

In this research work, five different coatings with different level of material properties have been selected for the bearing elements as per the industrial standards. The outer and inner race of bearing were electroplated with the following five different coatings: Nickel, Copper, Silver, Zinc phosphate and black oxide. All coatings are having unique level of surface roughness, hardness, wear resistance, grain size, and self-lubricating level. Two sets of coated bearing have been prepared, one is used for experimentation and second is utilized for the sake of characterization of already specified material properties. After measuring the level of considered properties for all bearing coatings, coated bearing has been installed in the bearing casing for the experimentation to capture its vibration signal in running condition. Then, effect of degradation in surface properties is monitored by analyzing variations in vibration signal.

2. Literature Review

The study of the literature has been divided into two parts. Firstly, significance of coatings has been discussed followed by discussion on various methods of coatings. Further, review on analysis of different coating properties has been carried out.

2.1 Coatings on bearing

Surface technology is among the most vital technologies in industry. By utilizing appropriate coating systems, it is possible to meet higher requirements for corrosion or wear protection as well as friction reduction. Consequently, coating systems contribute to the conservation of resources by extending the service life of components and reducing energy losses due to friction. This technology will grow in significance in the future, not only for extant products but also especially for new product types. Energy systems and wind energy are examples that can be used to illustrate this point. Moreover, a future contribution to the digitalized networking of the components and systems will be made possible by the multifunctional properties of components' surfaces. Energy systems and wind energy are examples that can be used to illustrate this point. Further, a future contribution to the digitalized networking of components and systems will be made possible by the multifunctional properties of component surfaces [10,11].

2.1.1 Coating systems with its applications

Coating is a tried-and-true method for enhancing the performance capability of the base material through functional expansion, thereby providing components with additional properties for specific applications. Coated rolling bearings enhance corrosion resistance in addition to tribological and electrical insulation properties. Corroded bearing components can cause functional issues, decreased efficiency, and premature bearing failure. Appropriate coatings may serve as a substitute for costly, corrosion-resistant bearing steels. The quality of a rolling bearing is largely determined by its smooth operation and resistance to attrition. These variables affect not only the

fundamental operation but also the energy and material requirements. A low friction coefficient decreases both energy consumption and lubricant requirements. This is related to reduced mechanical fatigue. In turn, this ensures the bearing's continued functionality and extends its service life. Coating systems are appropriate for the enhancement of tribological behavior. In these instances, the performance under poor lubrication conditions (lubricant starvation) can also be substantially enhanced by selecting the appropriate coating. To prevent rolling bearing failures caused by current flow, ceramic insulating coatings can be applied to the cylindrical surfaces and end faces of the bearing rings [11].

Depending on the specific application and requirements, a bearing's coating can provide various advantages. Here are some commonly utilized bearing coatings:

- Anti corrosion coating: In corrosive environments, bearings may require a protective coating against rust and other forms of corrosion. Zinc, nickel, chrome, and various forms of polymer coatings are common anti-corrosion coatings.
- Lubrication enhancers: Coatings can enhance bearings' lubrication properties, thereby minimizing friction and wear. For instance, certain solid lubricant coatings such as molybdenum disulfide (MoS_2) or polytetrafluoroethylene (PTFE) can be applied to improve the self-lubricating properties of the bearing.
- Thermal Barrier Coatings: Thermal barrier coatings can be beneficial for bearings exposed to elevated temperatures. These coatings provide insulation, which reduces heat transfer to the bearing and enhances its performance and durability.
- Wear resistant coating: When bearings are exposed to high loads or abrasive environments, wear-resistant coatings may be required. These coatings can be applied to the bearing surfaces in order to increase their hardness, resistance to attrition, and longevity.
- Low friction coatings: Coatings such as diamond-like carbon (DLC) and other nanocomposite coatings can reduce friction between bearing surfaces, resulting in increased efficiency, decreased energy consumption, and decreased heat production.

Notably, the choice of coating is dependent on bearing type, operating conditions, desired performance enhancements, and cost considerations. The utilization of specific coating will vary based on the requirements of the application.

2.1.2 Various methods of coating bearing elements

Several methods are used for coating of the bearings, each is having its own advantages and disadvantages. Commonly used methods for coating bearings are:

- Electroplating and Electroless Plating: Electroplating is the electrolytic deposition of a metal coating on a bearing surface. It provides exceptional adhesion and coating thickness control. Electroless plating is a chemical procedure that deposits a metal coating on a bearing surface without using an electrical current. It provides homogeneous and regulated coatings, even on intricate geometries.
- Physical Vapor Deposition (PVD): PVD techniques, including sputtering and evaporation, involve the vaporization of a solid metal or alloy, which is then deposited on the bearing surface. This method produces thin, adherent coatings with superior hardness, wear resistance, and friction.
- Chemical Vapor Deposition (CVD): CVD is a process that involves introducing a reactive gas to the bearing surface, which then reacts to form a solid coating. It permits precise control over coating composition and thickness and can produce dense, conformal coatings with high thermal stability.
- Thermal Spray Coating: Thermal spray techniques involve heating and propelling coating material particles onto a bearing surface. This technique incorporates plasma spraying, flame spraying, and high-velocity oxygen fuel (HVOF) spraying. Thermal spray coatings offer superior abrasion resistance, corrosion protection, and the ability to deposit different materials (metals, ceramics, polymers).
- Sol-Gel Coating: Sol-gel is a wet chemical process that entails the formation of a thin film on a bearing surface from a sol (a stable colloidal suspension). The sol-gel coating provides enhanced adhesion, lubrication, and corrosion resistance after drying and curing.
- Polymer-based Coatings: Bearings are coated with polymer-based coatings, including solid film lubricants, to reduce friction, wear, and noise. These coatings

frequently contain lubricating additives such as PTFE (polytetrafluoroethylene) or MoS_2 (molybdenum disulfide).

- Diamond-Like Carbon (DLC) Coating: DLC coatings are a form of diamond-like amorphous carbon coating. They possess extraordinary hardness, low friction, high wear resistance, and chemical inertness. DLC coatings can be applied using PVD or plasma-enhanced chemical vapor deposition (PECVD) techniques.
- Hybrid Coatings: Hybrid coatings combine diverse materials or processes to attain properties. Combining a tough ceramic layer with a lubricious polymer layer, for instance, can provide wear resistance and minimal friction.

It is essential to note that the selection of a coating method is contingent on a number of variables, including the desired properties, application requirements, budget, and production scale. Each method has its own advantages, limitations, and considerations, and the selection should be based on the bearing application's specific requirements. Some common methods that are used by bearing industries are anodizing, galvanizing and electroplating [12]. Anodizing is a procedure that triggers the generation of a protective oxide layer on a metal's surface. The resultant oxide layer develops at an accelerated rate and tends to be thicker compared to its natural formation [13]. Galvanizing is the procedure of immersing a metal (typically iron or steel) in a bath of molten zinc. When the coated metal is removed, it reacts with oxygen and carbon dioxide in the environment to form a protective layer of zinc carbonate [0]. Electroplating, also known as electro-deposition, is the application of a fine layer of one metal onto the surface of another. During electroplating, both metals are immersed in an electrolytic solution. The cathode is the coating metal, while the anode is the metal to be coated. A current is transmitted through the electrolytic cell, resulting in the flow of metal ions from the cathode to the anode and the formation of the coating [15].

There are a variety of materials that can be used to surface bearings, depending on the desirable property to be enhanced. The most widely used bearing coatings in the industry are Nickel, Copper, Zinc phosphate, Silver, and Black oxide [11]. The nickel coating has been used to improve corrosion resistance, adhesive resistance, and abrasive wear which make it a potential choice in engineering applications [20]. It has been observed that along with enhancing corrosion resistance, nickel electroplating also

improves the conductance and resistance to oxidation in transparent conductor also [21]. Moreover, nickel plating was also used on parts made by laser additive process to improve friction and wear behaviour. An important point to be noted that electroplating with nickel is a commercially significant surface treatment procedure that annually consumes approximately 100,000 tons of nickel across the globe [22]. As far as copper coating is concerned, due to its high conductivity and corrosion resistance that copper coatings confer on engineered assemblies, the use of copper coatings on steel mechanisms is abundantly viable. Copper electroplating on bearing steel AISI 52100 exhibited excellent results under sliding load. Moreover, it coating resulted in lower friction coefficient and wear loss from the surface of substrate, hence better surface properties [23]. Commonly, copper coating is preferred for enhanced tribological properties and increased electrical conductivity and is widely used on large bearing cages and cages for aerospace applications [24]. Further, in case of zinc phosphate coating, it has been observed that it has excellent friction reduction and wear protection properties and is utilized in numerous industries, including the wire drawing industry, the automobile industry, and various appliance and electronics industries. [16]. Phosphate coating is one of the most popular pre-treatments for steel due to its affordability, speed of application, abrasion resistance, and lubricating properties [17]. Moreover, zinc increases the hardness of the surface without affecting their corrosion resistance negatively when tested on mild steel substrate and verified using Vickers micro hardness tester [25, 26]. To improve the sustainability of bearing at high temperatures, silver coating has been used and depicted outstanding tribological characteristics at elevated temperatures. With the silver coating on bearing surfaces having antifriction performance, the magnitudes of friction force and coefficient could potentially be reduced. Crystallinity, microhardness, residual strain, and grain size are all enhanced on bearings when heated to high temperatures. Tribo-chemical reactions increase the surface's uniformity, making it more resistant to plastic deformations and so extending the bearing's useful life [28]. Surfaces benefit from increased wear resistance and antifriction due to the combined effects of Ag element, which is a hard lubricant with excellent lubricating behavior, and texturing [29-33]. Additionally, it has been found that to provide exceptional electrical conductivity for high-speed bearing, silver coating proves to be an effective solution [19]. Electroplating with silver has

existed for centuries. It has been utilized since the beginning of coinage and metal working. In modern times, silver was initially accumulated as a status symbol and, more significantly, for industrial use. Moreover, silver coating is used in numerous types of medical devices, including surgical instruments, implants, and MRI machines, incorporate metal coatings and finishes to provide or enhance various advantageous properties. Depositing a fine metal layer to the exterior of a medical device, such as through the plating process, can enhance electrical conductivity, reflectivity, and resistance to pathogens, among other benefits [20]. Along with medical, silver plating has been widely used in other areas like aerospace, defense, microelectronics, jewelry, and automotive industries [34]. Therefore, it can be said that the benefits of using silver coating are enhancement of tribological properties, increased emergency running performance under low-lubricant situations, better heat removal from a working space, to make substrate sustainable to extreme velocities and speeds and higher electrical conductivity [17]. Lastly, the significance of black oxide coatings in the field of bearing cannot be skipped. As utilization of black oxide coatings in bearing applications is prevalent throughout the industry [35]. In comparison to non-coated bearing steels, a black oxide layer has several advantages: It has better running-in behavior, higher corrosion resistance, lower hydrogen permeability, more micro pitting protection, and better smearing/scuffing resistance than conventional lubricants [36-41]. Black oxidation helps in reducing the prematurely risks of failure in wind gearbox bearings and wind turbine drivetrains due to cracks, spalls, or erratic white etching cracks (WECs). WEC describes how a microsection of polished and etched steel looks after its microstructure has been modified. Several bearings in a wind gearbox, including the planet bearings, intermediate shaft bearings, and high-speed shaft bearings, are prone to failure [42]. There are several mechanisms that, according to ongoing research and literature, can help lower the chance of WEC failures, including reduction in abrasive and corrosive wear [43], bearing steel with less hydrogen diffusing into it [44], protection from corrosion [45] and stabilization of track surface microstructure [71]. Therefore, Black oxidation serves as a protective measure for bearing components against the aforementioned failure mechanisms. Moreover, black oxide's porous microstructure helps boost the coating layer's affinity for lubricant or preservatives, which in turn makes the coating more water- and corrosion-resistant [42]. Black

oxidized bearings have been put through a bearing life test under extreme mixed lubrication circumstances. In terms of running-in and low kappa lubrication circumstances, the advantageous impact of black oxidized bearings over their non-coated counterparts has been proved [77].

From literature, it is obvious that different bearing manufacturer are coating the bearing elements with aim of enhancing the surface properties of bearing elements. Along with grain size, the important coating properties of the bearing elements considered in this work are: Surface roughness, Hardness, Wear resistance and Self-lubricating level. Next, the literature about evaluation of these coating properties is presented one after another.

2.2 Review on analysis of coating properties

Starting with surface roughness, E.García et al. had applied singular spectrum analysis (SSA) for the examination of surface roughness in CNC turning operation using vibration signal. SSA was used to decompose the signal into multiple sets of principal components. The results indicate that a single spectrum analysis of vibration signal processing distinguished the optimal frequency range for surface roughness prediction. [46]. Same author applied wavelet packet transform to predict the surface roughness using biorthogonal 4.4 wavelet. The best association between the vibration signal and the surface roughness was discovered at the third level of decomposition. The considerable packets were obtained in the medium to high frequency DDA (6250-9375 Hz) and high frequency ADA (9375-12500Hz) ranges [47]. Generally, conventional decomposition technique decomposes the signal without considering its nature but on the basis of highest frequency present in the signal. Sometimes, these frequency bands are very wide and contains insignificant information of the signal along with significant information. Due to this insignificant information present in the signal, it becomes difficult to study characteristics which are having lower energy contents. In the cases where required characteristics are having low energy levels, Variational mode decomposition (VMD) is proposed. The main advantage of VMD is that it is non-recursive in nature and generates frequency band across the significant frequencies

present in the signal [49]. These frequency bands are called intrinsic mode functions (IMF) with having specific sparsity characteristics while reproducing the signal. In this method, principal modes (IMF) of the signal are extracted while updating center frequencies for each mode during shifting operation [50,51]. VMD was successfully used to detect bearing fault by differentiating the transient impulses of complex vibration signals using IMF evaluation index [48]. Due to VMD's capacity to highlight non-stationary signal characteristics, significant results were obtained while analyzing seismic data with low frequency and high amplitude [52]. Moreover, VMD exhibits excellent execution in decomposition and feature extraction to diagnose rotor-stator faults by detecting multiple signal characteristics induced by rubbing in gas turbine blade [120]. In addition, VMD has also been used to enhance the precision of diagnosis by extracting weak characteristics of the signal corresponding to bearing's fault [53,54].

In case of hardness testing, commonly used methods are: Rockwell, Brinell, Vickers and Knoop testing. In all these methods, the resistance to penetration i.e., depth of indentation is going to be the measuring principle. However, among these four, Vickers method is preferred for measuring hardness of thin surfaces like coatings [55-58]. On the other hand, Ultrasonic Contact Impedance (UCI) Hardness Testing and Electromagnetic Induction Hardness Testing are considered to be non-destructive hardness measurement methods. Hardness is measured, without damaging the sample, by ultrasonic contact impedance (UCI) testing, which is commonly used on metals and alloys. Under compression, an indenter's depth of penetration is proportional to the load applied, hence UCI testing is based on the relationship between material hardness and elastic modulus. UCI testing employs a small Vickers indenter with a diamond-tipped point. Typically, the diamond tip has a pyramidal shape with a very small angle at the apex. The indenter is placed against the surface of the material, and a controlled force is applied. A transducer for ultrasonic waves is affixed to the indenter. Through the indenter, a high-frequency vibration is transmitted into the material. Measuring the resulting contact impedance, which is the resistance to the flow of ultrasonic vibrations. There is a relationship between material hardness and contact impedance. The contact impedance is higher and the indentation is shallower with harder materials, while the opposite is true with softer materials. The UCI hardness value is derived from the

calibration-established relationship between contact impedance and hardness [59-61]. Another nondestructive method of measuring hardness, Electromagnetic Induction Hardness Testing is useful in evaluating case depth of hardened material. This method is especially useful for determining the hardness of heat-treated components, such as carburized or induction-hardened parts. It is based on the principle that a material's hardness influences its electrical conductivity and magnetic permeability. The technique makes use of the correlation between a material's hardness and its electrical conductivity and magnetic permeability. An electromagnetic field is produced when an alternating current with a high frequency is created in a coil. The measurement instrument consists of a probe or coil placed on the surface of the material. The electromagnetic field's alternating nature is produced by the coil. Eddy currents are created in the material due to the alternating electromagnetic field. The hardness and case depth of the material affect the behavior of these eddy currents, including their penetration depth and phase shift. The amplitude, phase, and impedance of the eddy current are all measured by the equipment. The material's hardness or case depth is connected to these shifts. Accurate results are impossible without calibration. The output of the instrument is then correlated with the hardness of a collection of reference samples with established values. Based on the relationship determined during calibration, the device returns a hardness value. Some tools may also be able to produce a graphical representation of depth-dependent hardness changes [62-66]. Thomazella et al. developed a novel vibration signal processing method for chatter identification in tangential surface grinding of AISI 1045 steel using the short-time Fourier transform (STFT) and the ratio of power (ROP) statistical tool. In addition, the Vickers hardness, irregularity, and metallography of the surfaces of the ground workpieces were evaluated. The vibration signals underwent digital processing utilizing a technique grounded in the Short-Time Fourier Transform (STFT) and ratio of power (ROP) to deduce the properties of the babble. The findings indicate that this approach can be utilized for characterizing the spectral bands linked with chatter over a duration [67].

Further, in case of wear evaluation, a systematic approach for monitoring diamond tool degradation based on vibration measurements was developed. The monitoring system used the correlation coefficient with a perfect trend function to choose the

characteristics that consistently demonstrated tool wear. The monitoring system can rapidly extract and select features, allowing the manufacturer to implement an online monitoring system. This system will allow the manufacturer to optimize the utilization of diamond tools, resulting in substantial cost savings [63]. In turning operation, the relationship between tool wear and features of vibration signal has been developed. It was observed that frequency-based features associated well with the tool wear. The characteristics revealed a strong correlation between the measured wear values and particular resonant peak frequencies [68]. In another study of twist drill wear detection, vibration signal processing techniques proves to be more reliable and efficient when training a supervised neural network to identify and categorize the drill wear. Discrete harmonic wavelet transforms, Burg power spectral density (PSD), and four statistical metrics in the time domain were used to examine the data gathered from extensive experimentation. The findings demonstrate that once the neural network was appropriately instructed, it became an effective and trustworthy instrument for addressing classification and pattern recognition tasks, such as those encountered in this drilling job examination. The findings clearly signify that vibration signals have enormous potential for monitoring tool condition and diagnosing manufacturing processes [69]. Along with this, a reliable tool wear monitoring system was proposed based on vibration signal analysis. The singular spectrum analysis (SSA) and cluster analysis are used to analyze the constitution of the tool vibration signals, which forms the basis of the proposed tool condition monitoring system. SSA is a cutting-edge non-parametric time series analysis method that breaks down the recorded vibrations of a tool into a series of time points that can be analyzed together. To assess the tool flank wear, a feedforward back-propagation (FFBP) neural network is trained using a clustered SSA decomposition, which yields numerous distinct components in the frequency domain [70]. Another wear identification technique was proposed based on vibration signal for gears using an indicator of vibration cyclo-stationarity. In particular, the relationship between tribological features of the two wear phenomena and gear mesh-modulated second-order cyclo-stationary properties of the vibration signal is studied, taking into account the fundamental physics of gear meshing and the distinctive surface characteristics caused by fatigue pitting and abrasive wear. Gear mesh-cyclic components are analyzed for their carrier frequencies (spectral content) in order to

differentiate between the two wear phenomena. Using vibration data from two tests—one lubricated and influenced by fatigue pitting, and one dry and influenced by abrasive wear—the efficiency of the suggested approaches in wear mechanism recognition and deterioration trail is proven. With this advancement, fatigue pitting and abrasive wear can be detected and monitored using vibration-based approaches [76].

For grain size evaluation also, vibration signature has been used in estimating the sediment flux and grain size in river bed based on the amplitude of main mode of vibration. Sediment flux in rivers can be estimated indirectly by measuring the vibrations caused by sediments being moved on the riverbed. Metal plates installed on the riverbed are a commonly used technique. Geophones pick up the tremors and interpret the data as sediment flow rates. Controlled experiments and physical modelling shown that information, such as the grain size of transported particles, may be taken out from additional factors, such as the amplitude and frequency of the collected signal [72]. In another study, different grain sized rock drilling was differentiated on the basis of vibration signal. On the basis of examination of vibration signals recorded while drilling into various rock samples using a diamond impregnated drill bit on a laboratory drilling setup, it can be asserted that under consistent drilling conditions, both the disintegration process and the resulting fragmented rock display distinctive vibration patterns across time, frequency, and time-frequency domains. In the frequency domain, the vibration spectrum of materials with bigger grains showed greater amplitude components at low rotation speeds. Unique grain diameters of the studied materials were represented in the spectrograms by having distinct dominating frequencies and peak acceleration amplitudes. During the analysis of vibration data in the frequency domain, it was observed that there exists a polynomial correlation between the drilling rate and the vibration signal [75]. Another research work has been carried out to collect information about the rock structure based on the vibration signal analysis. The spectral properties of the sound or vibration signals produced during rock drilling operations were studied in relation to the mineral particle sizes using both numerical simulation and experimental methods. The results showed that the proportion of high-frequency sound and vibration increased as the aggregate size decreased. The aggregate sizes of the rock samples were varied in order to conduct several drilling

tests. Data from the vibrations were acquired using an indoor signal capture and processing system, and distinctive signals were then extracted. This study offered an alternative technique for evaluating the rock structure data collected via vibration from drilling [74]. Apart from this, grain size of the material was also studied based on the behavior of ultrasonic waves in low carbon steel. Using the acoustic resonance method, the precise measurement of ultrasonic wave attenuations in low carbon steels was conducted. Velocities were directly computed based on resonant frequencies and material thicknesses, while attenuations were determined by observing the decay of a signal from resonant vibration after halting external excitation at the selected resonant frequency. Average grain size and yield strength were shown to correlate well with attenuations measured at a frequency of around 5 MHz. Industrial applications for the findings include real-time assessment of grain size and mechanical strength of steels [73].

Lastly, to differentiate self-lubricating level based on the vibration signal, an attempt has been made by the researcher by taking two different coated bearings. One is coated with Al_2O_3 deposited using plasma thermal spray (NBC30205), while the other is coated via physical vapor deposition with wear-resistant carbon coating. The vibration signals of these two bearings were recorded after running at three distinct linear velocities under load conditions. The statistical moments of these vibration signals were computed, and the results were presented in the context of coating properties. As this coating is self-lubricating, the results demonstrate that bearings with a wear-resistant carbon coating have reduced statistical moment values. By calculating the RMS of the Fast Fourier transform, the spectral constituents of these signals were also determined, with the carbon-coated material yielding a lower value than the Al_2O_3-coated bearing. Due to improved lubrication, the lower value of spectral content reveals that the signal's harshness is significantly reduced. Randomness of spectral contents exhibits the greatest variation among all the analyzed parameters and proposed as a benchmark for analyzing the various levels of self-lubrication [80]. Based on the above discussed literature, it is advent that effect of change in material properties can be sensed by analyzing the variation in vibration signals by establishing a suitable relationship.

To improve the properties of bearing and hence life, most of the reputed bearing manufactures like SKF, NSK, FAG, RBC are using different types of surface coatings. Over a period, due to continuous running, the coating characteristics of bearing are bound to degrade but there are no techniques available to check the deterioration of the coating properties. Either the bearing needs to be dismantled or destroyed and is impossible to reuse the bearing for the same application. To overcome this challenge, this study will provide insight about the probable techniques that could be used to evaluate the bearing coating properties without damaging the bearing elements. After getting complete insight about most used techniques to measure properties, best possible would be recommended for checking coating deterioration without dismantling or destroying the bearing. Moreover, in actual conditions, the load on the bearing could be varying depending upon the application, as result it is challenging to estimate the bearing life effectively with the available formulas.

3. Hypothesis

From literature review, it is clear that there is a need to have an on-board technique to assess the level of properties of material. An evaluation technique is required which can work without dismantling the workpiece and can keep the component in shape during evaluation also i.e., nondestructive in nature. Although, numerous non-destructive techniques like Thermography, Ultrasonic testing, Radiography, Eddy current testing, Magnetic particle testing, Acoustic emission analysis, Dye penetrant testing and Vibration signal analysis are in use to monitor the state of the machine. But vibration signature analysis remains to be a preferred choice of researchers due to its ability to identify minute variations in the system from normal working condition. That is why in this research work, to compare the level of different properties of bearing coating, vibration signature analysis has been selected.

4. Objectives

- To coat the bearing mating surfaces with different materials to achieve various levels of surface properties.
- To measure and characterize surface properties of bearing coatings using conventional techniques
- Development of correlation for each material property with the relevant statistical parameter of the vibration signal of coated bearing element. So that, bearing surface properties could be evaluated while the bearing is in running condition, based on statistical analysis of the vibration signal.

5. Methods and Materials

In this research work, a ball bearing, NBC make, Model no: 6205 has been used for experimentation. It falls under the category of deep groove ball bearings. The single row deep groove ball bearing boasts minimal friction, noise, and vibration which make them ideal for use at high rotational speeds. Compared to other bearing types, they are more durable, easier to install, and require less maintenance for radial and axial loads in both directions [81].

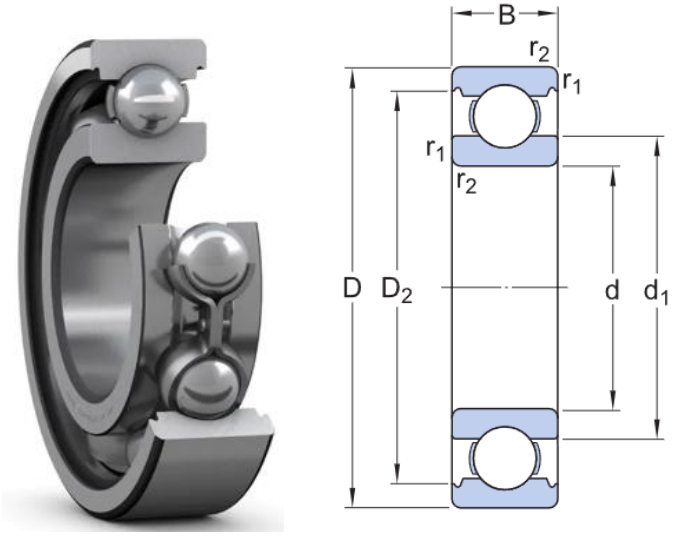

Figure 15: Sectional view of 6205 ball bearing [81]

Table 1: Technical specification of 6205 ball bearing [81]

Symbol	Value	Entity name
D	52 mm	Outside diameter
d	25 mm	Bore diameter
B	15 mm	Width
D_2	≈46.21 mm	Recess diameter
d_1	≈34.35 mm	Shoulder diameter
$r_{1,2}$	min.1 mm	Chamfer dimension

Table 2: Calculation data of 6205 ball bearing [81]

Parameter	Value
Basic static load rating	7.8 kN
Basic dynamic load rating	14.8 kN
Fatigue load limit	0.335 kN
Limiting speed	18, 000 rpm
Reference speed	28, 000 rpm
Mass of bearing	0.13 kg

Total 10 bearings are procured from bearing manufacturer and divided into two sets of 5 each. Each bearing in both sets were disassembled using the facility of manufacturer only. Later, each bearing from both sets were coated with a specific material as per the industrial standards. The coating used for the bearing in this study are: Nickel, Copper, Silver, Zinc Phosphate and Black Oxide. First three coatings are carried out with the process of electroplating and last two with chemical conversion process.

5.1 Electroplating

Electroplating involves immersing the bearing in a metal salt solution as a cathode, and required coating material like zinc as anode, followed by the passage of electricity to initiate chemical reaction process. In order to supply the electrical energy required for the plating process, they are wired to the power source, often a direct current (DC) power supply. An electrical current flow through the circuit when power is supplied, which draws metal ions from the electrolyte and directing them toward the cathode (substrate). At the cathode, the metal ions gain electrons and deposit as a metallic layer on the substrate after being reduced. The anode is responsible for replenishing the electrolyte with metal ions because this is where the metal is oxidized before being dissolved in the electrolyte. Prior to electroplating process, surface preparation is an important step where the substrate, such as a metal object or a plastic component, is extensively cleaned to remove any dirt, grease, or oxides. Typically, this is accomplished through a sequence of chemical degreasing, mechanical scouring, and rinsing steps. To ensure excellent adhesion and quality of the plated layer, it is imperative that the substrate should be clean. After cleaning the base metal, there are important parameters to be controlled during the electroplating process apart from

assigning cathode and anode after immersion in the electrolyte. These important parameters along with their significance are discussed further.

- **Preparation of base material**: To ensure high adherence and quality of the plated layer, surface pretreatment of the substrate prior to plating is essential. Adhesion between the substrate and the plated metal depends on factors including controlling the cleaning, activation, and etching processes, which remove impurities, prepare the surface for plating, and promote adhesion. That is why, the surface of bearing elements was thoroughly cleaned before the electroplating. After being cleaned of oil with hot aqueous alkali and acetone, the substrates were mechanically polished and immersed in a 10% (volume fraction) hydrochloric acid solution for 8-10 seconds to activate the surface.
- **Plating time**: The thickness of the plated layer depends on how long the substrate is submerged in the plating bath. In order to avoid under- or over-plating, the plating duration must be precisely managed to reach the target coating thickness. The plating time is directly linked with required coating thickness, which typically ranges from 3 to 6 minutes in this work, whereas the coating uniformity is highly dependent on the rate of withdrawal from the reservoir [82].
- **Current density**: How much electricity flows through the plating solution per square centimeter of the substrate is measured in terms of current density. Current density is commonly expressed as a ratio of amperes per centimeter squared (A/cm^2). Because it impacts plating velocity, thickness, and homogeneity of the deposited metal, controlling the current density is critical. Coating surface morphology is significantly impacted by plating current density. Very small platelets, measuring less than 1 m in size, were seen when the current density was raised from 30 mA/cm^2 to 48 mA/cm^2. There were also microcracks visible all the way through the coatings. Microcracks were more prominent when a lower current density was used [83].
- **Temperature**: The rate of plating and the grade of the deposited metal are affected by the temperature of the plating bath. Various metals have distinct temperature requirements for optimal gilding outcomes. Monitoring and regulating the temperature of the bath is essential for maintaining process consistency and

ensuring uniformity. The processing temperature in electroplating are usually below 100° C.

- **Voltage**: The rate of metal deposition during plating is controlled by the applied voltage or current. The plating rate cannot be adjusted or problems like burning or surface roughness can be avoided without careful voltage regulation.
- **Composition of Bath**: To get the proper plating results, it's crucial to know the exact composition of the plating bath or electrolyte solution. Factors such as metal ion concentration, pH, temperature, and the presence of additives or brighteners are all considered. To achieve consistent quality of plating, bath should be maintained in a controlled manner.
- **Agitation**: By stirring the plating fluid, concentration gradients of metal ions can be avoided, resulting in more uniform plating. By mixing the solution thoroughly, we can prevent faults like voids and roughness on the plated surface and guarantee uniform deposition. The plating technique and bath composition determine the type of agitation and the degree to which it must be applied.
- **Configuration of Anode**: The distribution of current and metal ions during plating can be affected by the selection and placement of anodes in the plating solution. Uniform plating thickness and the avoidance of problems like edge buildup or uneven deposition necessitate careful consideration when selecting and installing anodes.

  After coating nickel, copper, and silver on the bearing elements using process of electroplating as explained above. Next two coatings i.e., zinc phosphate and black oxide were coated with the help of chemical conversion process.

Table 3: Electroplating parameters used in the process

Coating Material	Current density (A/dm^2)	pH value	Mean Thickness (µm)	Deposition rate (µm/min)	Temperature (^0C)	Plating time (minutes)	Bath Composition
Nickel	5	3.4	18.54	1.8	60	10	Nickel Sulfate (240–300 g/L), Nickel Chloride (30–60 g/L), Boric Acid (30–40 g/L)
Copper	5	1.8	21.47	1.2	35	18	Copper Sulfate (150–250 g/L), Sulfuric Acid (50–80 g/L), Chloride Ions (50–100 mg/L)
Silver	5	9	20.09	0.7	25	30	Silver Cyanide (25–50 g/L), Potassium Cyanide (75–150 g/L)

5.2 Chemical conversion Process

The term "chemical conversion coating" refers to a surface treatment method in which a fine protective layer is generated on the surface of a substrate through the application of a chemical solution. The substrate's surface reacts with a chemical solution or substance in this process. Metals like aluminum, magnesium, zinc, and steel frequently undergo chemical conversion to improve their corrosion resistance, serve as a foundation for later coatings or paints, increase adhesion, or otherwise alter their surface qualities. Chemical conversion coatings come in a wide variety of styles, each optimized for a certain set of properties in combination with the substrate material. Some common chemical techniques for transforming metals are discussed further:

- **Phosphate Conversion Coating:** Steel and iron surfaces are often coated with phosphate conversion coating. It entails applying a solution containing phosphoric acid or phosphate salts to the metal surface. Phosphate conversion compounds offer corrosion resistance, improve paint adhesion, and can serve as a base for lubricants and oils. For instance: Zinc phosphating is also used on bearing surfaces by the manufacturers.
- **Black Oxide Coating:** Coating steel, stainless steel, or copper with a layer of black oxide also called blackening or blackening oxide, is the result of a chemical conversion process. Producing the black oxide layer that provides corrosion resistance and enhances aesthetics requires treating the metal surface with an alkaline solution or a mixture of chemicals. Black oxide coating is also carried out by the bearing industry.
- **Chromate Conversion Coating:** The coating of chromate conversion, also known as chromating or passivation, is commonly employed for zinc and aluminum. Chromates, phosphates, or other chemical compounds are used in a solution to treat the metal's surface. Corrosion protection and better adherence for later paints and coatings are both provided by chromate conversion coatings.
- **Anodizing:** Aluminum and its alloys undergo a unique chemical conversion process called anodizing. The aluminum is submerged in an electrolytic solution, and an electric current is then used to create an oxide coating on the metal's surface.

A variety of artistic and practical anodized coatings can be achieved, and corrosion resistance is greatly increased.

Table 4: Phosphating and black oxide process parameters

Process	pH value	Mean Thickness (µm)	Temperature (^{0}C)	Time (minutes)	Bath Composition
Phosphating	3.4	17.5	55–65°C	20	Zinc Phosphate (30–50 g/L)
Black Oxidizing	>12	2	135–145°C	30	Sodium Hydroxide (500–550 g/L), Sodium Nitrate (100–200 g/L)

5.3 Step by step procedure of Phosphating/ Black Oxidizing

Typically, a protective layer of zinc phosphate or black oxide is formed on the surface of AISI 52100 through a chemical conversion procedure. The following is an outline of the process required to apply zinc phosphate or black oxide coating on AISI 52100.

- **Surface Preparation:** It is very important to remove any debris, oil, rust, and scale from the AISI 52100 steel surface. Degreasing, alkaline cleaning, and mechanical cleaning (sandblasting, wire brushing) are all effective ways to do this. Zinc phosphate or black oxide coatings require a clean, contaminant-free surface to adhere successfully.
- **Activation:** Apply an acidic activator solution to the cleansed surface. This process aids in the elimination of any lingering oxides and helps prepare the surface for the zinc or black oxide coating. In most cases, an acidic cleanser or acidic phosphate solution is used as the activator solution. Concentration and duration of immersion should be determined in accordance with manufacturer recommendations.

- **Immersion:** The treated AISI 52100 steel must be submerged in the zinc phosphating solution. In case of black oxide coating, sodium hydroxide (caustic soda) and sodium nitrite, together with a few additional secret ingredients, make up the bulk of the black oxide solution. For a uniform coating, make sure the entire component to be coated has been completely submerged in the solution. Time in immersion will be determined by coating thickness and manufacturer-recommended procedure parameters. Immersion times often varies from few minutes to long time.
- **Rinse:** Rinsing the coated AISI 52100 steel with water after the zinc phosphating or black oxidizing process removes any remaining solution and by-products from the treatment, protecting the coating against residues and extending its life.
- **Drying:** Use methods such as air drying or forced hot air to dry the AISI 52100 steel that has been coated. Before proceeding with any packaging or handling, be sure the coating is totally dry.

5.4 Characterization of material properties

After coating the bearing elements with electroplating and chemical conversion process as per the nature of coating, the properties of these coatings were evaluated. As already discussed earlier, along with grain size, important properties of bearing coating considered in this work are: Surface roughness, Hardness, Wear resistance and Self-lubricating level. Further, description of all these properties is presented one by one, followed by its measurement method used in this work.

5.4.1 Surface Roughness

Starting with surface roughness, mostly termed as roughness, is a component of surface finish. It is determined by the extent to which an actual surface deviates from its ideal shape along the normal vector. If these variations are significant, the surface is considered rough; if minimal, it is deemed smooth. In surface metrology, roughness is commonly identified as the high-frequency, short-wavelength aspect of a surface under measurement. Assessing both the amplitude and frequency of roughness is often necessary to ensure surface suitability for a particular purpose. Roughness essentially

dictates the interaction of a real object with its environment. In tribology, rough surfaces typically exhibit higher friction coefficients and experience accelerated wear compared to smooth surfaces. Moreover, surface irregularities can act as initiation points for cracks or corrosion, utilizing roughness as a dependable indicator for the performance of mechanical component performance. Roughness can be assessed manually using a surface roughness comparator in reference to a sample of defined surface roughness, but more frequently, a profilometer is used to quantify the surface profile which could be optical (e.g.: a white light interferometer) or contact based which is usually a diamond stylus. For measurement, Mitutoyo made, Model: SJ-410 surface roughness tester has been used in this work as shown in Figure 16. Surface roughness level has been measured of coated bearing races before and after operation as presented in Table 5. Different units like arithmetical mean roughness (R_a), maximum height (R_y), ten-point mean roughness (R_z), mean spacing of profile irregularities (S_m), mean spacing of local peaks of the profile (S) and profile bearing length ratio (t_p) are in use to measure the surface roughness, whereas R_a is most widely used term to measure the roughness mainly due to historical reasons, as earlier mostly testers used to give readings in R_a only, there is no other specific benefit of choosing R_a to define roughness level.

Table 5: Surface roughness level (R_a) of coated bearing element

S. No	***Coated Material***	***Surface Roughness Indicator (R_a) (Before Operation)***	***Surface Roughness Indicator (R_a) (After Operation)***
1	Nickel	0.29	0.29
2	Copper	0.52	0.53
3	Zinc Phosphate	0.71	0.71
4	Silver	2.65	2.66
5	Black Oxide	3.22	3.25

Figure 16: Surface roughness tester used to measure roughness level of coated bearing races [85]

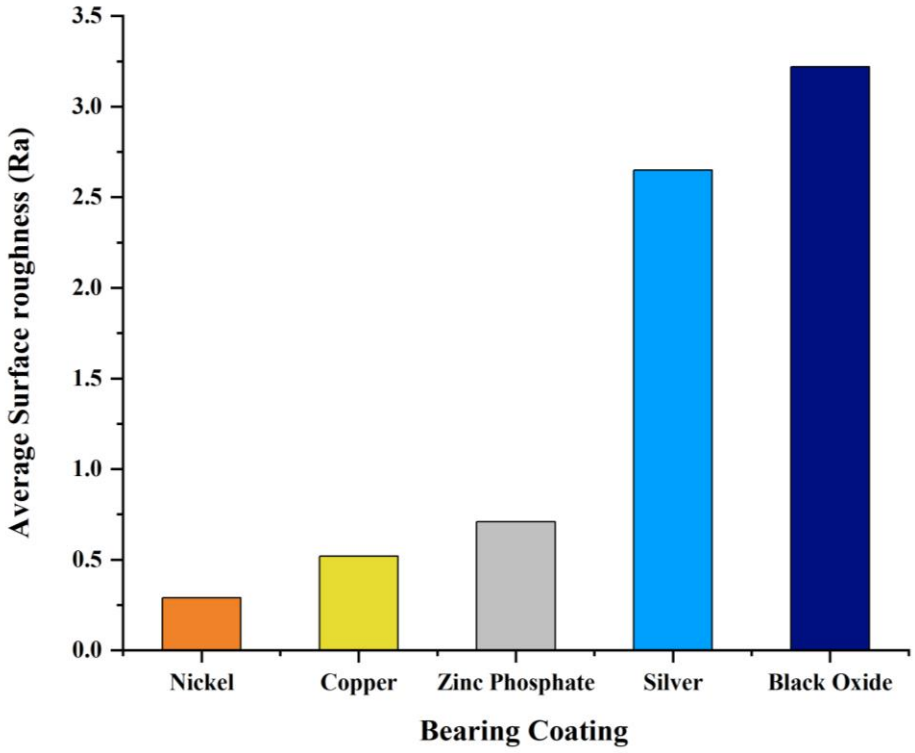

Figure 17: Average surface roughness (R_a) plot of bearing coating

5.4.2 Hardness

A material's hardness is assessed based on its capacity to endure localized permanent deformation, often resulting from indentation. Furthermore, it reflects the material's resilience against deformation against abrasion, penetration, or scratching. Hardness is a significant factor in numerous applications of engineering design, as it plays a pivotal role by directly impacting the performance and appropriateness of the material. For example, as hardness increases, a component's resistance to wear generally improves. As hardness is not a fundamental characteristic of a material, it must be understood in relation to other characteristics like strength, elasticity, and ductility. For instance, a substance may be hard but also brittle. This characteristic may restrict the use of the item in particular applications. Therefore, it should be within required limits for smooth functioning of the machine element. This is crucial for mechanical equipment like bearing that has moving parts where metal components come in contact with other metal or containments. In order to ensure less wear and a longer service life, the hardening process during production is essential. Additionally, hardening offers the physical qualities that develop the optimal physical characteristics for the bearing. Therefore, it is important to retain this property during the functioning of the bearing, as degradation of the same may lead to failure of the component. However, the process of degradation is not happening at a noticeable rate so it is impractical to define a time period when hardness is going to be get effected. Therefore, onboard technique is required to monitor the hardness level without dismantling the component again and again during its working life. However, Conventionally, the surface hardness of the coated bearing has been measured using Vickers Hardness tester (Make: OmniTech, Model: S-Auto), same has been used in this work to measure hardness of bearing coating as shown in Figure 19 and measured values are mentioned in Table 6. Five sample readings of the same surface at different locations have been taken then mean of the five values has been considered as the final hardness value of each coated bearing. The values are taken in HV, Vickers hardness number. This process of measuring hardness is based on indentation only where a diamond shaped stylus forced to penetrate into the surface and leave its impression which is to be evaluated with the help of microscope.

Table 6: Vickers Hardness number (HV) of coated bearing

S. No	*Coated Material*	*Vickers Hardness Number (HV) (Before operation)*	*Vickers Hardness Number (HV) (After Operation)*
1	Silver	192	192
2	Copper	491	489
3	Zinc Phosphate	539	538
4	Nickel	614	611
5	Black Oxide	624	623

Then, the dimensions of the indentation, a diagonal formed into the surface after penetration has been proportionally converted into HV number by dividing the test force with surface area of the indentation which is then displayed on the screen as measured output value.

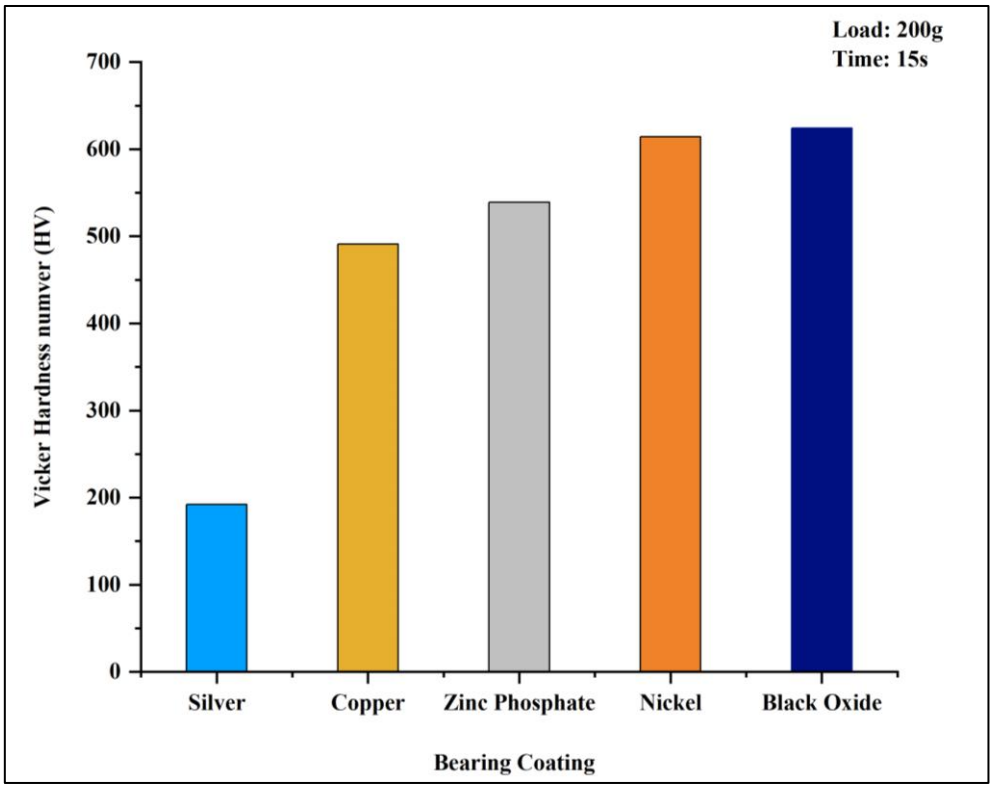

Figure 18: Microhardness plots of the coating

Figure 19: Vickers hardness tester used to measure hardness of coated bearing races

5.4.3 Wear Resistance

Wear resistance refers to a material's capacity to withstand extensive external forces throughout service, including abrasion, edge cutting, impact, and so on. It is possible for a material to have high wear resistance and toughness without being extremely hard, and vice versa. On the other hand, the ability of a material to absorb impact energy and bend (either elastically or plastically) without breaking is known as its toughness. For instance, tires of a car. Tires are not that challenging. Tires are remarkably resilient, springing back from even severe distortion (elastic deformation) caused by anything as small as a fingernail. Even if a tire is perpetually deformed (plastic deformation), it rips or breaks infrequently. Despite traveling on much harder surfaces, such as concrete, these tires last a very long time to wear out. In addition, they are shock and temperature-resistant. Tires are durable, deformable, able to sustain a great deal of energy prior to failure, and resistant to wear, but they are not particularly hard.

For the wear testing, Pin-on-disc measurement involves pressing an indenter or pin (typically flat or spherical) against a test specimen. With the rotation of test specimen,

the engagement mechanism applies a precise force to the indenter. Using a strain gauge sensor, the resulting friction forces are determined. Wear coefficients can be determined for both the pin and the sample by assessing the quantity of material lost throughout the testing process. Pin-on-disc can be used to determine the wear resistance of a coating, as well as its coefficient of friction, lubricity, and adhesion properties. A surface exhibiting low friction coefficient and high lubricating properties will allow the pin to roll more readily on the surface, reducing material loss and enhancing wear resistance. In contrast, the pin's tension would cause a coating with inadequate adhesion to break apart at the bond and peel off. This indicates poor wear resistance, even if the coating is tough.

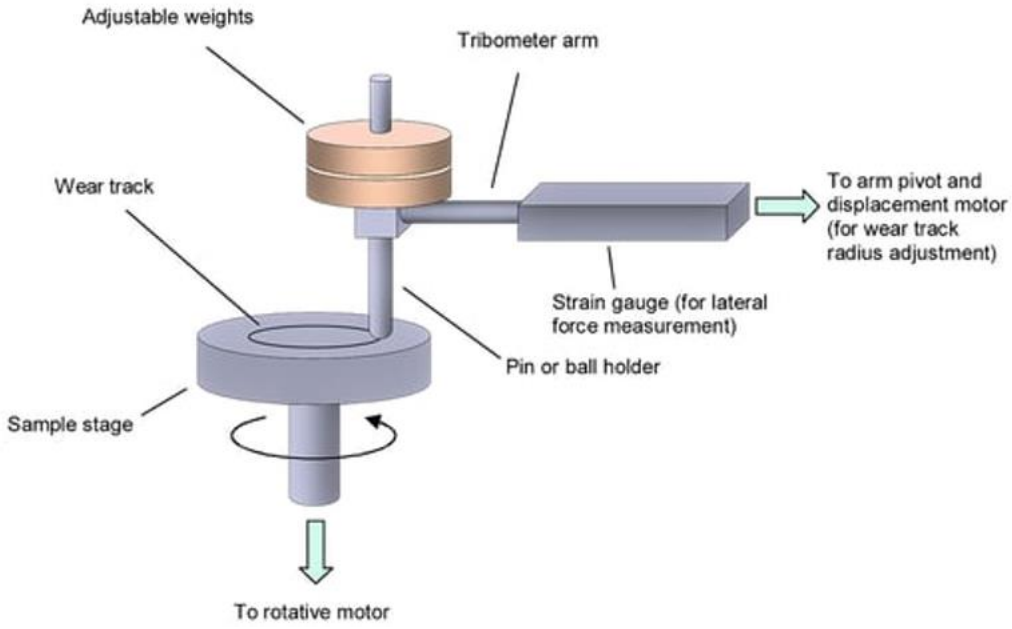

Figure 20: General layout of Pin-on-disc equipment to measure wear [86]

The wear test of the bearing coatings was conducted using pin-on-disc test according to the ASTM-G99 standard. For testing, cylindrical pin shaped samples were prepared to slide against the SiC (silicon carbide) emery sheet of 200 grit size mounted on the rotary disc of the tribometer. The diameter and length of the pin were taken as 10 mm and 30 mm respectively. After fixing the sample in specimen holder, it must slide against the SiC emery sheet mounted on the rotary disc made up of EN31 steel [8]. Table 7 gives information about the wear testing parameters used in this work. The loss

in weight of the samples after wear was evaluated with the help of weight measuring instrument (Model: ML-220, Make: Mettler Toledo).

Table 7: Parameters of abrasive wear test

Wear Test Parameters	Values
Speed (m s^{-1})	1
Load (N)	20
Track diameter of disc (mm)	80
Sliding distance (m)	5000
Temperature (°C)	30 ± 5

The abrasive wear coefficient and characteristics of cumulative weight loss of all the samples (coatings) are shown in Figure 21 and Figure 22. The equation *(4)* is used to find out abrasive wear coefficient for all samples is called as Archard's wear equation [241].

$$Q = \frac{KW}{H} \qquad (4)$$

Where K = Dimensionless parameter called as abrasive wear coefficient

Q = Wear rate (g m^{-1})

W = Load (N)

H = Sample Hardness

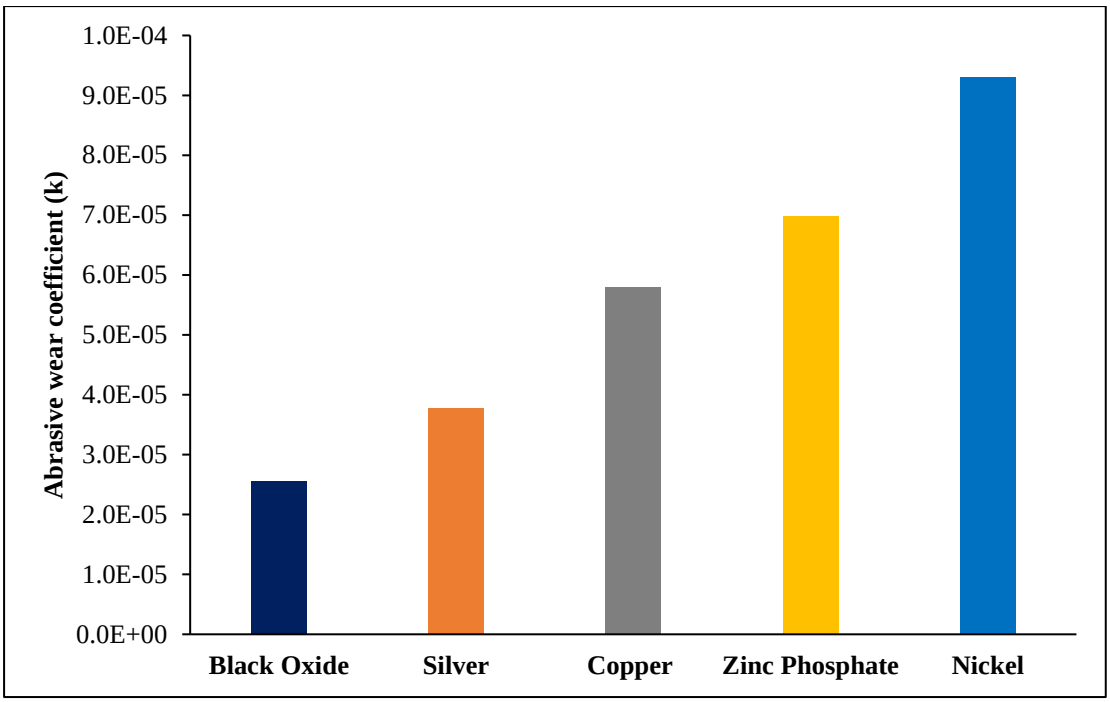

Figure 21: Abrasive wear coefficient for all coatings

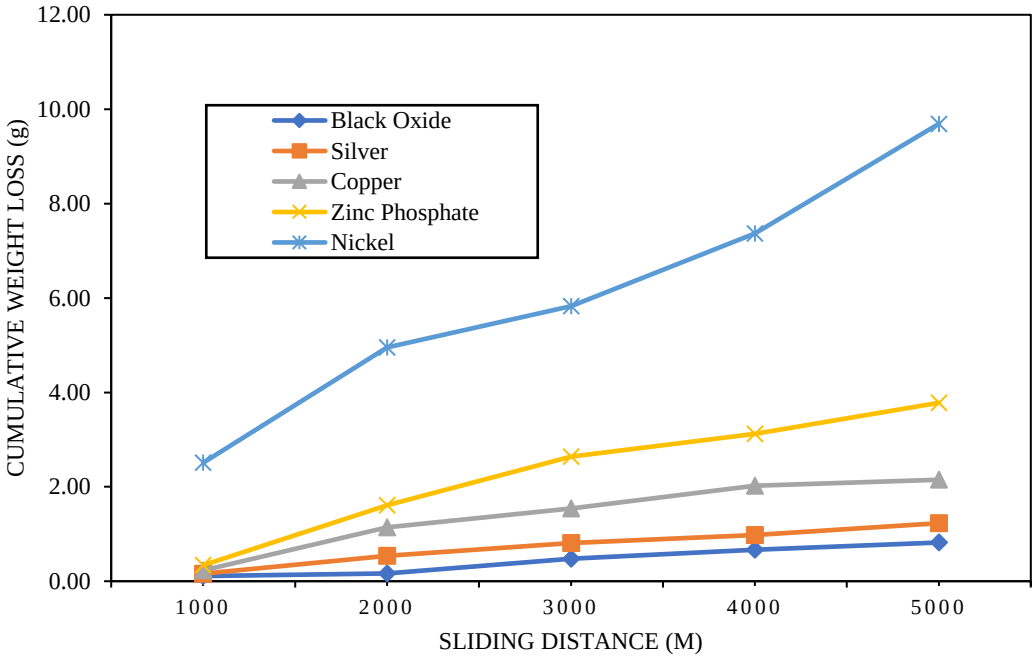

Figure 22: Cumulative weight loss w.r.t sliding distance

Figure 23: Pin on disc apparatus to measure wear rate [86]

5.4.4 Grain Size

Grain size is an essential determinant of a material's mechanical properties and corrosion behavior. The mechanical properties of material such as fatigue, creep, yield strength, and impact transition temperature, are affected by the grain size. The particle sizes can have a substantial effect on the macro-scale mechanical response. Altering grain size will impact the volumetric number density of interactions between grains and the geometric configuration of their surroundings, solely from a geometric perspective. Moreover, grain size variation can affect the initial rigidity and damage behavior of grain-pair interactions. The mathematical description of the macroscopic response of granular materials must start with the concept of grain-interactions. According to the traditional Hall-Petch equation, grain size is significant: yield strength decreases as the square root of the grain size increases. Grain size also influences both hardenability and critical plastic flow properties [87]. Therefore, estimating the grain size of a material can be extremely beneficial. Conventionally, grain size is measured using optical photomicrographs or by observing the microstructure under a microscope. In comparison to optical microscope, higher magnification and in-depth details can be obtained using Scanning electron microscope (SEM). Employing a focused beam of high-energy electrons, the scanning electron microscope (SEM) produces a variety of signals on the surface of solid specimens. Signals resulting from electron-sample interactions disclose data of the specimen, such as its surface morphology, chemical composition, and crystalline structure and orientation of the sample's constituent materials. In most applications, data are collected over a specific region of the sample's surface, and a two-dimensional image displaying spatial variations in these properties is generated. With conventional SEM imaging methods, one can capture areas ranging from about 1 cm to 5 microns wide in scanning mode, with magnifications ranging from 20X to approximately 30,000X and a spatial resolution of 50 to 100 nm. Additionally, the SEM can conduct point-by-point analyses of the sample, which proves especially beneficial for qualitative or semi-quantitative assessments of chemical compositions using energy dispersive X-ray spectroscopy (EDS), crystalline structure, and crystal orientations, with the aid of diffracted backscattered electrons (EBSD). Considerable quantity of kinetic energy is conveyed by accelerated electrons within a SEM. This

energy disperses as diverse signals arising from the interactions between electrons and the sample, these phenomena occur as incident electrons slow down within the solid specimen. These signals include secondary electrons, which produce SEM images, backscattered electrons (BSE), and diffracted backscattered electrons (EBSD), used to determine crystal structures and mineral orientations. Additionally, photons emit characteristic X-rays for elemental analysis, alongside continuum X-rays, visible light, and heat. Primarily, the SEM is employed for producing high-resolution images illustrating object morphologies (SEI) and for unveiling spatial differences in chemical compositions. This includes tasks such as obtaining elemental maps or conducting spot chemical analyses using EDS, distinguishing phases by mean atomic number (typically associated with relative density) using BSE, and generating compositional maps based on variances in trace element "activators" (usually transition metals and Rare Earth elements) [87]. Therefore, in this work, SEM is used to measure the grain size of coated material. For this purpose, second set of coated bearing has been used after cutting out a rectangular piece from inner and outer race using slow speed (200 rpm) diamond cutter (Make: Chennai Metco). After cutting, sample preparation has been carried out to get better results during SEM analysis. Each piece is etched with suitable acid followed by gold plating on the surface to be inspected. Etching represents a chemical or electrolytic procedure commonly employed prior to microscopic surface analysis. In materialgraphy, etching intentionally alters the surface profile or optical properties at grain boundaries, phases, or grain surfaces. This aids in microscopic examination and the additional use of optical filters.

5.4.4.1 Steps to be followed in etching process [88]:

a) Pre-polishing of the specimen necessitates a smooth, deformation and scratch-free surface.
b) The appropriate etching solution for the material is chosen based on information obtained from the literature as shown in Table 8.
c) In certain instances, light microscope filters could be utilized in conjunction with chemical etching for better contrast. This process is known as "optical etching."
d) Electrolytic etching requires the selection of an appropriate electrolyte, voltage, and sample exposure duration.

Table 8: Etchant used for different coated elements

S. No	*Coated Material*	*Acid used for etching*	*Time of etching in seconds*
1	Nickel	Sulfuric acid	2
2	Copper	Nitric acid	2
3	Zinc Phosphate	Sulfuric acid	2
4	Silver	Hydrofluoric acid + water (in same proportion)	30
5	Black Oxide	Hydrofluoric/ Nitric acid	3

5.4.4.2 Types of Etching [88]

a) Chemical Etching: Chemical etching involves fully submerging a sample, which is ground for macro etching or finely polished for micro etching, into an etching solution (etchant). Macro etching allows for visual inspection of the sample surface either with the naked eye or under a magnifying lens (up to 25x magnification). Micro etching facilitates microscopic examination at magnifications of 1,000x or more, utilizing either light microscopy or electron microscopy. The dissolution etching process enables targeted attacks on grain boundaries, surfaces, and phases. In precipitation etching, alternatively known as color etching, a thin layer develops on the surface, its thickness determined by the chemical composition or particle orientation.

b) Electrolytic Etching: Electrolytic etching necessitates a uniformly conductive workpiece. Initial surface preparation typically involves brief mechanical grinding and furbishing to achieve better even surface, albeit with potential deformation and scratches. Unlike mechanical methods, electrolytic polishing tends to minimize edge rounding and potential phase discharge while reducing deformation. The underlying principle of electrolytic etching mirrors that of chemical etching, except that the specimen serves as the anode within a galvanic cell, resulting in material removal from the specimen's surface. For specialized investigations involving aluminum-based materials, electrolytic ablation can be employed to produce an anodized layer on a meticulously furbished specimen surface, which can then be examined using polarized light (known as Barker-etching).

Although, in this work, only chemical etching has been done followed by gold sputtering. Throughout history, gold has maintained its status as the preferred material for sputter coating. Its high conductivity and relatively fine grain size contribute to enhancing the signal-to-noise ratio in SEM imaging, thereby producing higher-quality images and rendering it optimal for analysis. After gold plating, the samples are mounted on holder with the help of carbon tape as shown in the Figure 24.

Figure 24: Coated bearing samples after cutting and gold sputtering mounted on SEM holder with carbon tape

SEM analysis has been carried out on JEOL make machine, Model No: JSM-7610F Plus as shown in Figure 25. However, it is required to measure grain size with an onboard technique. The optical microscopic methods are time-consuming and frequently require cutting samples from the material which is impractical during working conditions [93].

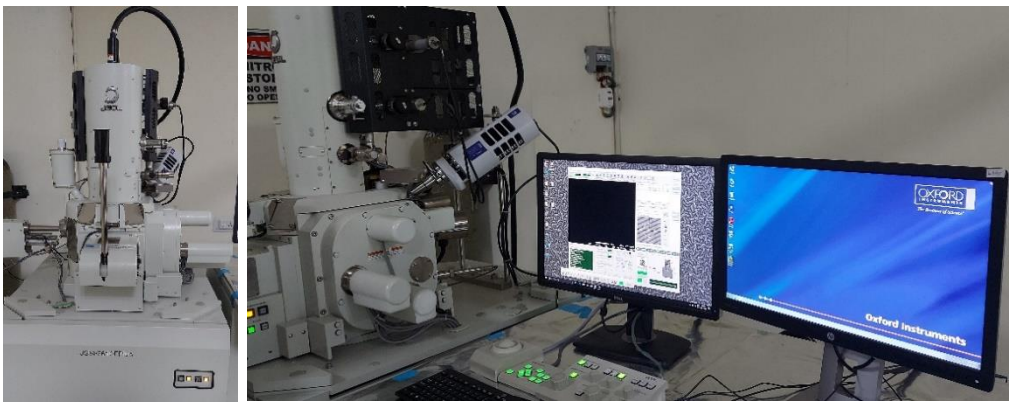

Figure 25: Machine used for SEM analysis to measure grain size of bearing coating

Table 9: Grain size of bearing coating

S. No	***Coated Material***	***Grain size diameter (nm)***
1	Nickel	22.25
2	ZnP	24.16
3	Copper	24.92
4	Silver	26.8
5	Black oxide	78.48

The conventional techniques discussed above for the evaluation of properties of coated material needs dismantling of the workpiece which adds to idle time. Therefore, an onboard method is required to assess the level of these properties when the component is in running condition. In this work, vibration signature analysis technique has been utilized to compare the different level of properties for the bearing coating. All coated bearings were made to run using a customized bearing test rig and their vibration signals were recorded at five different speeds i.e., 300, 600, 900, 1200 and 1500 rpm. The statistical analysis of the captured signals was carried out using relevant signal processing techniques. Then, correlation between the coating properties and statistical parameters of vibration signal have been developed.

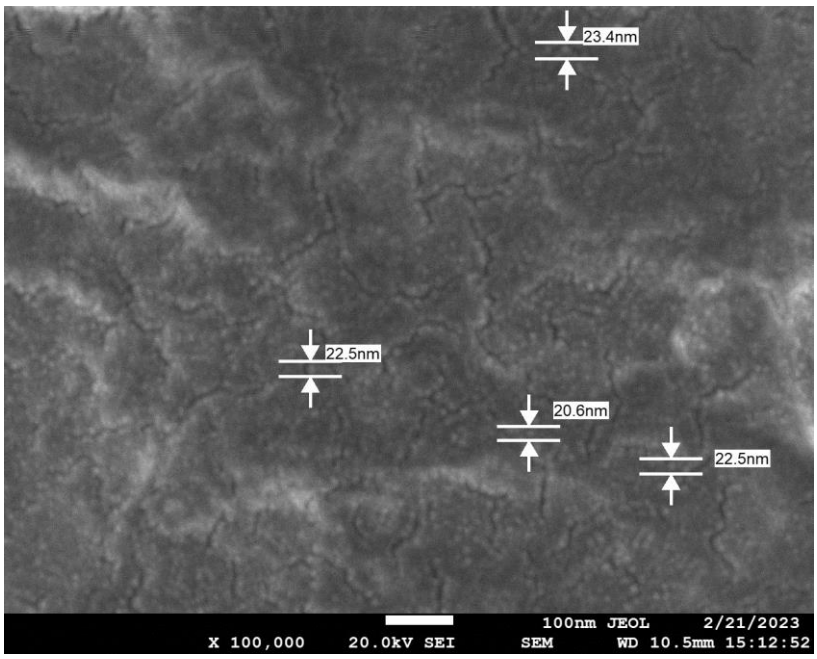

Figure 26: SEM micrographs of nickel coating

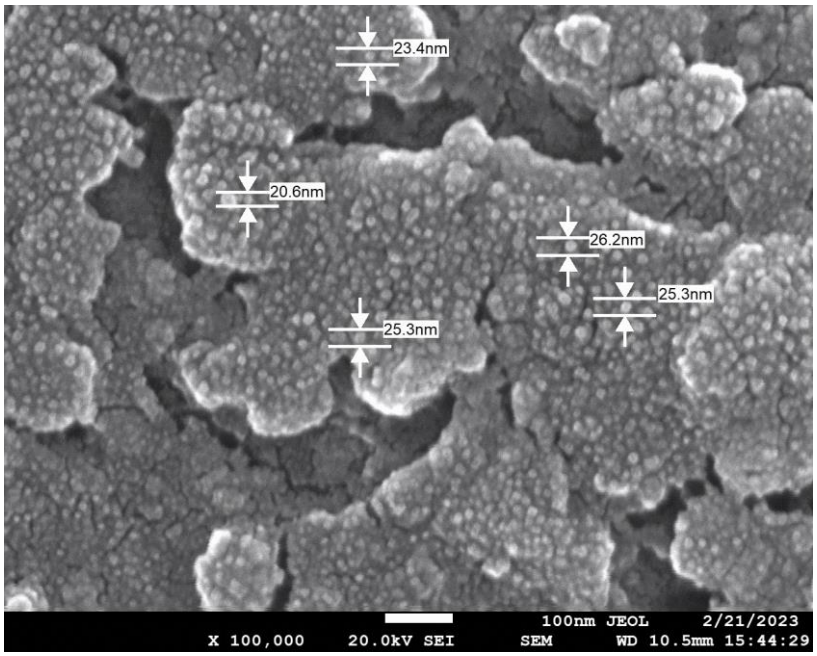

Figure 27: SEM micrographs of zinc phosphate coating

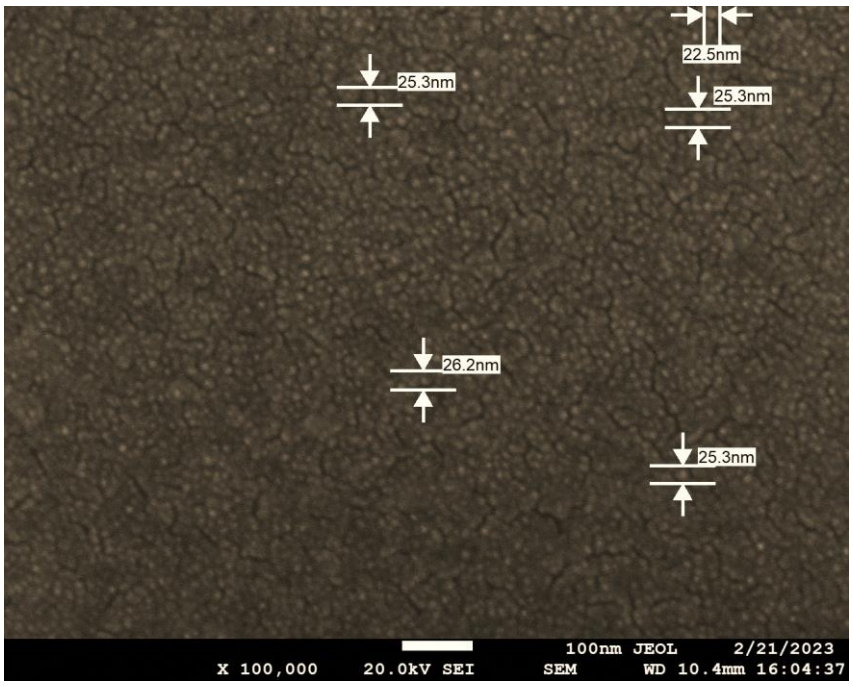

Figure 28: SEM micrographs of copper coating

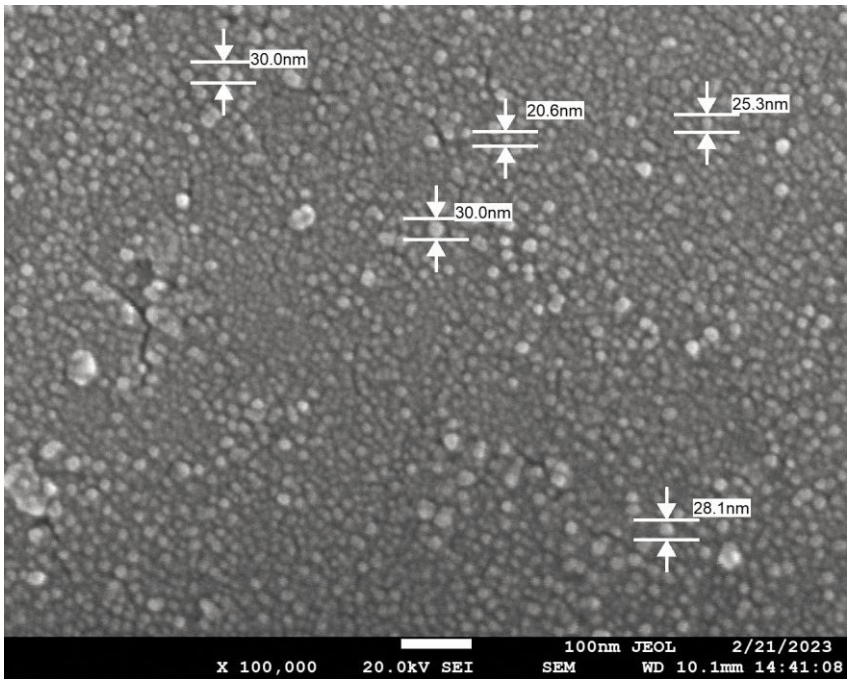

Figure 29: SEM micrographs of silver coating

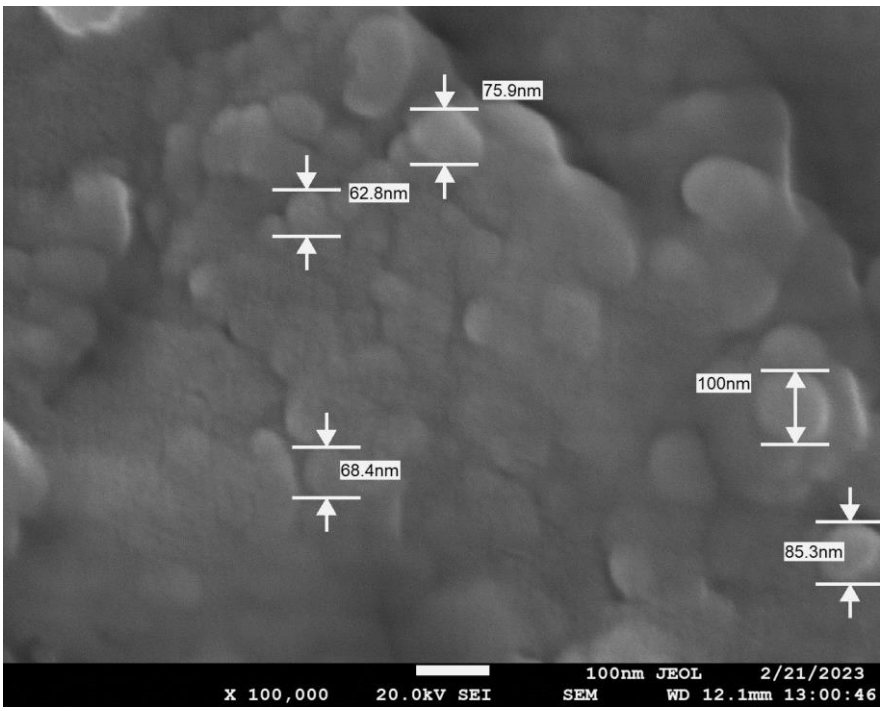

Figure 30: SEM micrographs of black oxide coating

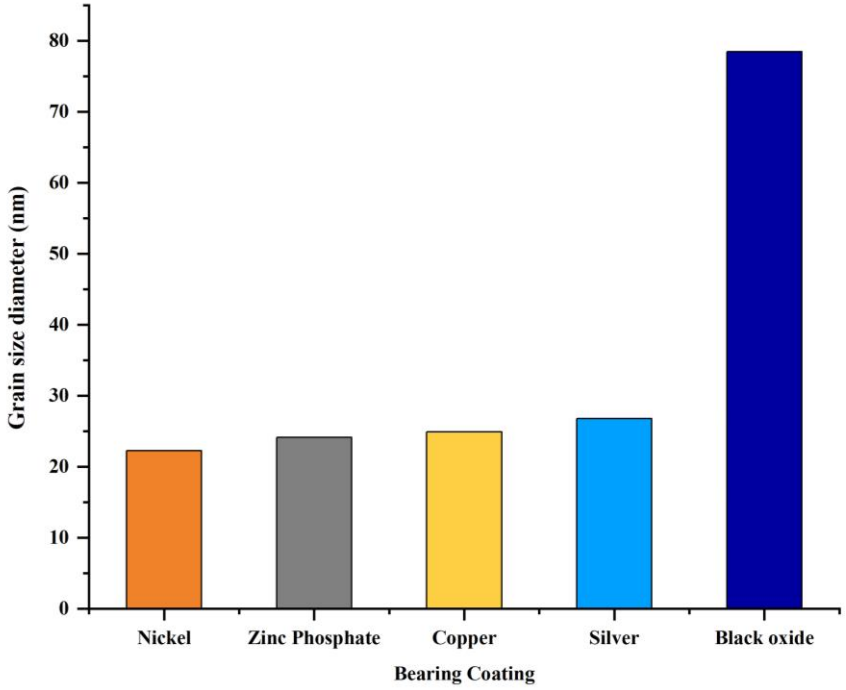

Figure 31: Plot of grain size diameter of bearing coating

5.4.5 Self-lubricating level

The ability of the bearings to transfer minute quantities of material to the mating surface is what makes them self-lubricating. This method of transmission results in a layer that lubricates and decreases friction along the whole shaft. Self-lubricating bearings have various benefits over their greased counterparts. Because there is no oil, disposal, or cleanup of hazardous materials to worry about, self-lubricating bearings reduce the cost and inconvenience of preventative maintenance. Consistent frictional forces on the bearings and drive system are maintained by self-lubrication, eliminating the need for the grease or oil that attracts the impurities that wear out standard bearings. In this type, the process of providing lubrication is continuous throughout its service life. The break-in stage is the first and most important stage. It is the beginning of transfer of material to the mating surface. Several variables, including as transfer rate, load, stroke length, etc., might affect the bearing material's degree of damage during the transition. In most cases, the first transfer will take between 50-100 strokes of continuous operation to complete.

5.4.5.1 Step by step procedure of making a self-lubricating bearing

1) First step is to select a suitable base material for the bearing with required mechanical properties, specified dimensions and compatible for the given application. Commonly used materials are bronze, composites, polymers, and ceramics.
2) Next step is to select an appropriate solid lubricant with can exhibit self-lubricating behavior. Commonly used solid lubricants are: Polytetrafluoroethylene (PTFE), nylon, graphite, and Molybdenum disulfide (MoS_2).
3) These solid lubricants need to be integrated with the bearing material during manufacturing. The particles of the lubricant should be uniformly distributed within the bearing material matrix for proper lubrication.
4) The various methods used to manufacture the self-lubricating bearing are powder metallurgy, sintering, injection molding or machining.
5) The mechanism of lubricant transfer must be incorporated in bearing design by providing micro-pores or reservoirs to provide continuous supply of lubricant to

bearing surface. With the wear of bearing surface, these lubricant particles must be released gradually through transfer mechanism.

6) The surface of bearing could be treated with a layer of solid lubricant through the process of impregnation, spray coating or electrostatic deposition. Otherwise, lubricant particles can be embedded into the bearing surface with burnishing process.

5.4.5.2 Applications of self-lubricating bearing

The automotive and aerospace industries make extensive use of self-lubricating bearings. Aerospace applications require resilient, low-friction bearings to reduce the likelihood of a malfunction at altitudes of 10,000 feet or more. Additionally, many of an aircraft's components are difficult to access and service, and therefore benefit greatly from the extended service lives of self-lubricating bearings. However, it is incorrect to claim that self-lubricating bearing systems require no additional lubrication during their operational life, there is no such thing as an indefinitely lubricated bearing. Most of these systems lubricate themselves through integrated lubrication, which ultimately runs out or becomes ineffective. Therefore, it is more accurate to mention that these self-lubricating systems have a very long service life. Inspecting and maintaining the machine assemblies on a regular basis should always include lubricating these systems.

Since self-lubricating materials are developed to lessen friction and wear between surfaces, there is a strong correlation between self-lubricating level and wear rate. There is a strong association between efficient lubrication and less wear, and a lower wear rate is indicative of better self-lubricating properties [90-92]. Therefore, in this work, self-lubricating level of the bearing coating is considered based on the wear rate, which is already evaluated and presented earlier in section 5.4.3. Based on this inverse correlation between wear rate and self-lubricating level, readings of wear rate are utilized to develop a relation between self-lubricating level and statistical parameter of vibration signal.

5.5 Bearing Testing

With the help of procedure discussed above, two sets of bearing elements were coated with zinc phosphate and black oxide. Even though, two different processes were followed to coat all bearing sets but thickness of coating thickness was maintained in the range of 15-25 microns. The reason behind close tolerances of the coating thickness is the requirement of accurate assembly of the bearing elements. After coating inner and outer races of all five bearings, the process of assembly has been carried out as per the industrial standards.

Figure 32: Coated bearing elements after assembly

After coating all five sets of bearing (two bearing in each set) with the specified coatings, first set of five coated bearings has been utilized for the experimentation and second set used for characterization of material properties. The description about considered material properties of the bearing coating has already been done in the introduction chapter. Further, details about the experimentation carried out on the first set of coated bearings has been discussed.

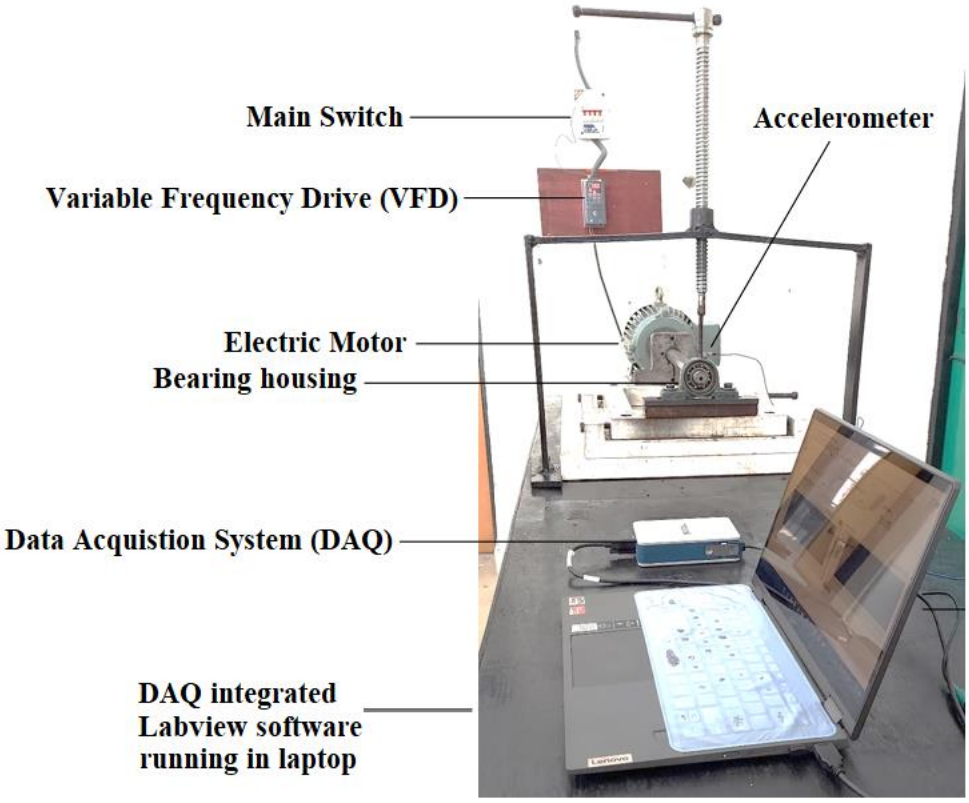

Figure 33: Customized bearing test rig

In this research work, a customized bearing set up has been developed as shown in the Figure 33. Here, the main shaft was powered by a 3-phase induction motor of 1.5 kW capacity (Make: Crompton). As depicted in Figure 33, two ball bearings are affixed at the ends of the shaft (Make: NBC Model: 6205). Using an optical tachometer, speed can be measured during an experiment. On the loading side of bearing casing, coated bearings were mounted. To measure vertical acceleration, a PCB accelerometer with a sensitivity of 990 mV/g was mounted on the bearing's upper right side. A PC-based acquisition system by National Instrument (Model: SCXI-1000 with 4 channel input) employed to capture vibration signatures. Then, an inline arrangement was made to store the captured data on the hard drive using the NI LabVIEW (2020) interface so that it can be further analyzed in MATLAB software.

5.6 Introduction to Lab-VIEW

Laboratory Virtual Instrument Engineering Workbench (LabVIEW) is a graphical programming language and development interface developed by National Instruments. It deals with measurement and control system design, prototyping, and deployment with extensive application in the fields of engineering and scientific research. LabVIEW is a visual programming environment in which users can construct virtual instruments (VIs) by connecting graphical icons that represent different functions and operations. As no textual code is required, engineers and scientists who lack programming skills can also use LabVIEW software due to its visual method. LabVIEW's graphical dataflow paradigm is its central idea. LabVIEW uses wires between nodes to represent the transmission of data and the execution of commands throughout the program. The various features of nodes are sensor data collection, computation, output to a user interface, hardware device control, and system communication. It is simple to interact with multiple instruments and sensors because of LabVIEW's wide library with pre-built functions, tools, and drivers for diverse hardware devices. As a result, LabVIEW is widely used in fields like as data acquisition, test and measurement, and automation. In addition to its many other useful features, LabVIEW's user interface design toolset lets you craft dynamic and aesthetically pleasing user interfaces for your digital instruments. A variety of controls and visual representations of data in real time can be included into these front panels. LabVIEW also allows users to incorporate existing code or improve LabVIEW's capabilities by accessing additional libraries and tools thanks to its support for integration with other programming languages like C/C++, .NET, and Python. Apart of this, LabVIEW has developed its base in many different sectors like Automation in industry, robotics, control systems, embedded systems, scientific experimentation, and academic research. Its widespread adoption in the fields of engineering, science, and education can be attributed to the software's adaptability, user-friendliness, and hardware compatibility.

In this research work also, a graphical interface has been developed using LabVIEW software to record vibration signals. A file with extension .vi has been created where after selecting integrated data acquisition system, recording can be initiated. For

recording purposes, a start and stop button has been provided on the interface along with timer. For continuous monitoring, live plotting of two waveform graphs have been incorporated also where live feed of amplitude vs time and amplitude vs frequency can be seen. The whole exercise has been done by developing block diagram of the whole system. This block diagram has been drawn by covering up all the elements like ball bearing, data acquisition system (DAQ) physical channel, DAQ assistant data, spectral measurements, waveform graph, file path control, record button, stop button and reset button along with setting up of their connections in the software. The front panel of the interface is shown in the Figure 34.

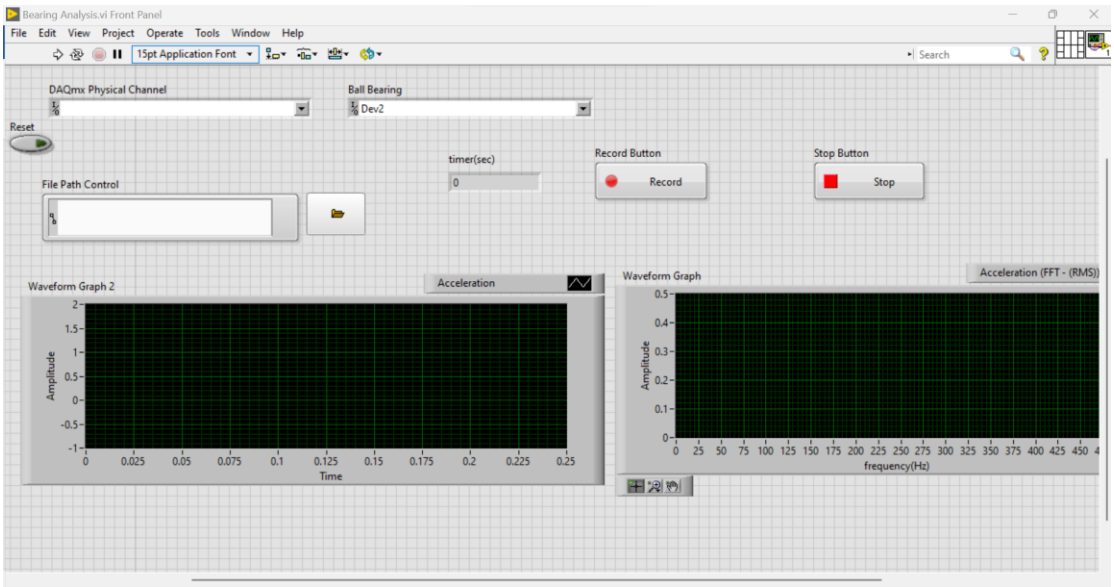

Figure 34: LabVIEW Interface to record vibration signals

Using front panel interface of LabVIEW software, it becomes feasible to record vibration signal with the computer system. For this, accelerometer has been mounted on top of the bearing using petro wax. At low temperatures, petrol wax is an outstanding adhesive. Like cyanoacrylate, the uniform frequency response of petro-wax increases as temperature decreases. It should be noted that the maximal bonding strength of petro-wax when applied to smooth steel surfaces is approximately 15 psi. After acquiring signal from top of the bearing casing using accelerometer, it is transferred through DAQ system to the computer. Further, the signal is saved in the hard drive using DAQ integrated LabVIEW software installed in the computer system. The signal file was saved in .tdms format which was converted into .xlsx format by installing converter

extension file from official website of LabVIEW software. These converted files were imported into MATLAB software, where it was firstly converted into .mat file extension to analyze the same using signal processing toolbox of the software or by using relevant code-based signal processing technique.

5.7 Introduction to Signal Processing Toolbox of MATLAB

The Signal Processing Toolbox offers capabilities and uses for managing, examining, preprocessing, and extracting characteristics from signals, whether they are uniformly sampled or nonuniformly sampled. It provides comprehensive functions and tools for signal analysis, processing, and synthesis within the MATLAB environment. It has many features used in signal processing, including as filtering, spectral analysis, waveform synthesis, and signal visualization. The toolbox contains instruments for filter design and analysis, resampling, smoothing, detrending, and estimation of the power spectrum. The Signal Analyzer application can be used to simultaneously visualize and process signals in the time, frequency, and time-frequency domains. The various features of the toolbox are discussed further:

- **Filtration**: Filter types including FIR (Finite Impulse Response) filters, IIR (Infinite Impulse Response) filters, and multi-rate filters are all available as part of the toolbox's collection of functions. Filters can be designed and implemented to perform operations such as suppressing unwanted noise, amplifying weak signals, and processing data based on their frequencies.
- **Frequency Analysis:** Functions for calculating and inspecting signal frequencies are included in the toolkit. Spectral analysis activities like as performing the Fourier transform, estimating power spectral density, creating spectrograms, and using windowing techniques are all within the reach using this approach.
- **Signal Processing algorithms:** The toolbox contains an assortment of sophisticated algorithms for signal processing, such as adaptive filters, wavelet transforms, and cepstral analysis. These algorithms can be used for a variety of purposes, including reverberation cancellation, speech recognition, and audio compression.

- **Waveform generation:** The toolbox includes functions for generating sine waves, square waves, sawtooth waves, and pulse trains, among other waveforms. These functions are useful for producing test signals, simulating communications systems, and synthesizing audio signals, among other applications.
- **Signal Visualization:** To better view and analyze signals, MATLAB's Signal Processing Toolbox provides several charting and visualization capabilities. To better understand the signals, it can be plotted in time domain or frequency domain, make spectrograms, and construct various types of graphs.

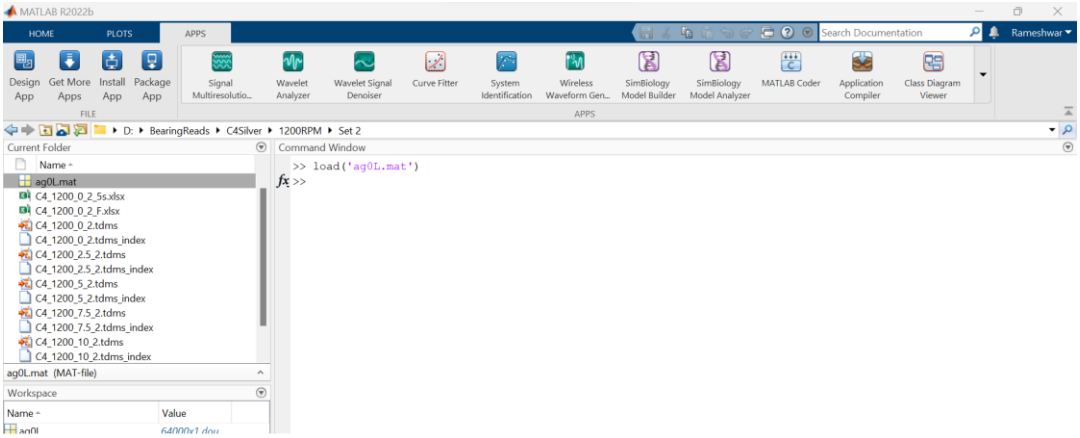

Figure 35: Interface for the signal processing in MATLAB

In this study, each coated ball bearing was made to run at five different speeds i.e., 300, 600, 900, 1200 and 1500 rpm and its vibration signals were captured for ten seconds using timer feature in front panel display screen of LabVIEW software. The sampling rate for signal capturing was kept at the rate of 12800 data points per second. The captured ten second signal was later trimmed to a five second signal hence generating 64000 data points for each signal, which is relevant enough for the application of suitable signal processing technique. After acquiring the signals at different speeds, the bearing has been dismantled from casing and was replaced with next coated bearing. The same procedure for all coated bearings were repeated for five times then average of the vibration signals collected in five attempts has been considered for the further analysis. It is to be noted that, in all five iterations, the order of installing bearing in the mounting were maintained. For instance, if while taking readings for the first set, the

order of installing bearing were Nickel, Copper, Zinc Phosphate, Silver, and Black Oxide then in second set also, same order of installation of bearings has been followed and so on. While recordings the signals, care has been taken to maintain the same working conditions to the best possible extent. Moreover, all signals were recorded only after stabilization of the system i.e., after attaining required shaft speed using VFD, the system was allowed to run idle for few minutes before start recording the signal. All signals were saved in hard drive of the computer in different folders made according to the specified coatings at different running speeds. Depending on the nature of the signal and required information to be extracted, suitable signal processing techniques can be applied onto these signals using signal processing toolbox or code-based algorithms of MATLAB software. The R2022b release version of the software has been used in this research work.

After acquiring vibration signals of specified coated bearings at different speeds, it is required to extract relevant information from these signals with the help of suitable signal processing techniques. Condition monitoring and fault diagnostics rely heavily on information achieved after processing vibration signal of bearings [84,89]. These signals are often processed and analyzed using a variety of methods. The techniques for processing vibration signals can be broadly categorized as follows:

- **Time-Domain Techniques**: The time domain techniques have been sub categorized into two versions as time waveform analysis and envelope analysis. Time waveform analysis is the process of analyzing the unprocessed vibration signal in the time domain to identify key characteristics. such as peak amplitudes, impulses, and transient patterns. Whereas, in envelope analysis with the usage of techniques like demodulation and high-pass filtering, the amplitude variations of the vibration signal are extracted. This assists in identifying bearing defect frequencies and tracking their progression.
- **Frequency Domain Techniques:** The frequency domain techniques have been sub categorized into three types as: Fast Fourier transform (FFT), Power spectral density (PSD) and Cepstrum analysis.

a) Fast Fourier transform (FFT): In order to locate specific frequencies associated with bearing defects, it is necessary to transform the vibration signal from the time domain to the spectral domain.

b) Power spectral density (PSD): The main frequencies and their harmonics can be more accurately represented by estimating the power distribution across all audible frequencies.

c) Cepstrum analysis: To isolate overlapping frequency components and spot patterns related to bearing faults, a logarithmic spectrum analysis is performed.

- **Statistical Analysis**: Statistical analysis is the procedure to analyze data gathered from vibrating systems and can be interpreted with the use of statistical methods and techniques. The state, health, and behavior of the vibrating system, including bearings, machinery, or structures, can be predicted by analyzing the statistical features of vibration signals. The method of statistical analysis remains to be a preferred choice of researchers since decades to be implemented on vibration signal for the variety of tasks like fault detection and analysis [84-96], Trend analysis [97-100], Condition Assessment [101-106], Identification of fault related frequencies [94,107-111], Statistical pattern recognition [112-116], Prognostics [117-122], Remaining Useful Life (RUL) estimation [123-129], Decision support [130-134] and Data-driven Insights [135-141].

  Therefore, in this work also, attempt has been made to compare the level of properties for the bearing coating based on the statistical analysis of the vibration signal. Further, details about the same has been discussed in the next chapter.

6. Results and Discussion

As previously stated, this research work focuses on comparing the diverse properties of the bearing coating through statistical analysis of vibration signals. The aim is to establish a correlation between variations in specific properties and appropriate statistical parameters. The objective is to identify a statistically significant parameter that exhibits a similar trend of increase or decrease as the level of the property varies with changes in the coating. For example, if the coatings are arranged in ascending order based on their surface roughness, the goal is to determine the corresponding increase in the value of a specific statistical parameter as the roughness increases. However, if multiple statistical parameters exhibit an increasing trend, a sensitivity analysis has been conducted to identify the most suitable parameter that responds effectively to variations in the surface roughness of the coating. While it is possible to directly perform statistical analysis on the acquired vibration signal, preprocessing the signal can yield improved results. In this study, first of all, statistical analysis has been directly conducted on the obtained vibration signals. but not much encouraging results were obtained. Therefore, a decomposition technique has also been employed to separate the signal into distinct spectral components, aligning with the nature of the research. It enables a more accurate identification of the frequency band that may correlates with the variation in the specific material property under investigation. Once the relevant frequency band is identified, further statistical analysis is conducted to obtain refined information regarding the statistical parameter that exhibits a response to the property variation. Further, decomposition technique is elaborated upon in detail, alongside a comprehensive description of the various statistical parameters utilized in this study.

6.1 Signal Decomposition

Signal processing plays a crucial role in facilitating vibration-based Structural Health Monitoring (SHM), which encompasses tasks such as damage detection and more complex analyses. It is widely acknowledged that signal processing serves as the fundamental enabling technology for SHM, providing the necessary tools and techniques to extract valuable information from vibration signals and support various

aspects of structural health assessment and monitoring. Nevertheless, the exploration of real-world vibration measurements presents an intriguing challenge. In order to enhance our comprehension of the system's dynamic characteristics, it is essential to effectively decompose a multi-degree-of-freedom system into its individual components. However, nonlinearities, whether associated with damage or not, can introduce noise-like distortions in the vibrational response of the target structure. These distortions can result in nonstationary behavior, necessitating a time-frequency analysis approach. In such cases, adaptive mode decomposition methods considered to be best strategy to effectively address these challenges. In this study, a careful selection process has been undertaken to identify three widely recognized signal decomposition algorithms for in-depth analysis. The chosen approaches: Empirical Mode Decomposition (EMD), Wavelet Packet Transform (WPT) and Variational Mode Decomposition (VMD) have been regarded as representative techniques due to their extensive utilization and positive reception within the research community [146-155]. The research comprehensively examines and compares the key characteristics of these data-adaptive methods, along with their respective advantages and disadvantages. Following the analysis of vibration signals, the selection of the most suitable decomposition technique has been made based on the obtained response.

Examining actual signals from vibrating structures presents challenges primarily due to measurement noise, non-stationarity, and distortions resembling noise induced by structural nonlinearities [142]. Nonetheless, the dynamic response of a target system can unveil its mechanical characteristics, particularly its stiffness and/or mass. This process is commonly known as System Identification (SI/NLSI), which involves the process of determining the linear or nonlinear characteristics of a system. In the presence of consistent operational, environmental, and boundary conditions (i.e., without confounding factors), alterations in these characteristics can be directly associated with the advancement of damage [143]. Through a comprehensive comparison between the present state of the system and the predefined "normal" baseline model, effective implementation of vibration-based damage detection and Structural Health Monitoring (SHM) becomes feasible. The primary objective of any decomposition technique is to separate and extract a variation from normal i.e., Defect

Signal Mode (DSM) from the wide-band recordings of the structural response. These DSMs can be utilized either individually or, more commonly, further post-processed to extract one or more Damage-Sensitive Features (DSFs) from each mode. Subsequently, surrogate models can be established using the DSMs and/or the DSFs obtained during normal operational conditions. To ensure robustness and minimize false alarms, it is advisable to incorporate data recorded across diverse environmental and operational conditions. That is why, five different sets have been made while recording vibration signals then mean of these signals is taken before further processing [142]. Finally, damage-related or property variation anomalies can be uncovered using standard outlier identification statistical approaches. The fundamental concept of decomposing a signal is to effectively fragment a complex signal into simple and identical parts in a rapid and efficient manner. These components, also known as modes, should ideally exhibit a high degree of independence from one another, resembling the eigenmodes obtained from the modal analysis of a time-independent, linear system. Additionally, it is desirable for these components to possess certain sparsity properties, such as being limited in bandwidth within the frequency domain and exhibiting compactness around a center frequency. It is crucial that the integration of all these elements enables the reconstruction of the original signal with minimal information loss, ideally obtaining a minimum least-square error. While the generated modes share similarities with linear normal modes (LNMs), it is important to note that they are not necessarily identical, and both logics should not be conflated [144].

Subsequently, these "modes" can be utilized in various ways. For instance, it is possible to discard very low- or high-frequency content that is not linked with physical characteristics of the system under investigation. This process is commonly known as denoising and baseline drift removal. Both techniques are commonly employed in Structural Health Monitoring (SHM). However, it is crucial to exercise caution when removing nonstationary components, as it may result in the loss of important data information. This consideration is particularly significant in civil engineering applications where the input excitation is influenced by ground motion [145]. Additional modes that are not relevant to damage detection or influenced by external factors such as temperature, seasonal variations, or vibrations from operating

machinery, pedestrians, or vehicles can also be eliminated. Nonstationary components can be disregarded to emphasize time-independent mechanisms or features [146]. Ultimately, certain modes may exhibit higher sensitivity to damage compared to others. Consequently, it becomes easier to detect small changes, such as those caused by early-stage crack development, in an individual component rather than across the entire signal. The presence of other damage-insensitive information can mask these subtle variations, making it more challenging to identify them.

6.2 Adaptive Mode Decomposition Methods

In recent years, numerous algorithms have been proposed to address the objectives mentioned earlier. Nevertheless, there has been a lack of systematic analysis of these approaches from the perspective of Structural Health Monitoring (SHM). Many review papers simply compile uses documented in the previous research, presenting the results and outcomes of several authors. Some review articles conduct restricted testing by executing algorithms on limited signals, often synthetic, with minimum additional remarks. The objective of the given straight-forward comparison is to evaluate the accuracy and efficiency of these procedures to extract Damage-Sensitive Features (DSFs) and subsequent training of Machine Learning models. Among the various suggestions documented in scientific literature, the most renowned methods comprise Empirical Mode Decomposition (EMD) [147], Wavelet Packet Transform (WPT) [148] and Variational Mode Decomposition (VMD) [49]. Each of these approaches is predominantly based on empirical observations or incorporates theoretical principles that justify their operational methodology. Their mutual aim is to facilitate data-adaptive time-frequency analysis for nonstationary time histories (THs) of both linear and nonlinear systems. These three algorithms have been carefully chosen that have gained significant popularity across various engineering domains and exhibit substantial differences from one another. Each of these algorithms has demonstrated successful applications in the realms of fault detection and damage assessment [150, 151]. In this study, the three methods mentioned above are subjected to a quantitative comparison. It is important to note that although the reviewed algorithms are not restricted to time series or one-dimensional single-channel data analysis, given study

will focus solely on this specific case, even though respective bivariate or multivariate extensions may exist [153, 154].

6.3 Theoretical Background of Signal Processing Techniques

This section focuses on the theoretical aspects of the three decomposition techniques under consideration. As mentioned earlier, all of these methods involve splitting the given signal into multiple parts. This decomposition can be achieved directly in the time domain, as seen in the case of the Empirical Mode Decomposition (EMD) and related methods, or in the frequency domain, such as with the Variational Mode Decomposition (VMD). Moreover, decomposition can also take place in the time-frequency (or time-scale) domain. The fundamental principle behind frequency- and time-frequency-based decomposition methods lies in the recognition that the majority of real-world signals demonstrate compact and band-limited Fourier spectra. These techniques inherently presuppose that the individual components of the signal exhibit narrow-band characteristics and typically possess clearly defined spectrum supports. What distinguishes the discussed methodologies from the conventional Fourier transform (FT) is their ability to analyze time-varying signals, often referred to as nonstationary signals. These techniques are characterized by their analytical or empirical definitions, meaning that it operates based on algorithms rather than having a precise mathematical formulation. This feature grants them a certain level of adaptability to the data being analyzed [155]. The subsequent subsections provide a comprehensive description of the three methodologies. The discussion commences with the Empirical Mode Decomposition (EMD) and its subsequent variants, followed by the WPT, and finally the VMD.

6.3.1 Empirical Mode Decomposition

Empirical Mode Decomposition (EMD) is a multi-resolution method to split a signal into meaningful components based on the data itself. This technique is capable of handling non-linear and non-stationary signals by extracting components with varying

resolutions. Empirical mode decomposition finds its usefulness in various domains such as bearing fault detection, analysis of biomedical data, power signal analysis, and examination of seismic signals [156-158]

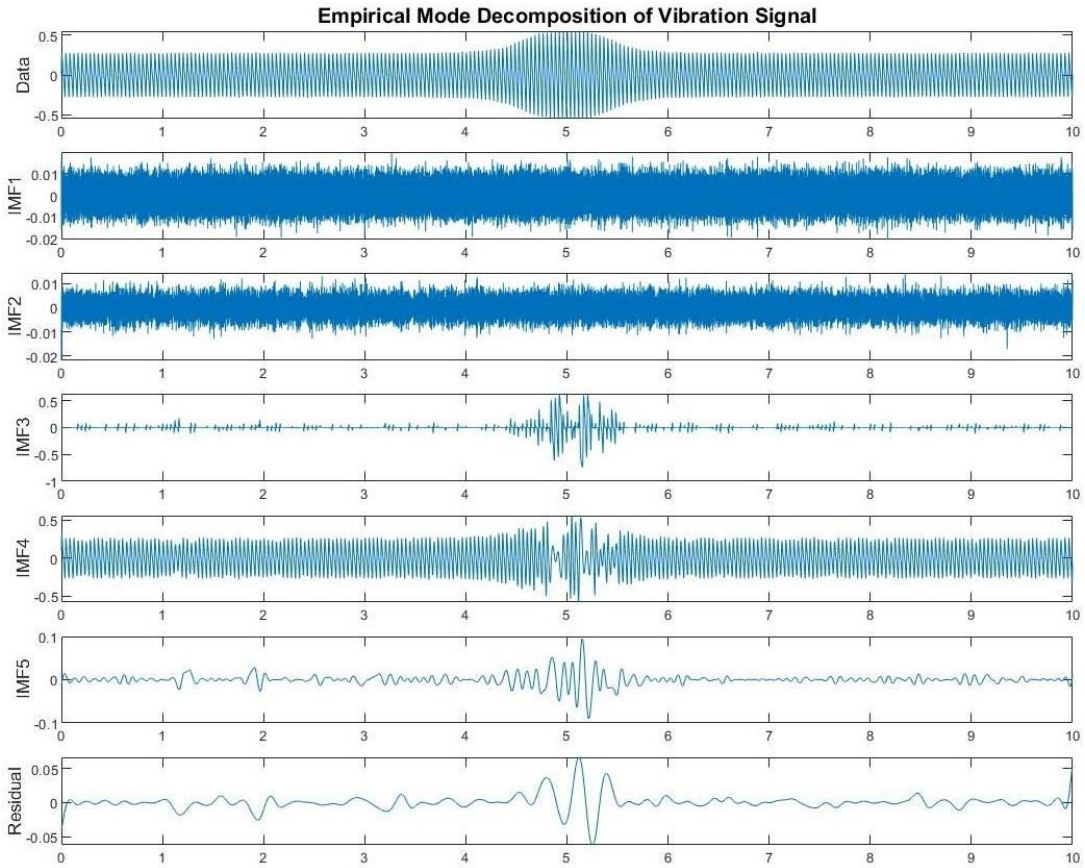

Figure 36: Empirical mode decomposition applied to a vibration data in MATLAB [158]

Since its inception in 1998 [147], the Empirical Mode Decomposition (EMD) has been extensively investigated and implemented in a variety of fields. For structural purposes, it has been utilized for System Identification [158,159], as well as for Operational Modal Analysis [160] by approximating the eigenmodes of bridges. In addition to the SHM of steel frame structures [161], it has been utilized in a variety of other applications. The technique is notably valued for rotating machinery condition monitoring [162-164].

Empirical Mode Decomposition (EMD) enables time-frequency analysis while preserving the signal's time domain representation. The resulting components, known

as intrinsic mode functions (IMFs), maintain the same time scale as the original signal, facilitating their analysis. Unlike conventional multiresolution analysis techniques like wavelet analysis, EMD recursively separates different resolutions directly from the data itself, without relying on predefined functions or filters. Another approach to understanding EMD is to consider a signal as a combination of a rapid oscillation overlaid on a slower variation. By extracting the rapid oscillation component, in the EMD algorithm, the slower component that remains is considered as the new signal. and repeats the process, considering it as a rapid oscillation superimposed on a slower variation. This iterative procedure continues until reaching a predefined stopping criterion. By employing this methodology, EMD decomposes the signal into its constituent IMFs, providing a localized and interpretable representation of its intrinsic mode functions [158]. To be classified as an Intrinsic Mode Function (IMF), a function needs to fulfill two specific criteria:

a) The count of local maxima and minima should either be equal or differ by at most one.

b) The local mean, calculated as the average of the upper and lower envelopes, must be zero.

In essence, an IMF must possess a balanced number of extrema and zero crossings while maintaining a symmetrical distribution of energy around its mean value. These conditions ensure that IMFs capture the intrinsic mode functions of a signal without introducing any spurious components or biases. Therefore, the Intrinsic Mode Functions (IMFs) can be regarded as zero-mean components characterized by amplitude modulation and frequency modulation. Consequently, the original signal can be reconstructed by simply taking sum of all the IMFs in the time domain [147]. It is important to note that IMFs lack a specific analytical formulation [165]. This is due to the fact that Empirical Mode Decomposition (EMD) is an algorithm based on empirical rules, as the name suggests, without a well-defined theoretical foundation, unlike, for example, the Fourier Transform. The EMD decomposition process, also known as the "sifting process" [166]. In Figure 28, a visual representation illustrates the steps involved in the process. At each step, the residual signal, referred to as r_p(t) (where p=0 and $r_{p=0}(t)=x(t)$), is sifted. The mean of the upper and lower envelopes is obtained,

resulting in $m_p(t)$. The difference between $r_p(t)$ and $m_p(t)$ is then further iterated, denoted by the additional counter *i*, until it satisfies the two defining conditions of an IMF. At this stage, $x_p(t)$ represents the *p*-th IMF, and a new residual is computed. The algorithm continues until the *P*-th residual, $r_P(t)$, becomes a monotone function or a function with less than two local minimum or maximum points, indicating the termination of the process.

One significant technical drawback of the basic definition of Empirical Mode Decomposition (EMD) is the presence of a phenomenon called "mode-mixing" when applied to signals contaminated with measurement noise or noise-like nonlinear disturbances. This issue arises when the EMD method excessively decomposes a signal, resulting in the extraction of more Intrinsic Mode Functions (IMFs) than the original signal's actual oscillatory modes. The occurrence of mode-mixing can be attributed to the completely data-driven nature of EMD. When noise is introduced, it introduces additional "artificial" maximum and minimum points that are detected and interpolated by the algorithm. Consequently, even a single-component signal like a simple sinusoid can be fragmented into multiple sub-signals when influenced by noise [167]. The heightened susceptibility to noise restricts the dependability of a signal monitoring scheme based on Empirical Mode Decomposition (EMD). Therefore, WPT and VMD methods of decomposition are also applied on same dataset so as to compare and obtain best results.

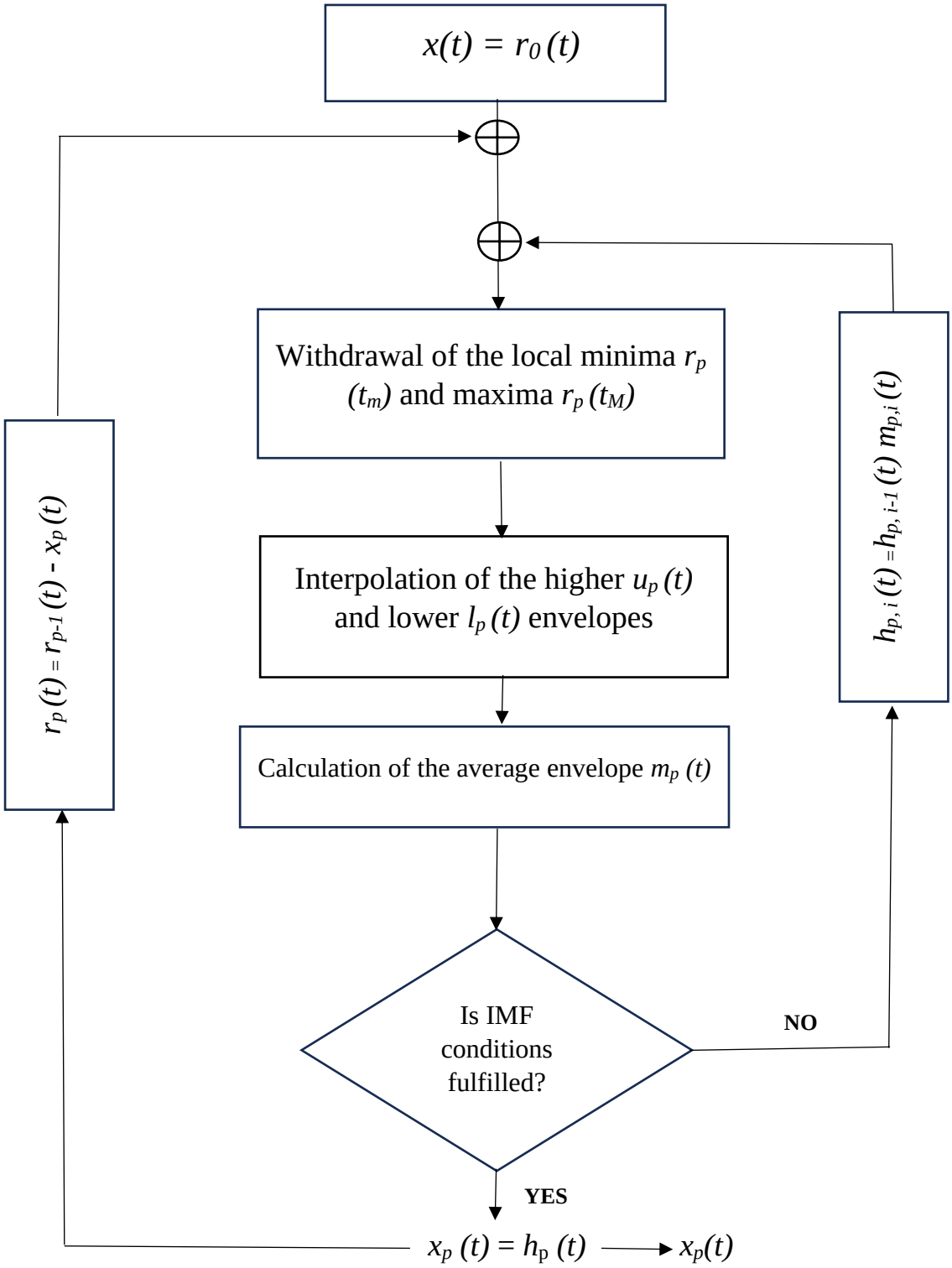

Figure 37: EMD algorithm flowchart

6.3.2 Wavelet Packet Transform

When it comes to breaking down signals or data into their component frequencies, the Wavelet Packet Transform (WPT) is an extremely useful mathematical technique. It is an expansion of the Wavelet Transform that allows for greater versatility in signal representation and processing. The WPT uses wavelet functions, including the Wavelet Transform, which are small, localized functions that are ideal for capturing localized aspects of signals. However, the wavelet transform decomposes signals into a collection of approximation and detail coefficients, which appears to be a treelike structure, therefore called as Wavelet Packet Tree. WPT is one of the instruments for time frequency analysis. It is a transformation that places the signal in a domain containing both time and frequency data [168]. This allows for simultaneous frequency and time examination of the signal. Making FFT analyses in small time windows is the simplest technique to perform time frequency analysis. This has the downside that a long window is needed to identify low frequency components and a short window is needed to identify rapid changes in the signal. When it comes to handling transitory signals, the wavelet packet transform (WPT) provides a great lot of flexibility [148]. Wavelet packets are a specific type of linear combination formed by combining wavelets. These combinations create bases that preserve important properties of their parent wavelets, including orthogonality, smoothness, and localization. The coefficients for these combinations are determined through a recursive algorithm, which calculates each wavelet packet coefficient. As a result of this computational process, expansions using wavelet packet bases exhibit low computational complexity. Each level of the Discrete wavelet transform (DWT) is computed by applying high and low pass filters to the preceding approximation coefficients. The WPD, on the other hand, separates out the detail and approximation coefficients. In contrast to the DWT, which generates (n+1) sets of coefficients (or nodes) for n levels of decomposition, the Wavelet packet decomposition (WPD) generates 2^n sets. However, the total number of coefficients remains constant due to the down sampling process, thus eliminating redundancy [148]. Moreover, features have been deduced from time domain signals using WPT algorithms. The time signal is mined for information that can then be used in the feature extraction process [169]. The wavelet packet transform offers several significant

advantages over the discrete wavelet transform. Wavelet packet functions form a diverse set of fundamental building block functions. While still exhibiting temporal localization, wavelet packet functions provide greater flexibility compared to wavelets in representing various signal types. It is particularly effective at capturing signals with oscillatory or periodic behavior. Wavelet packets are naturally organized into collections, with each collection serving as an orthogonal basis for $L^2(R)$. This simple yet powerful extension of wavelets and multiresolution analysis (MRA) enables the basis to adapt more flexibly to a signal's frequency content. Furthermore, developing a fast wavelet packet transform is relatively straightforward. The strength of the wavelet packet transform lies in its increased freedom to choose the most appropriate basis function for representing a given function. Additionally, it can be computed efficiently, requiring only $O(M \log M)$ time, where M represents the number of data points. This efficiency is particularly advantageous in real-time applications. Furthermore, wavelet packets exhibit compact support both in the time and frequency domains, adapting their support locally to the signal. This adaptability is crucial for handling time-varying signals. With wavelet packets, finer resolution of the signal is gained with wider range of options for decomposition. These capabilities provide enhanced flexibility and accuracy in signal analysis and processing.

The wavelet packet method serves as an extension of wavelet decomposition, offering a broader array of options for signal analysis and enabling optimal matching of the analysis to the signal. It transforms a signal from the time domain to the frequency domain level by level. This transformation is achieved through a recursive process of filter-decimation operations, which decreases time resolution while enhancing frequency resolution. Unlike wavelet decomposition, which only divides the low-frequency subband, the wavelet packet method partitions both the low and high-frequency subbands, resulting in uniformly wide frequency bands.

During wavelet analysis, a signal is split into an approximation coefficient and a detail coefficient. The approximation coefficient is further subdivided into second-level approximation and detail coefficients, and this process continues iteratively. In WPT, details and approximations can be separated, providing multiple encoding options for the signal. Unlike wavelet transformation, which employs only two basis functions at

the deepest level, the wavelet packet method allows for more than one basis function at a given scale by iterating both low and high-pass filter outputs.

The wavelet packet method offers various bases constructed from collections of wavelet sequences, with the wavelet basis resulting from iterating only the low-pass filter, and the full tree basis generated by iterating both low and high-pass filters. At the highest level of the wavelet packet decomposition tree lies the signal's temporal representation, while traversing each level of the tree involves a trade-off in between time and frequency resolution. Ultimately, the lowest tier of a fully decomposed tree illustrates the signal's frequency representation.

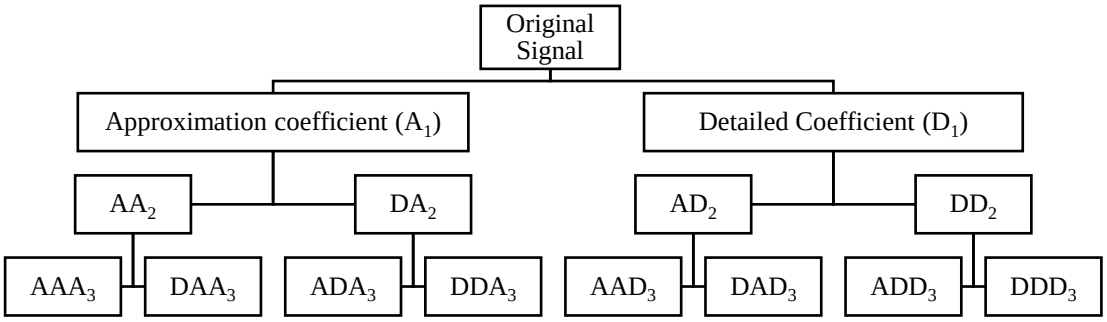

Figure 38: Wavelet packet decomposed signal up to level 3

In wavelet packet analysis, the optimal decomposition of a given signal is determined using an entropy-based criterion. This entails examining each node of the decomposition tree and quantifying the information to be obtained from each split. There are several different families of wavelets. Haar, Daubechies, Symlets, Coiflets, and biorthogonal wavelets are some of the most well-known wavelet families.

Before decomposing the signals using WPT, choosing an appropriate wavelet based on the signal's characteristics is crucial. The choice of wavelet can be made based on several significant criteria as discussed next after literature review. There are numerous varieties of mother wavelet that can be utilized in wavelet analysis. If distinct mother wavelets are used to scrutinize the given signal, different results will be produced. In general, mother wavelets are distinguished by characteristics including orthogonality, compact support, symmetry, and vanishing moment. In selecting a mother wavelet, the

properties of the mother wavelet are considered in light of previous research. However, there is frequently more than one mother wavelet with the same properties. In order to circumvent this, the resemblance between the signal and mother wavelet is taken into account when selecting a mother wavelet. Based on quantitative and qualitative approaches, researchers have devised numerous methods for determining the similarity between a signal and its mother wavelet. There is currently no standard or general method for choosing the mother wavelet.

6.3.2.1 Review on the selection of mother wavelet using qualitative approach

Choosing the appropriate mother wavelet for analysis relies on considering either the characteristics of the mother wavelet itself or the resemblance between the signal and the mother wavelet. In this specific case, choosing the optimal mother wavelet for separating surface profiles into their multi-scale representations is based on the symmetry properties of the wavelet. It was determined that the biorthogonal 6.8 wavelet best fulfilled the desired criteria [170]. In consideration of regularity, vanishing moment, and degree of shift variance, biorthogonal wavelets were chosen for characterizing texture [171]. The Daubechies4 (db4), coiflet, and b-spline were all found to be equally effective by Safavian et al. [172] in detecting transients in power systems. Biomedical engineers Wang et al. [173] separated burst and tonic components in compound surface electromyogram (EMG) signals collected from patients with dystonia by considering the features of compact support, vanishing moment, and orthogonality. After considering orthogonality, symmetry, regularity, explicit expression, and compact support, Ahuja et al. [174] in the field of image processing determined that B-spline wavelets are the optimal choice as the mother wavelet for enhancing image sequence super resolution.

Another qualitative criterion for selecting a mother wavelet was the degree to which it resembled the input signal. Picking the best mother wavelet typically involves using shape matching via visual inspection. Timing of multiunit bursts in surface electromyograms (EMG) from single trials was studied by Martha Flanders [175], who looked into the effectiveness of various mother wavelet shapes. To best represent the EMG signal, the db2 wavelet was selected as the mother wavelet. Faisal et al. [176]

noted that the choice of a mother wavelet that closely fits the signal is crucial in the identification of true three phase voltage sags. Finally, the Gauss wavelet was found to be the optimal mother wavelet for spotting voltage drops in three-phase systems. The gauss mother wavelets are visually most similar to the recorded acoustic emission leakage signal-signatures, as discovered by Ahadi et al. [177]. Also, it was noted that leak detection systems can make advantage of the spectrograms generated by well selected mother wavelets. Since morlet wavelet is analogous to mechanical impulse signal, Tang et al. [178] used it to de-noise vibration signals for defect diagnostics of wind turbines. It was also noted that the chosen mother wavelet should possess characteristics similar to the mechanical impulse response. This similarity helps amplify the amplitude of the resulting wavelet coefficients associated with fault impulses, thereby enhancing the fault identification process. However, visually correlating the signal's structure with that of the mother wavelet found to be challenging.

6.3.2.2 Review on the selection of mother wavelet using quantitative approach

Researchers have also introduced the introduction of quantitative approaches to the justification of the similarities between a signal and its mother wavelet. Saito et al. [178] suggested the metric of minimum description length (MDL) as a criterion for choosing the best mother wavelet (MW) for noise cancellation and signal compression. According to the Minimum Description Length (MDL) concept, the 'best' model is the one that describes the data and the model with the fewest words. In order to choose the best MW for power disturbance data compression, Hamid et al. [180] used MDL as a guideline. When compared to other mother wavelets using the MDL criterion, symlet 7 appeared to be the most effective at suppressing power disturbance signals. Khan et al. [181], who analyzed the safety of three-phase, induction permanent-magnet motors, also used MDL criteria to determine which mother wavelet was best suited to their problem. This led to db3 being chosen as the "MW" for WPT. A self-tuning multiresolution proportional integral derivative controller was designed for the interior permanent magnet synchronous motor drive system, employing the same criteria for selecting the mother wavelet [182]. The db4 wavelet was selected as the mother wavelet for denoising UHF signals in a study on partial discharge (PD) detection, primarily due

to its highest cross-correlation coefficient with the UHF signal among the considered options [183]. To determine the optimal mother wavelet for PD signal extraction, W. Li [184] used the maximum cross correlation coefficient (MCCC) criterion. Denoising an electrocardiogram signal also used the MCCC criterion. Singh et al. [185] investigated the denoising of the electrocardiogram signal with db8, after using the highest cross correlation coefficient as a criterion for its selection. Zhang et al. [186] provided two criteria' for choosing the best mother wavelet for image denoising. Information extraction (IC) criterion and distribution error (DE) criterion were the first and second criteria, respectively. As the congruence between the selected mother wavelet and the form of the signal under study increases, the ratio of the first to the second criterion should decrease. Using the aforementioned criterion, the bior1.3 wavelet was discovered to be capable of providing the greatest performance for image denoising. In order to choose the best mother wavelet for automatic ultrasound non-destructive foreign body (FB) detection and categorization, Tsui et. al [187] presented relative entropy as the evaluating parameter to find out resemblance between wavelet coefficients. According to their research, biorthogonal 3.1 is the best mother wavelet for classifying FB shapes, whereas haar (or symlet 1 or reverse biorthogonal 1.1) and reverse biorthogonal 3.9 are the best for classifying FB materials that are spherical and rectangular, respectively. R. Yan [188] introduced the energy-to-Shannon entropy ratio (ESER) criterion and the MinMax information criterion as techniques for selecting the optimal mother wavelet for detecting bearing faults. The ESER criterion aims to maximize the energy while minimizing the Shannon entropy of the associated wavelet coefficients. On the other hand, the MinMax information criterion takes into account several criteria, including the minimum joint entropy, minimum conditional entropy, minimum relative entropy, maximum mutual information, and maximum correlation coefficient. By employing the ESER criterion and the MinMax information criterion, the reverse biorthogonal 5.5 wavelet was chosen as the MW for discrete wavelet transform analysis in this study. On the contrary, the authors opted for the utilization of the complex Morlet wavelet in their analysis through continuous wavelet transform. J. Rafiee et al. [189] put forth a method to select the most appropriate MW for gear signals by evaluating the variances of continuous wavelet coefficients. They found that a higher variance indicated a better ability to accurately classify failures. To simplify the

process, they calculated the sum of the five elements with the highest values from various faults, referred to as "SUMVAR." The MW with the highest SUMVAR value was chosen as the most identical MW for gear signals. Out of the 324 MWs, the db44 wavelet was chosen for analysis as it displayed the closest similarity to gear signals. The same selection criterion for the mother wavelet was also applied in diagnosing bearing and gear faults. The investigation revealed that while db44 exhibited the highest similarity as a MW function for both bearing and gear signals, it was not suitable for all wavelet-based processing [190]. In another study by J. Rafiee et al. [191], the selection of the MW, for gear fault diagnosis was proposed using a genetic algorithm. The genetic algorithm methodology was utilized to explore the optimal Daubechies order, signal decomposition level, and the quantity of neurons in the hidden layer. The findings revealed that db11, level 4, and 14 neurons were identified as the optimal values for the Daubechies order, decomposition level, and hidden layer node count, respectively. To determine the optimal wavelet family and MW for studying power system steady-state harmonic distorted waveforms with minimal spectral leakage, Morsi et al. [192] suggested a novel criterion for selecting the mother wavelet, relying on the energy of the wavelet coefficients at every level. Accuracy improves with each wavelet order, and the db MW family was shown to be the best fit for low distorted levels. Results are more reliable when using a low-order MW, and the coiflet family is optimal for high-distortion situations. Cheng et al. [193] suggested a novel method for automatically picking the mother wavelet and parameters, a significant factor to employ wavelet algorithms, in the context of contrast enhancement research. A total of 66 MWs were chosen in advance using the suggested method, with each one being evaluated for its vanishing moment, shift variance, and regularity. An ideal MW was chosen by minimizing a measurement of the wavelet's horizontal and vertical edges. Phinyomark et al. [194] proposed a innovative, noise-resistant mother wavelet selection technique for EMG feature extraction in the field of biomedicine. Wavelet coefficients and reconstructed signals' mean squared errors were compared to find the best mother wavelet. J. Rafiee et al. presented [195] evaluation metric (EM) for the MW selection process concerning biomedical signals. The continuous wavelet coefficient absolute value was determined at various resolutions. This value was then estimated across all scales for various biological signals. For convenience, an average across all signal types

were calculated and labeled it "evaluation criterion" (EC). The db44 was chosen for the evaluation of EMG, EEG, and VPA signals using continuous wavelet transform. The research suggested that exclusively depending on the resemblance between signals and mother wavelet functions might not always be appropriate for signal processing with wavelet transform and other wavelet-based techniques. Instead, it was proposed that methods relying on the similarity between signals and mother functions were better suited for wavelet-based processing techniques. Kankar et al. [196] also employed the energy to Shannon entropy ratio criterion to detect bearing faults. Additionally, an alternative criterion was proposed for selecting the mother wavelet based on information regarding relative energy within associated frequency bands. Through the application of continuous wavelet transform on the bearing signals, the coefficients were computed with the help of three real mother wavelets and three complex mother wavelets. The choice of the Meyer wavelet was guided by the ESER criterion, whereas the complex Morlet wavelet was selected based on the maximum relative wavelet energy. Findings indicated that the mother wavelet chosen via the ESER criterion notably enhanced classification accuracy. After analyzing the above-mentioned case studies, the selection of wavelets for this research has been determined by considering the ratio of maximum relative energy to the Shannon entropy criterion. This approach has exhibited significant outcomes in many similar cases [197-200], which aligns well with the objectives of this research. Therefore, for each coated bearing signal, the value of maximum energy has been calculated using 30 wavelets followed by calculation of minimum Shannon entropy. Afterwards, ratio of these two terms were taken out for the purpose of selecting wavelet based on maximum energy to minimum Shannon entropy criteria. Out of 30 wavelets, Bior 2.6 wavelet has shown promising results for the given type of signal. Hence, bior 2.6 wavelet has been used to decompose the signal further using wavelet packet transform. For in-depth analysis, the signals were decomposed up to 30^{th} level, then statistical analysis was performed on each part of the signal. However, no significant results have been found even after decomposing the signal up to 30^{th} level. The reason behind inefficiency of the given technique to extract a particular frequency of interest possibly due to presence of miniscule frequency content corresponding to thin bearing coating which may get dominated by existing frequencies present in the signal. Hence, a sensitive decomposition technique is required which can

create frequency bands around central frequencies present in the signal. Therefore, Variable mode of decomposition has been implemented on acquired vibration signals to obtain desirable results.

6.3.3 Variational Mode of decomposition

Variational Mode Decomposition (VMD) splits the input signal into distinct band-limited Intrinsic Mode Functions (IMFs). VMD offers advantages over methods like Wavelet Transform (WT) and Empirical mode decomposition (EMD) by eliminating the issue of modal aliasing and exhibiting sensitivity to noise [201]. VMD aims to break down a real-valued input signal into a finite number of sub-signals or modes. These modes possess specific sparsity characteristics while accurately representing the original signal. The sparsity property of each mode is determined by its spectral bandwidth. Essentially, we assume that each mode primarily occupies a compact region centered around a pulsation frequency, which is determined as part of the decomposition process [202]. To determine the bandwidth of each mode, a scheme is suggested, which involves the following steps:

a) Compute the analytic signal corresponding to each mode by applying the Hilbert transform. This allows obtaining a one-sided frequency spectrum for each mode.

b) Translate the frequency spectrum of each mode to the "baseband" by combining it with an exponential function tailored to the estimated center frequency of that mode.

c) Estimate the bandwidth by evaluating the smoothness of the demodulated signal, specifically by measuring the squared norm of the gradient. This estimation is based on the Gaussian smoothness concept. Consequently, the resulting problem to be solved is a constrained variational problem as given in the equation below.

$$\min_{\{u_k\},\{\omega_k\}} \left\{ \sum \left\| \partial_t \left[\left(\delta(t) + \frac{j}{\pi t} \right) * u_k(t) \right] e^{-j\omega_k t} \right\|_2^2 \right\} \quad \text{iv)}$$
$$s \cdot t \cdot \sum_k u_k = f$$

where $\{u_k\} \coloneqq \{u_1 \dots \dots u_k\}$ and $\{\omega_k\} \coloneqq \{\omega_1 \dots \cdot \dots \omega k\}$ representing notations of the entire set of modes and their respective center frequencies.

Equally, $\Sigma_k \coloneqq \sum_{k=1}^{k} f$ is understood as the summation over all modes [202]. The reconstruction constraint can be handled in various ways. In this approach, we

propose employing both a quadratic penalty term and Lagrangian multipliers, λ to make the problem unconstrained. The quadratic penalty method is a traditional approach used to promote constancy in the reconstruction, particularly when dealing with additive independent and identically distributed (i.i.d.) Gaussian noise. The weight of the penalty term is determined based on a Bayesian prior, inversely proportional to the noise level in the data. However, in a noise-free scenario, the weight must be infinitely large to ensure precise data fidelity, which can lead to an ill-conditioned system. On the other hand, Lagrangian multipliers are commonly employed to strictly enforce constraints. The incorporation of both terms brings about advantages by capitalizing on the favorable convergence properties of the quadratic penalty with finite weight, as well as the stringent enforcement of the constraint through the use of the Lagrangian multiplier. Therefore, augmented Lagrangian *L* has been introduced as written in equation (5). [203,204]

$$\mathcal{L}(\{\mu_k\},\{\omega_k\},\lambda) \coloneqq \alpha\Sigma_1\partial t\left[\left(\delta(t)+\frac{j}{\pi t}\right)\times u_k(t)\right]e^{-j\omega_k t}\Big|_2^2 + f(t) - \sum_k u_k(t)|_2^2 + \langle\lambda(t), f(t) - \sum_k u_k(t)\rangle \quad (5)$$

The initial minimization problem's solution is achieved by pinpointing the saddle point of the augmented lagrangian via a series of iterative sub-optimizations, a process known as the alternate direction method of multipliers (ADMM) [205–207]. In accordance with the VMD algorithm, each mode undergoes updates in the frequency domain, and for each iteration, the center frequencies are recalculated.

The Lagrange multiplier serves to enhance the constraint, while a secondary penalty can enhance convergence. If exact reconstruction is not necessary, constraints can be relaxed by solely utilizing the quadratic penalty function and eliminating the need for the Lagrange multiplier. In essence, the quadratic penalty function reflects the precision with which the least squares are connected to the introduced Gaussian noise. The primary procedure of VMD can be briefly outlined as follows [208]:

a) Initialize $\hat{u}^1_k$, ω^1_k, $\lambda\hat{}^1$ initial value of iteration n, maximum number of iteration N;
b) n=n+1, update $\hat{u}_k$ for all $\omega\geq 0$
c) update ω_k for all $\omega\geq 0$

d) update $\lambda\hat{}$

e) Repeat step (b) to (d) until n > N and convergence formula as shown in equation *(6)*

$$\sum_k \| \hat{u}_k^{n+1} - \hat{u}_k^n \|_2^2 / \| \hat{u}_k^n \|_2^2 < \varepsilon \qquad (6)$$

VMD enables the decomposition of a complex echo signal into several modal signals. By eliminating the noise present in the undesired modes and combining the modalities with frequencies close to the transducer's center frequency, the resulting data can be utilized for the reconstruction [209].

6.3.3.1 Intrinsic Mode function

The vmd function in MATLAB software performs the decomposition of a signal $x(t)$ into a limited number K of narrowband intrinsic mode functions (IMFs). The intrinsic mode functions are provided as a matrix or timetable. Each IMF represents an amplitude and frequency modulated signal, featuring positive and slowly changing envelopes. Furthermore, every mode exhibits an instantaneous frequency that progressively increases, changes slowly, and tends to concentrate around a central value [210]. It can be defined mathematically with the help of equation *(7)*

$$x(t) = \sum_{k=1}^{k} u_k(t) \qquad (7)$$

The IMFs exhibit the following characteristics:

- Each mode, u_k, is a signal that combines amplitude and frequency modulation, represented as $u_k(t) = A_k(t)\cos(\phi_k(t))$, where $\phi_k(t)$ represents the phase of the mode and $A_k(t)$ represents its envelope.
- The modes possess positive and gradually changing envelopes.
- Every mode has an instantaneous frequency, $\phi'_k(t)$, that is non-decreasing, changes slowly, and is primarily concentrated around a central value, f_k.

The VMD technique calculates the waveforms of all the modes and their central frequencies simultaneously. The process involves solving a constrained variational problem to determine a set of $u_k(t)$ and $f_k(t)$ that minimizes the objective [49].

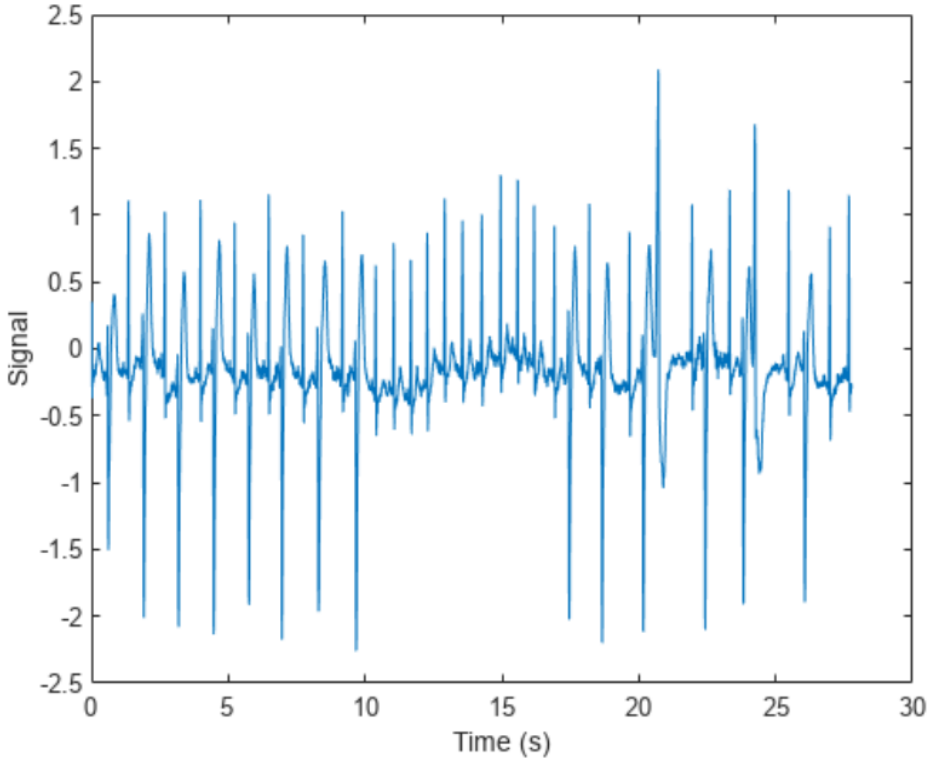

Figure 39: Sample signal plotted w.r.t time in seconds

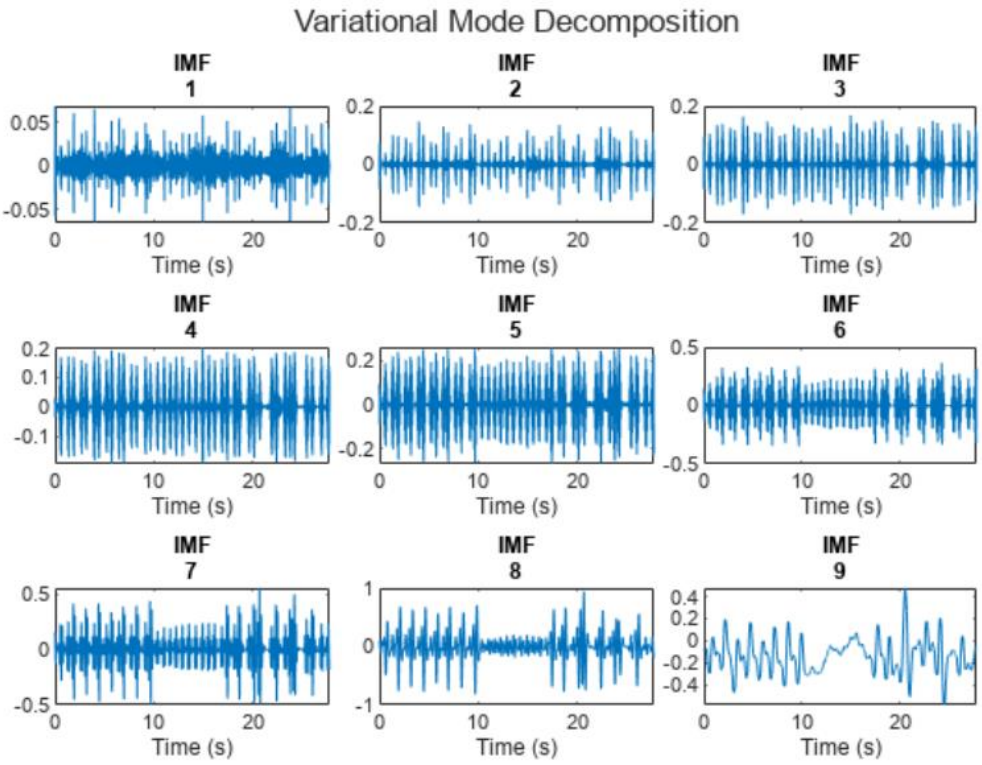

Figure 40: Example of VMD decomposition for an ECG signal [210]

6.3.3.2 General methods to select number of IMFs

- **Maximum Center Frequency Observation Method:** The underlying principle of the Maximum Center Frequency Observation (MCFO) method is to monitor the trend of the maximum center frequencies. As the mode number increases, the maximum center frequency of each mode component gradually rises. Once the maximum center frequencies begin to stabilize, then K value can be found [211].

- **Correlation Coefficient Method:** Correlation coefficient (CC) between the mode components and the original signal can be obtained by the equation *(8)*. Decomposition will be stopped when the minimum correlation coefficient is less than the given threshold, and then K value can be calculated [212]:

$$\rho_{u_{k,f}} = \frac{E(u_k \cdot f) - E(u_k)E(f)}{\sqrt{E(u_k^2) - E^2(u_k)}\sqrt{E(f^2) - E^2(f)}} \quad (8)$$

  Where $\rho_{u_{k,f}}$ depicts the correlation coefficient between the intrinsic mode function (IMF) and the original signal; *f* and u_k illustrates the actual signal and IMF generated by VMD; *E(.)* relates to the mathematical expectation.

- **Normalized Mutual Information Method:** The Mutual Information (MI) value between the intrinsic mode function (IMF) and the original signal is computed using the equation *(9)*. The decomposition process ceases when the minimum value of Normalized Mutual Information (NMI) falls below the specified threshold, enabling the determination of the value of K [212]:

$$MI\ (X, Y) = H(Y) - H(Y|X) \quad (9)$$

  Where *H(Y)* shows information entropy of *Y; H(Y|X)* depicts the conditional entropy of *Y* for known *X*. As the correlation between *X* and *Y* strengthens, the conditional entropy value *H(Y/X)* diminishes, while the mutual information *MI (X, Y)* increases. The normalized mutual information *(NMI)* can be defined with equation *(10)* [212].

$$\delta_i = \frac{MI_i}{max(MI_i)} \quad (10)$$

  where *i* reflects the serial number of the IMF

- **Variance ratio criterion**: The ratio of variances between successive IMF deviations is measured against this criterion. The goal is to pinpoint the maximum or most notable shift in the variance ratio, which would indicate the optimal number of IMFs. The decomposition procedure for this criterion begins by calculating the variances between adjacent IMFs. Examining the ratio of variances to determine if there is a significant change or peak. This change in the variance ratio indicates that the signal is transitioning between distinct modes or frequency components. The criterion focuses on locating the point at which the variance ratio shifts significantly or reaches its maximal value. This value represents the desirable number of IMFs to retain during decomposition. Depending on the application and the characteristics of the analyzed signal, the threshold or condition for determining a significant change in the variance ratio may vary. It can be determined empirically or through prior knowledge of the signal's characteristics [214].

- **Empirical Mode Decomposition (EMD)-Based Methods:** These strategies use EMD to break the signal down into IMFs, and then use statistical analysis to figure out relevant number of IMFs. One method involves looking at the IMFs' instantaneous frequency characteristics. The rate of phase or frequency change within each IMF must be calculated. It is possible to gain insight into the optimal number of IMFs by counting the number of notable shifts or crossings in the frequency content. Analyzing the IMFs' amplitude modulation and frequency modulation properties, or using statistical metrics like kurtosis or skewness to evaluate their characteristics, are two more possible EMD-based approaches. These strategies are geared toward capturing the IMFs' instinctive structure and properties in order to direct the selection of the appropriate number of modes. The signal's characteristics, the level of decomposition required to achieve, and application's needs are all factors that could influence the decision on the EMD-based method to choose. To ascertain how well these strategies perform in actual use, researchers frequently conduct experiments and validate their results against known signals or real time data.

6.3.3.3 Methods to select IMF in case of distributed defects in bearing [53]

As already mentioned earlier, in this work, the purpose is to differentiate the level of properties of bearing coating based on vibration signature of coated bearing. Several researchers since many decades have successfully utilized vibration signature analysis to study the various types of defects in the bearing. However, limited work has been done to study about the properties of bearing surface with vibration signal. Broadly, bearing defects can be categorized into two types as local defect and distributed defect. The nature of this work is somewhat similar to distributed discontinuity as the coating has been done over the whole surface of bearing elements. Therefore, the techniques used to study local defects in bearing may not be able to yield relevant results. Hence, the methods used to select number of IMFs in VMD technique while dealing with distributed defects in bearing has been preferred in this work. The commonly used methods are discussed further:

- **Energy based criteria:** This criterion evaluates the contribution of each IMF to the total signal's energy. Using this method, the relative importance of each IMF to the whole signal's energy level may be determined. When the total energy of the remaining IMFs falls below a certain level, the breakdown process is terminated. The important modes associated with the distributed faults can be determined by taking into account the energy distribution among the IMFs. The process of decomposition proceeds until the remaining IMFs' energy becomes negligible or falls below a predetermined threshold. This indicates that additional decomposition would not significantly contribute to capture the significant features of signal. Using the Energy-Based Criterion, the number of IMFs is determined by the trade-off between capturing essential signal components and averting noise or insignificant modes. The criterion ensures that the retained IMFs comprise the significant energy contributions, enabling an accurate representation of the signal's properties. Depending on the application, signal-to-noise ratio, and level of decomposition desired, the specific threshold for energy reduction may vary. It may be determined empirically or based on prior knowledge of the energy distribution of the signal. It is essential to note that the Energy-Based Criterion is a popular and widely used method due to its simplicity and efficacy in capturing the fundamental modes of the

signal. However, it should be used with caution and in conjunction with other methods to assure a thorough analysis of the signal's characteristics.

- **Kurtosis based criterion:** Kurtosis quantifies the non-Gaussianity or a signal's peaks. In this method, the kurtosis of each IMF is determined, and the decomposition procedure is terminated when the kurtosis values begin to decrease or remain comparatively constant. This suggests that the predominant modes associated with distributed defects have been identified. The Kurtosis-Based Criterion takes into account the turning point or stabilization of the kurtosis values to identify the number of relevant IMFs. This technique uses the kurtosis to take advantage of the unique features of the bearing faults to help choose useful IMFs for further investigation and interpretation. Depending on the bearing's properties and the level of precision required for the decomposition, the threshold or condition for identifying the stability or turning point of the kurtosis data may change. This criterion can be refined and fine-tuned for actual applications with the help of validation against known failure cases and experience in bearing analysis.
- **Frequency Band analysis:** In this method, the frequency content of each IMF is examined to locate unique bands related to the distributed defects. The transitions in the frequency bands across IMFs can be used to estimate the number of relevant IMFs. The frequency content of each IMF derived from the VMD decomposition is examined. This can be accomplished through the use of techniques such as Fourier analysis, wavelet transform, and spectrogram analysis. Observing the frequency spectra or power spectra of the IMFs enables the identification of distinct frequency bands associated with the distributed defects in the bearing. These bands might correspond to particular harmonics, sidebands, or modulation patterns resulting from the defects. In order to learn more about the dispersed flaws, analyze the properties of the discovered frequency bands. To further establish the optimal number of IMFs for capturing the defect-related information, the transitions or variations in frequency bands across the IMFs are also studied. On the basis of the identified frequency bands and their transitions, it is possible to determine the number of relevant IMFs. The number of distinct bands or significant variations in the frequency content indicate the number of IMFs required to effectively represent

the distributed defects. When applying this method, it is essential to consider the signal-to-noise ratio, signal complexity, and defect characteristics. Validation against known defect cases or expert knowledge can boost the precision and reliability of the chosen IMFs.

In this study, the determination of the optimal number of decomposed levels has been carried out based on an energy-based criterion. Energy based method has been chosen because of thin coating on bearing surface. It is anticipated that the impact of balls on the surfaces of a thin coating will generate a correspondingly low-energy event in the vibration signature of the bearing. Therefore, the decomposition process has been conducted with the aim of obtaining a residue that possesses nearly negligible energy. Hence, the vibration signals of coated bearing are decomposed up to six levels with residue having less than 1% relative energy content. Further, statistical analysis was conducted on all six levels of the decomposed signal to determine the frequency band that is most closely associated with changes in the coating's properties

6.3.4 Comparison between EMD, WPT and VMD

Though similar in effectiveness, EMD, WPT, and VMD each take a unique approach to time-frequency analysis and signal decomposition. However, EMD is prone to mode mixing, while being adaptable and well-suited for non-stationary signals. WPT offers a high-resolution, flexible decomposition, but only if nature of the signal is well known in advance. Contrary, VMD is adaptable to non-stationary and non-linear signals, addresses mode mixing efficiently, and has a foundation in variational optimization. In comparison to EMD, it is capable of mitigating errors that can arise from recursive calculations and termination of recursion. VMD exhibits superior noise reduction capabilities compared to the empirical mode decomposition (EMD) method. Unlike EMD, where the number of intrinsic mode functions (IMFs) cannot be manually adjusted, VMD allows for such customization. Additionally, parameters in EMD, like sifting stopping criteria and IMF number determination, must be manually chosen, which can be a subjective and time-consuming process. However, VMD eliminates the requirement for manual involvement by automatically determining the number of modes and their related parameters via variational optimization. The low-frequency

component of VMD accurately captures the overall fluctuation trend of the original signal, a feature that is challenging to observe using EMD. Moreover, in contrast to Empirical Mode Decomposition (EMD), Variational Mode Decomposition (VMD) requires a smaller number of modes to reconstruct the original non-linear signal. This study focuses solely on the three decomposed modes (IMFs) obtained through VMD. The VMD algorithm is more efficient compared to the EMD algorithm because it can decompose a given signal into a smaller number of modes without the need for recursive iterations [215].

In comparison to WPT, VMD is superior at isolating individual signal modes. With VMD, the signal is broken down into clearer modes, each of which has its own unique instantaneous frequency and amplitude. WPT, on the other hand, uses a set of predetermined wavelet basis functions and may not be as effective at isolating complicated signals as other methods. When distinct frequency components are mixed within the same sub-band, mode mixing can occur in WPT. The optimization-based strategy of VMD reduces or eliminates mode blending, resulting in a more precise signal decomposition. Additionally, VMD is typically more resistant to background noise than WPT. Although noise can interfere with the decomposition process in WPT due to the usage of predetermined wavelet bases, VMD's variational optimization framework permits efficient noise separation and improves the clarity of the signal modes. When dealing with large-scale or high-dimensional signals, VMD typically provides faster computing than WPT. In contrast to WPT's tree-based decomposition structure, VMD's optimization-based method can be quickly implemented with numerical optimization algorithms, resulting in shorter decomposition durations. Unlike WPT, which is limited to extracting a single IMF, VMD is capable of simultaneously extracting multiple IMFs. Because of this, VMD is better suited for evaluating signals with a wide range of frequencies. Along with this, VMD exhibits a higher degree of parameter insensitivity compared to WPT, ensuring more consistent outcomes even with slight variations in parameter selection. In comparison to noise-assisted versions of empirical mode decomposition (EMD) and wavelet packet transform (WPT), the parameter-optimized VMD demonstrates superior capability in

effectively separating closely spaced modes while concurrently recovering the most extensive modal information.

Therefore, considering the sensitivity of analyzing bearing coating properties through vibration signals, the VMD technique has been chosen as the preferred method based on the above-mentioned comparative analysis of EMD, WPT, and VMD. The coated vibration signals have been decomposed up to six levels based on energy criterion and statistical analysis of all six levels has been carried out as mentioned earlier also. Further, details about parameters used for the statistical analysis has been discussed in detail.

6.4 Vibration signal analysis

Vibration is a physical occurrence observed in operational rotating machines and moving structures, irrespective of the condition of the machines or structures. Multiple sources, such as shafts, gears, bearings, and structural resonance can induce vibration. Vibration is highly applicable for determining the operational conditions and status of rotating apparatus and structures due to its prevalence. Vibrations are capable of being represented in various ways, including displacement, velocity, and acceleration. Displacement is the distance traveled by the measuring point, velocity is the speed of the movement, and acceleration is the rate of change of velocity. Acceleration, providing the broadest frequency range, is extensively utilized for dynamic fault analysis., is the most popular of the three varieties. For measurement, multiple vibration-detecting sensors are commercially available. There are a wide variety of vibration-based sensors that use technologies including piezoelectric (PZT) sensors, microelectromechanical (MEMS) sensors, proximity probes, laser Doppler vibrometers, and many others to measure displacement, velocity, and acceleration. The proper placement of sensors is essential for gathering reliable information. Stud mounting the sensor on a smooth, flat area of the machine is the suggested way of sensor installation. This guarantees a complete and uniform recording of the electromagnetic spectrum. Magnet holders, wax, or glue can be used as alternatives to stud mounts when vibrational and frequency considerations are more important. Vibration signals are typically below 20 kHz, although certain vibration resonances can exceed this frequency. In practice, the sampling rate must be selected with care to ensure that the

bandwidth containing the frequencies of interest is captured. In addition, the recording duration for one measurement should be at least several periods of the devices' slowest speed. A vibration monitoring system is a comprehensive setup designed to collect vibration signals according to predetermined parameters such as sampling frequency, vibration level, recording duration, recording intervals, and frequency bandwidths. The system should be able to interpret the vibration data and provide machine operators, maintenance personnel, and asset managers with intuitive warnings. There should not be any interreference between system with the normal operation of the monitored devices or structures, and the benefits of the system should outweigh the implementation costs.

Vibration analysis is the process to detect abnormal vibration events and assess the state of the test object by overseeing the magnitudes and patterns of vibration signals within a component or machinery, or building. It is typically performed on both the raw time waveforms of the vibration signal and the frequency spectrum derived from the time waveform using Fourier Transform. Analyzing recorded vibration waveforms in the time domain reveals the occurrence and severity of abnormal vibration events by means of parameters such as RMS, Skewness, Kurtosis, Variance, Shannon entropy, Log energy, and Crest factor. Time domain analysis can monitor the state of the system under observation as a whole. In real-world applications, particularly those involving rotating apparatus, it is highly desirable to include frequency spectrum analysis in addition to time domain analysis. In a complex machine comprising multiple components, vibrations combine to form a composite signal, encompassing the vibrations generated by each rotating component. Hence, evaluating the condition of critical components such as gears, bearings, and shafts in large rotating equipment solely based on time waveforms poses a challenge. With time domain vibration analysis, it is possible to monitor vibration levels and determine the safe operating range. The machine's long-term performance and breakdown records can be used to set these limits. The machine's health is deteriorating and flaws are present when these thresholds are repeatedly crossed. When these limits are surpassed, it indicates a deterioration in the machine's overall health and the occurrence of defects. Nonetheless, frequency analysis dissects time waveforms and delineates the repetitive nature of

vibration patterns to explore the frequency components associated with each individual component. It is possible to detect bearing defects by monitoring the frequency spectrum and studying the periodicity of the collisions.

As mentioned earlier also, in this work, a series of tests have been conducted on coated bearings, varying their rotational speeds from 300 rpm to 1500 rpm. During these tests, the vibration signals generated by the bearings were recorded. These recorded vibration signals exhibited distinct characteristics that are influenced by the properties of the ball rolling on different surfaces. As a result, the signals displayed a distributed nature.

To analyze the distributed characteristics of the signals, several commonly used statistical parameters were calculated, including Root Mean Square (RMS), Crest factor, Variance, Skewness, Kurtosis, Shannon entropy (SE), and Log energy (LE). The intention is to assess the correlation between these parameters and the different levels of properties present, but no significant relationship was found. The probable reason for getting no response in statistical parameters might be because of weak characteristics of surface roughness in the overall signal. Therefore, for further investigation, signals are decomposed into intrinsic mode functions (IMF) using Variational Mode Decomposition (VMD) technique. This decomposition process effectively isolates narrow frequency bands centered around prominent frequencies present in the signal. The same set of statistical parameters are then recalculated for each of these decomposed levels. The usage of statistical parameters in vibration signal analysis continued to be a preferred choice of many authors because of its simplicity, precision, reliability, and quicker computation [221-232]. Moreover, statistical parameters have also been used to extract information about the level of properties [227-230], which is of prime concern in this research work. The following features are encouraging the use of statistical parameters like finding out energy content present in signal, dispersion of the data, variation in data, impulsiveness of the signal and degree of randomness and so on. The statistical parameters with characteristics to cover important features present in the signal are selected are discussed with their significance.

a) RMS (Root Mean Square): Root mean square, in general, estimates the entire power intensity of an acoustic/vibration signal [80]. It is simply the square root of the

signal's average squared value. The strength of the vibrating signal created by rolling elements defines the signal's intensity. It is one of the statistical parameters used to predict the surface roughness in machining process using vibration signal analysis [227].

b) Crest Factor: The crest factor is the ratio of the crest value (the largest absolute value attained by the functions representing of the signal during the time period under consideration) to the root mean square value of the signal [231]. Crest factor proved to be an important parameter for differentiating healthy bearing from bearing with distributed defects like pitting, scratching, or misalignment [232].

c) Variance: Variance (σ^2) is the average of a data set's squared difference from the mean. Equation *(11)* gives the variance of a set of numbers, x_n, $n = 1, \ldots, N$, with a known mean value of μ [233]. Variance is also considered to be among important statistical parameter to discriminate fault conditions [234]

$$\sigma^2 = \frac{1}{N} \sum_{n=1}^{N} (x_n - \mu)^2 \qquad (11)$$

d) Skewness: Because a normal distribution has zero skewness, any symmetrical data should have skewness close to zero as well. When the skewness is negative, the data is skewed to the left of the normal distribution curve and skewed right when the skewness is positive. When there are noticeable peaks in the signal, it often produces a larger value [233]. Skewness is commonly used to extract features of vibration signal with statistical computations [229]. Mathematically, it can be defined with the help of equation *(12)* [224].

$$Skewness = \frac{1}{n} \sum_{k=1}^{n} ((x_k - \bar{x})^3 \frac{1}{\sigma^3} \qquad (12)$$

e) Kurtosis: Kurtosis is a statistical metric used to assess impulsiveness by calculating the peak and tails of a temporal domain signal. A bearing in excellent condition has a Kurtosis value of a Gaussian curve and its signal is near to three, but the Kurtosis value of a damaged bearing is greater than three [235]. The Kurtosis factor has been used to analyze local defect signals but not much explored in detecting distributed

characteristics of the signal. Mathematical expression for kurtosis is shown in equation *(13)* [224] is,

$$Kurtosis = \frac{\frac{1}{n}\sum_{k=1}^{n}[x_k-\bar{x}]^4}{\left[\frac{1}{n}\sum_{k=1}^{n}[x_k-\bar{x}]^2\right]^2} \quad (13)$$

The given statistical term has been used by many authors to differentiate healthy and faulty bearing or to extract relevant information from the vibration signal statistically [220-224, 234, 236]

f) Shannon Entropy: It provides insights into the level of randomness within the signal i.e., random signal alterations. Shannon Entropy is the metric used to assess changes in a signal because of different characteristics on a logarithmic scale (SE). The more is the changes in the characteristics in the signal more will be the change in value. The change is expected to bring variation in the level of randomness contained within the signal. It amplifies the characteristics of the signal in the form of randomness such that even small disturbances can be highlighted using SE [237]. The measure of randomness has been used in a variety of applications such as identifying gear problems, image processing, motor defect analysis, and structural health audits to examine various features. Because of its capacity to process signals on a logarithmic scale, it may serve as a significant criterion for representing the diverse features of coating in addition to its many uses. Mathematically, it is expressed as equation *(14)* [224].

$$S(Z) = -\sum_{i=0}^{X-1} z_i^2 \, log_2[P(z_i)]^2 \quad (14)$$

Shannon entropy is another important statistical parameter and widely used in diagnostic and monitoring analysis of bearing [221-224, 229, 237,] and used in the study carried out to extract features of vibration signal for the monitoring of important coating property i.e., surface finish in CNC operation [222].

g) Logarithmic Energy: The statistical feature with the capability of measuring uncertainty proved to be an effective indicator of the fault severity. Mathematically, expressed in equation *(15)* [238].

$$L(Z) = -\sum_{i=0}^{X-1} log_2[P(z_i)]^2 \quad (15)$$

In log energy, representative features are retrieved in sub-bands of interest as a measure of the degree of disturbance. If the chance of occurrence for each discrete state is roughly equal, then this entropy is lower. Log energy is already used as representative feature in the study of early fault detection in bearings [239].

After introduction of all statistical parameters, all obtained results needs to be presented in tabular form in reference to specified property of the coated material. Therefore, starting with surface roughness, after calculating values of previously defined statistical parameters, results are presented in reference to surface roughness.

6.4.1 Study of variation in statistical parameters in reference to surface roughness

To find out the responsive parameter in response to variation in surface roughness, results of statistical analysis are presented in tabular form. In these tables, the coatings are arranged in ascending order of surface roughness so that it becomes easier to identify similar upward or downward trend in any of the statistical parameters (specified earlier). Initially, simple statistical analysis has been carried out on acquired vibration signals as shown in the Table 10 to Table 14. No considerable trend is obtained in any of the statistical parameter reference to variation in surface roughness from 300 to 1200 rpm.

Table 10: Calculated statistical parameters of acquired vibration signal at 300 rpm

Coating	*R_a*	*RMS*	*Skewness*	*Kurtosis*	*Variance*	*Shannon Entropy*	*Log Energy*	*Crest Factor*
Nickel	0.29	0.3483	-0.0549	6.6457	0.0084	1.5380E+04	-1.4521E+05	4.3904
Copper	0.52	0.5303	0.0212	24.0533	0.1352	9.4413E+03	-1.5015E+05	16.9466
ZnP	0.7	0.5539	-0.0604	4.7608	0.0759	1.5467E+04	-1.1623E+05	5.4113
Silver	2.65	0.6030	0.4346	42.8313	0.1241	8.1855E+03	-1.0988E+05	13.6759
Black Oxide	3.22	0.5062	0.0157	3.5156	0.1241	1.2158E+04	-1.5690E+05	5.3841

Table 11: Calculated statistical parameters of acquired vibration signal at 600 rpm

Coating	*R_a*	*RMS*	*Skewness*	*Kurtosis*	*Variance*	*Shannon Entropy*	*Log Energy*	*Crest Factor*
Nickel	0.29	0.4240	-0.0512	6.9079	0.0657	1.3613E+04	-1.6413E+05	8.4871
Copper	0.52	0.5785	-0.0464	3.8190	0.1429	1.1206E+04	-1.3404E+05	5.2815
ZnP	0.7	0.7168	0.7289	36.5291	0.2880	-1.3361E+04	-1.1924E+05	17.5162
Silver	2.65	0.6039	0.0526	15.2910	0.2197	3.2207E+03	-1.4386E+05	12.8050
Black Oxide	3.22	1.3020	0.0617	3.2082	1.5628	-1.4040E+05	-4.9631E+04	4.5811

Table 12: Calculated statistical parameters of acquired vibration signal at 900 rpm

Coating	*R_a*	*RMS*	*Skewness*	*Kurtosis*	*Variance*	*Shannon Entropy*	*Log Energy*	*Crest Factor*
Nickel	0.29	0.6878	0.0661	6.4600	0.3594	-4.8971E+03	-1.3604E+05	8.5603
Copper	0.52	0.8759	-0.0206	3.6320	0.5609	-2.3209E+04	-9.7597E+04	6.4620
ZnP	0.7	1.3640	0.5979	31.6941	1.6630	-2.9778E+05	-8.6381E+04	17.7376
Silver	2.65	1.0419	-0.0032	6.4559	0.9125	-7.1170E+04	-8.5177E+04	9.3617
Black Oxide	3.22	2.1142	0.0499	3.1541	4.3430	-6.4608E+05	1.2190E+04	5.1794

Table 13: Calculated statistical parameters of acquired vibration signal at 1200 rpm

Coating	*Ra*	*RMS*	*Skewness*	*Kurtosis*	*Variance*	*Shannon Entropy*	*Log Energy*	*Crest Factor*
Nickel	0.29	0.9157	0.0746	6.8410	0.7158	-4.4123E+04	-1.0547E+05	9.5801
Copper	0.52	1.3137	-0.0104	3.5016	1.5141	-1.4497E+05	-4.7965E+04	6.5199
ZnP	0.7	1.8629	0.2448	19.3549	3.2666	-6.4716E+05	-4.4193E+04	13.4397
Silver	2.65	1.6567	-0.0031	8.0532	2.5606	-3.7475E+05	-3.5971E+04	11.6506
Black Oxide	3.22	3.3363	0.0890	3.2619	11.0010	-2.2693E+06	7.0207E+04	5.0021

Table 14: Calculated statistical parameters of acquired vibration signal at 1500 rpm

Coating	*R_a*	*RMS*	*Skewness*	*Kurtosis*	*Variance*	*Shannon Entropy*	*Log Energy*	*Crest Factor*
Nickel	0.29	1.7112	0.0068	7.3779	2.7967	-4.0019E+05	-2.9785E+04	12.9099
Copper	0.52	1.9870	0.0133	3.4406	3.6855	-5.4450E+05	3.5729E+03	5.9436
ZnP	0.7	1.9888	0.0469	13.8614	3.7372	-7.0755E+05	-2.3921E+04	12.2110
Silver	2.65	2.7803	-0.0217	8.4975	7.5545	-1.6260E+06	2.1392E+04	10.1144
Black Oxide	3.22	4.4616	0.0181	3.5697	19.7852	-4.8394E+06	1.0585E+05	6.8683

However, at 1500 rpm, RMS and Shannon entropy has shown continuous rising trend with the increase in surface roughness as shown in Table 14. Based on this result, it can

be stated that rise in power and randomness of the vibration signal is noticeable with the increase in surface roughness of mating surfaces at 1500 rpm. Further, in order to find out most sensitive parameter among these two, chain indexing has been carried out as shown in Table 15. With average percentage variation of 98.35%, it is clear that Shannon entropy is much more sensitive than RMS towards variation in roughness at 1500 rpm. It reflects that signal acquired for different coatings below 1500 rpm cannot be differentiated in reference to surface characteristics with simple statistical analysis. Therefore, decomposition of the signals was carried out using VMD as mentioned earlier.

Table 15: Chain indexing of responded parameters at 1500 rpm

S. No	***Coating***	***R_a***	***RMS***	***Chain Index***	***Shannon entropy***	***Chain Index***
1	Nickel	0.29	1.7112	--	-4.0019E+05	--
2	Copper	0.52	1.9870	16.1173	-5.4450E+05	36.0604
3	ZnP	0.7	1.9888	0.0906	-7.0755E+05	29.9449
4	Silver	2.65	2.7803	39.7979	-1.6260E+06	129.8071
5	Black Oxide	3.22	4.4616	60.4719	-4.8394E+06	197.6261
Average Chain Index				***29.11***		***98.35***

After decomposition, the statistical parameters of all six modes are calculated and relevant outcomes are illustrated next in tabular form. Decomposition was stopped at sixth level because beyond that, the percentage of relative energy content in the signal is extremely low. However, in the process of finalizing decomposition up to sixth level, it was kept in mind that essence of thin coating in vibration signal is going to be a low energy event only. Therefore, decomposition was extended up to sixth level to cover relevant low energy events also in the calculations.

Table 16: Statistical parameters of IMF 1 at 300 rpm

Coating	***R_a***	***RMS***	***Skewness***	***Kurtosis***	***Variance***	***Shannon Entropy***	***Log Energy***	***Crest Factor***
Nickel	0.29	0.0211	0.0026	7.5290	0.0004	1.9136E+02	-5.8614E+05	13.9519
Copper	0.52	0.0871	0.1464	68.3347	0.0076	1.4702E+03	-4.3350E+05	29.2495
ZnP	0.7	0.0395	0.0015	3.3055	0.0016	5.6840E+02	-4.9727E+05	6.1717
Silver	2.65	0.1128	0.0002	70.2502	0.0127	1.7526E+03	-4.0967E+05	23.4350
Black Oxide	3.22	0.1025	0.0005	3.1083	0.0105	2.5586E+03	-3.7408E+05	4.3417

Table 17: Statistical parameters of IMF 2 at 300 rpm

Coating	R_a	*RMS*	*Skewness*	*Kurtosis*	*Variance*	*Shannon Entropy*	*Log Energy*	*Crest Factor*
Nickel	0.29	0.0222	0.0026	29.0549	0.0005	1.9787E+02	-5.8891E+05	23.4255
Copper	0.52	0.1801	0.0022	20.5296	0.0325	4.5628E+03	-3.1735E+05	18.9200
ZnP	0.7	0.0443	0.0031	4.1635	0.0020	6.7353E+02	-4.8814E+05	7.1655
Silver	2.65	0.1530	-0.0123	46.8417	0.0234	2.4652E+03	-3.7574E+05	19.4516
Black Oxide	3.22	0.0966	0.0048	3.2972	0.0093	2.3314E+03	-3.8304E+05	5.2231

Table 18: Statistical parameters of IMF 3 at 300 rpm

Coating	R_a	*RMS*	*Skewness*	*Kurtosis*	*Variance*	*Shannon Entropy*	*Log Energy*	*Crest Factor*
Nickel	0.29	0.0290	0.0078	14.0081	0.0008	3.0828E+02	-5.6268E+05	13.1508
Copper	0.52	0.1488	0.0006	8.5246	0.0222	3.9101E+03	-3.3755E+05	11.9742
ZnP	0.7	0.0540	-0.0063	23.4947	0.0029	8.3061E+02	-4.7778E+05	18.1938
Silver	2.65	0.1543	0.0027	36.5897	0.0238	2.4941E+03	-3.8303E+05	17.7908
Black Oxide	3.22	0.1577	0.0008	4.2258	0.0249	4.5630E+03	-3.2225E+05	8.9797

Table 19: Statistical parameters of IMF 4 at 300 rpm

Coating	R_a	*RMS*	*Skewness*	*Kurtosis*	*Variance*	*Shannon Entropy*	*Log Energy*	*Crest Factor*
Nickel	0.29	0.0399	-0.0050	9.6108	0.0016	5.2925E+02	-5.2122E+05	11.5277
Copper	0.52	0.0859	-0.0082	4.2707	0.0074	1.9060E+03	-4.0305E+05	7.1574
ZnP	0.7	0.0764	-0.0022	11.8841	0.0058	1.4354E+03	-4.3644E+05	11.6646
Silver	2.65	0.1466	0.0008	14.6782	0.0215	3.1964E+03	-3.6214E+05	10.6533
Black Oxide	3.22	0.1819	-0.0019	3.4225	0.0331	5.5076E+03	-3.0556E+05	4.9911

Table 20: Statistical parameters of IMF 5 at 300 rpm

Coating	R_a	*RMS*	*Skewness*	*Kurtosis*	*Variance*	*Shannon Entropy*	*Log Energy*	*Crest Factor*
Nickel	0.29	0.0501	-0.0177	5.3196	0.0025	7.8921E+02	-4.8717E+05	5.7100
Copper	0.52	0.1436	-0.0059	4.9765	0.0206	3.8464E+03	-3.4237E+05	6.7712
ZnP	0.7	0.0545	0.0793	4.1068	0.0030	9.3973E+02	-4.6224E+05	6.4678
Silver	2.65	0.0865	-0.0622	6.9086	0.0075	1.7928E+03	-4.1757E+05	7.8006
Black Oxide	3.22	0.1396	0.0132	3.1170	0.0195	3.9753E+03	-3.3478E+05	4.5140

Table 21: Statistical parameters of IMF 6 at 300 rpm

Coating	*R_a*	*RMS*	*Skewness*	*Kurtosis*	*Variance*	*Shannon Entropy*	*Log Energy*	*Crest Factor*
Nickel	0.29	0.3371	0.0270	3.0426	0.0007	1.5732E+04	-1.3993E+05	1.3129
Copper	0.52	0.3845	-0.0934	3.4511	0.0018	1.7863E+04	-1.2391E+05	1.4332
ZnP	0.7	0.4586	0.1143	2.7605	0.0020	2.0728E+04	-1.0103E+05	1.3400
Silver	2.65	0.4908	-0.1571	3.2507	0.0013	2.1775E+04	-9.1821E+04	1.2719
Black Oxide	3.22	0.3671	0.0053	3.1491	0.0026	1.6961E+04	-1.3079E+05	1.6170

From results presented in Table 16 to Table 21, it was observed that at 300 rpm, no significant trend was found in any of the statistical parameter with the variation in R_a. Absence of any trend is due to presence of weak harmonics in the signal corresponding to roughness level or the given technique was unable to differentiate the roughness characteristics at low speed. Only the tables (values of statistical parameters in tabular form) of responded IMFs have been presented and discussed further. Remaining tables of all IMFs at all speeds are added in Appendix

Table 22: Statistical parameters of IMF 6 at 600 rpm

Coating	*R_a*	*RMS*	*Skewness*	*Kurtosis*	*Variance*	*Shannon Entropy*	*Log Energy*	*Crest Factor*
Nickel	0.29	0.3416	0.0689	3.1202	0.0026	1.5709E+04	-1.4047E+05	1.6221
Copper	0.52	0.3922	0.0410	3.3110	0.0043	1.7879E+04	-1.2360E+05	1.7043
ZnP	0.7	0.4176	0.3074	5.9950	0.0092	1.8333E+04	-1.1916E+05	3.7997
Silver	2.65	0.4554	-0.0248	3.2999	0.0093	1.9722E+04	-1.0695E+05	1.8395
Black Oxide	3.22	0.4594	-0.0045	3.2959	0.0081	1.9992E+04	-1.0486E+05	2.2225

Table 23: Statistical parameters of IMF 4 at 900 rpm

Coating	*R_a*	*RMS*	*Skewness*	*Kurtosis*	*Variance*	*Shannon Entropy*	*Log Energy*	*Crest Factor*
Nickel	0.29	0.2145	0.0253	11.5853	0.0460	4.9698E+03	-3.1531E+05	12.4978
Copper	0.52	1.1888	-0.0002	3.6845	1.4132	-1.0802E+05	-6.7736E+04	4.6418
ZnP	0.7	1.4660	0.0004	3.3983	2.1491	-2.1658E+05	-3.9258E+04	4.2566
Silver	2.65	1.1008	0.0135	4.7679	1.2118	-9.1663E+04	-8.6184E+04	6.5777
Black Oxide	3.22	1.4370	0.0013	3.1161	2.0651	-1.9524E+05	-3.7115E+04	4.5632

Table 24: Statistical parameters of IMF 2 at 1200 rpm

Coating	*R_a*	*RMS*	*Skewness*	*Kurtosis*	*Variance*	*Shannon Entropy*	*Log Energy*	*Crest Factor*
Nickel	0.29	0.4457	0.0172	13.4801	0.1986	-1.3447E+02	-2.4237E+05	12.1138
Copper	0.52	1.0156	0.0031	4.0636	1.0314	-6.1044E+04	-9.0671E+04	5.9267
ZnP	0.7	1.0281	-0.0019	7.2462	1.0569	-8.1241E+04	-1.0064E+05	9.6025
Silver	2.65	1.3398	0.0143	26.8203	1.7950	-3.0240E+05	-3.0174E+05	17.2483
Black Oxide	3.22	1.8366	-0.0015	3.7760	3.3733	-4.4557E+05	-1.0732E+04	5.8560

At 600, 900 and 1200 rpm, considerable variation in characteristics of the signal like energy level (RMS), dispersion of data from mean (Variance) and degree of randomness (Shannon entropy) were noticed. All three parameters were showing rising trend in 6th, 4th, and 2nd IMF respectively with the increase in R_a as shown in Table 22, Table 23 and Table 24.

Table 25: Statistical parameters of IMF 2 at 1500 rpm

Coating	*R_a*	*RMS*	*Skewness*	*Kurtosis*	*Variance*	*Shannon Entropy*	*Log Energy*	*Crest Factor*
Nickel	0.29	0.7251	0.0100	6.5700	0.5257	-1.8766E+04	-1.5574E+05	6.7257
Copper	0.52	0.8957	-0.0014	3.1598	0.8022	-2.6915E+04	-9.5922E+04	5.5265
ZnP	0.7	0.8923	0.0054	19.3354	0.7963	-8.5186E+04	-1.5613E+05	10.5387
Silver	2.65	1.0875	0.0034	8.3551	1.1827	-1.1187E+05	-1.0722E+05	9.9914
Black Oxide	3.22	2.8276	-0.0012	3.4671	7.9954	-1.4725E+06	4.7083E+04	5.8121

However, at 1500 rpm, only randomness level continued to depict rising trend in IMF 2 with the rise in R_a as shown in Table 25.

Table 26: IMF wise different responsive statistical parameters at different speed

S. No	*RPM*	*IMF level shown response*	*Responding statistical parameters (SPs)*
1	300	None	None
2	600	6	RMS, Variance, SE
3	900	4	RMS, Variance, SE
4	1200	2	RMS, Variance, SE
5	1500	2	SE

The occurrence of rising trend in above mentioned IMFs at different speeds is due to interaction of bearing balls with different coatings. Each coated material possesses

different damping characteristic thus, generating unique frequency bands due to balls rolling on the surfaces of different roughness. Therefore, corresponding roughness characteristics can be obtained in responsive frequency bands of vibration signal.

However, due to thin film of the coating, responded IMFs are of low energy as compared to energies of other common frequencies present in signal like BPFO, BPFI or cage frequency. That is why, no consistent trend has been found between various modes and distribution of relative energy at all speeds in all coatings. The results in tabular form are presented in Appendix .

Further, to compare the level of variation among responsive statistical parameters in reference to $R_{a,}$ chain indexing has been used. Chain indexing gives percentage variation in consecutive values. The variation in value of statistical parameters were calculated in percentage while moving from one surface roughness level to other. Based on chain indexing, at 600 rpm, it has been observed that beyond R_a value of 0.7, the value of chain index is comparatively negligible. Therefore, even though three statistical parameters have shown rising trend in reference to increase in R_a but rate of variation is almost negligible. The reason behind this minute variation could be same as in case of 300 rpm. Hence, no significant results have been obtained at 600 rpm also as presented in

Table **27**.

Table 27: Responded statistical parameters at 600 RPM in IMF 6 with its chain index.

S. No	***Coating***	***R_a***	***RMS***	***Chain Index***	***Variance***	***Chain Index***	***Shannon entropy***	***Chain Index***
1	Nickel	0.29	0.3416	--	0.0026	--	1.5709E+04	--
2	Copper	0.52	0.3922	14.814	0.0043	65.839	1.7879E+04	13.812
3	ZnP	0.7	0.4176	6.494	0.0092	111.641	1.8333E+04	2.541
4	Silver	2.65	0.4554	9.056	0.0093	1.531	1.9722E+04	7.573
5	Black Oxide	3.22	0.4594	0.861	0.0094	1.326	1.9992E+04	1.370
Average Chain Index				***7.80***		***45.08***		***6.32***

However, at 900 rpm, all three responsive parameters have shown considerable minimum variation at each level as shown in Table 28. The selection of most appropriate parameter has been done based on the value of minimum variation. Therefore, based on comparison of chain index values, randomness level found to be most relevant parameter at the given speed to estimate level of surface roughness.

Table 28: Responded statistical parameters at 900 RPM in IMF 4 with its chain index.

S. No	***Coating***	***R_a***	***RMS***	***Chain Index***	***Variance***	***Chain Index***	***Shannon entropy***	***Chain Index***
1	Nickel	0.29	0.1692		0.0286		9.7675E+02	
2	Copper	0.52	0.2772	63.840	0.0768	168.436	3.5166E+03	260.032
3	ZnP	0.7	0.6702	141.831	0.4492	484.821	8.6090E+03	144.810
4	Silver	2.65	0.7767	15.887	0.6033	34.297	1.7476E+04	102.996
5	Black Oxide	3.22	1.2654	62.918	1.6013	165.423	2.4901E+05	1324.891
Average Chain Index				***71.12***		***213.24***		***458.18***

Further at 1200 rpm, insignificant high variation in chain index values is observed in RMS and variance. Contrary, Shannon entropy depicting considerable variation in values of chain index. Overall, based on the minimum variation in percentage, randomness level surpasses both other parameters as depicted in Table 29.

Finally, again at 1500 rpm, out of three responsive parameters, only degree of randomness continued to show considerable rising trend as shown in Table 30.

Table 29: Responded statistical parameters at 1200 RPM in IMF 2 with its chain index.

S. No	***Coating***	***R_a***	***RMS***	***Chain Index***	***Variance***	***Chain Index***	***Shannon entropy***	***Chain Index***
1	Nickel	0.29	0.4457		0.1986		1.3447E+04	
2	Copper	0.52	1.0156	127.884	1.0314	419.311	6.1044E+04	353.953
3	ZnP	0.7	1.0281	1.237	1.0569	2.474	8.1241E+04	33.085
4	Silver	2.65	1.3398	30.309	1.7950	69.829	3.0240E+05	272.221
5	Black Oxide	3.22	1.8366	37.088	3.3733	87.930	4.4557E+05	47.346
Average Chain Index				***49.12***		***144.89***		***176.65***

Table 30: Responded statistical parameters at 1500 RPM in IMF 2 with its chain index.

S. No	*Coating*	*R_a*	*RMS*	*Chain Index*	*Variance*	*Chain Index*	*Shannon entropy*	*Chain Index*
1	Nickel	0.29	0.7251		0.5257		1.8766E+04	
2	Copper	0.52	0.8957	23.529	0.8022	52.593	2.6915E+04	43.421
3	ZnP	0.7	0.8923	-0.370	0.7963	-0.740	8.5186E+04	216.502
4	Silver	2.65	1.0875	21.872	1.1827	48.528	1.1187E+05	31.323
5	Black Oxide	3.22	2.8276	160.009	7.9954	576.028	1.4725E+06	1216.260
Average Chain Index				***51.26***		***169.10***		***376.87***

From results, it is also clear that with the rise in rpm, central frequencies responsible to create IMFs were found to be shifted towards higher bands as shown in Table 31. Based on the highest value of average chain index, the effect of surface roughness variation can be seen at its best in IMF 4 at 900 rpm with the help of Shannon entropy. Therefore, Shannon entropy found to be a reliable indicator of surface roughness level for bearing surface running between 900 to 1500 rpm.

Table 31: Responsive IMF and statistical parameters at different rpm

S. No	*RPM*	*IMF level shown response*	*Approximate Frequencies Band (Hz)*	*Responding statistical parameters*	*Average chain index*
1	300	None	None	None	NA
2	600	6	0.0058-431	Variance (Insignificant)	NA
3	900	4	567-2100	Shannon entropy	458.18
4	1200	2	2250-4490	Shannon entropy	176.65
5	1500	2	3010-4590	Shannon entropy	376.87

6.4.2 Study of variation in statistical parameters in reference to hardness

To find out the responsive statistical parameter in relation to variation in hardness, again results are presented in tabular form. In these tables, the coatings are now arranged in ascending order of hardness so that it becomes easier to identify similar upward or downward trend in any of the statistical parameters. Firstly, attempt has been made to find out a relevant trend in reference to hardness from the statistical analysis of acquired vibration signal. The results are presented in Table 32 to Table 36.

Table 32: Calculated statistical parameters of acquired vibration signal at 300 rpm

Coating	*HV*	*RMS*	*Skewness*	*Kurtosis*	*Variance*	*Shannon Entropy*	*Log Energy*	*Crest Factor*
Silver	192	0.603	0.4346	42.8313	0.1241	8.19E+03	-1.10E+05	13.6759
Copper	491	0.5303	0.0212	24.0533	0.1352	9.44E+03	-1.50E+05	16.9466
ZnP	539	0.5539	-0.0604	4.7608	0.0759	1.55E+04	-1.16E+05	5.4113
Nickel	614	0.3622	0.2099	16.9047	0.0105	1.58E+04	-1.41E+05	7.5891
Black Oxide	624	0.5062	0.0157	3.5156	0.1241	1.22E+04	-1.57E+05	5.3841

Table 33: Calculated statistical parameters of acquired vibration signal at 600 rpm

Coating	*HV*	*RMS*	*Skewness*	*Kurtosis*	*Variance*	*Shannon Entropy*	*Log Energy*	*Crest Factor*
Silver	192	0.6039	0.0526	15.291	2.20E-01	3.22E+03	-143860	12.805
Copper	491	0.5785	-0.0464	3.819	0.1429	1.12E+04	-1.34E+05	5.2815
ZnP	539	1.6964	0.0712	7.6801	2.7124	-3.98E+05	-3.12E+04	11.8225
Nickel	614	0.4543	0.1271	6.8154	0.0843	1.28E+04	-1.60E+05	7.3244
Black Oxide	624	1.9627	0.04	3.5348	3.729	-5.37E+05	-2.93E+03	4.9784

Table 34: Calculated statistical parameters of acquired vibration signal at 900 rpm

Coating	*HV*	*RMS*	*Skewness*	*Kurtosis*	*Variance*	*Shannon Entropy*	*Log Energy*	*Crest Factor*
Silver	192	1.0419	-0.0032	6.4559	0.9125	-7.12E+04	-8.52E+04	9.3617
Copper	491	0.8759	-0.0206	3.632	0.5609	-2.32E+04	-9.76E+04	6.462
ZnP	539	1.364	0.5979	31.6941	1.663	-2.98E+05	-8.64E+04	17.7376
Nickel	614	0.6878	0.0661	6.46	0.3594	-4.90E+03	-1.36E+05	8.5603
Black Oxide	624	2.1142	0.0499	3.1541	4.343	-6.46E+05	1.22E+04	5.1794

Table 35: Calculated statistical parameters of acquired vibration signal at 1200 rpm

Coating	*HV*	*RMS*	*Skewness*	*Kurtosis*	*Variance*	*Shannon Entropy*	*Log Energy*	*Crest Factor*
Silver	192	1.6567	-0.0031	8.0532	2.5606	-3.75E+05	-3.60E+04	11.6506
Copper	491	1.3137	-0.0104	3.5016	1.5141	-1.45E+05	-4.80E+04	6.5199
ZnP	539	1.8629	0.2448	19.3549	3.2666	-6.47E+05	-4.42E+04	13.4397
Nickel	614	0.9157	0.0746	6.841	0.7158	-4.41E+04	-1.05E+05	9.5801
Black Oxide	624	3.3363	0.089	3.2619	11.001	-2.27E+06	7.02E+04	5.0021

Table 36: Calculated statistical parameters of acquired vibration signal at 1500 rpm

Coating	*HV*	*RMS*	*Skewness*	*Kurtosis*	*Variance*	*Shannon Entropy*	*Log Energy*	*Crest Factor*
Silver	192	2.7803	-0.0217	8.4975	7.5545	-1.63E+06	2.14E+04	10.1144
Copper	491	1.987	0.0133	3.4406	3.6855	-5.45E+05	3.57E+03	5.9436
ZnP	539	1.9888	0.0469	13.8614	3.7372	-7.08E+05	-2.39E+04	12.211
Nickel	614	1.7112	0.0068	7.3779	2.7967	-4.00E+05	-2.98E+04	12.9099
Black Oxide	624	4.4616	0.0181	3.5697	19.7852	-4.84E+06	1.06E+05	6.8683

However, no considerable trend has been found with the calculations of statistical parameters directly. Therefore, for in depth analysis, the signals are decomposed into six levels using VMD. After decomposition, the statistical parameters (specified earlier) of all six modes at all speeds are calculated and outcomes are illustrated from Table 37 to Table 66.

Table 37: Statistical parameters of IMF 1 at 300 rpm

Coating	*HV*	*RMS*	*Skewness*	*Kurtosis*	*Variance*	*Shannon Entropy*	*Log Energy*	*Crest Factor*
Silver	192	0.1128	0.0002	70.2502	0.0127	1.75E+03	-4.10E+05	23.435
Copper	491	0.0871	0.1464	68.3347	0.0076	1.47E+03	-4.34E+05	29.2495
ZnP	539	0.0395	0.0015	3.3055	0.0016	5.68E+02	-4.97E+05	6.1717
Nickel	614	0.0211	0.0026	7.529	0.0004	1.91E+02	-5.86E+05	13.9519
Black Oxide	624	0.1025	0.0005	3.1083	0.0105	2.56E+03	-3.74E+05	4.3417

Table 38: Statistical parameters of IMF 2 at 300 rpm

Coating	*HV*	*RMS*	*Skewness*	*Kurtosis*	*Variance*	*Shannon Entropy*	*Log Energy*	*Crest Factor*
Silver	192	0.153	-0.0123	46.8417	0.0234	2.47E+03	-3.76E+05	19.4516
Copper	491	0.1801	0.0022	20.5296	0.0325	4.56E+03	-3.17E+05	18.92
ZnP	539	0.0443	0.0031	4.1635	0.002	6.74E+02	-4.88E+05	7.1655
Nickel	614	0.0222	0.0026	29.0549	0.0005	1.98E+02	-5.89E+05	23.4255
Black Oxide	624	0.0966	0.0048	3.2972	0.0093	2.33E+03	-3.83E+05	5.2231

Table 39: Statistical parameters of IMF 3 at 300 rpm

Coating	*HV*	*RMS*	*Skewness*	*Kurtosis*	*Variance*	*Shannon Entropy*	*Log Energy*	*Crest Factor*
Silver	192	0.1543	0.0027	36.5897	0.0238	2.49E+03	-3.83E+05	17.7908
Copper	491	0.1488	0.0006	8.5246	0.0222	3.91E+03	-3.38E+05	11.9742
ZnP	539	0.054	-0.0063	23.4947	0.0029	8.31E+02	-4.78E+05	18.1938
Nickel	614	0.029	0.0078	14.0081	0.0008	3.08E+02	-5.63E+05	13.1508
Black Oxide	624	0.1577	0.0008	4.2258	0.0249	4.56E+03	-3.22E+05	8.9797

Table 40: Statistical parameters of IMF 4 at 300 rpm

Coating	*HV*	*RMS*	*Skewness*	*Kurtosis*	*Variance*	*Shannon Entropy*	*Log Energy*	*Crest Factor*
Silver	192	0.1466	0.0008	14.6782	0.0215	3.20E+03	-3.62E+05	10.6533
Copper	491	0.0859	-0.0082	4.2707	0.0074	1.91E+03	-4.03E+05	7.1574
ZnP	539	0.0764	-0.0022	11.8841	0.0058	1.44E+03	-4.36E+05	11.6646
Nickel	614	0.0399	-0.005	9.6108	0.0016	5.29E+02	-5.21E+05	11.5277
Black Oxide	624	0.1819	-0.0019	3.4225	0.0331	5.51E+03	-3.06E+05	4.9911

Table 41: Statistical parameters of IMF 5 at 300 rpm

Coating	*HV*	*RMS*	*Skewness*	*Kurtosis*	*Variance*	*Shannon Entropy*	*Log Energy*	*Crest Factor*
Silver	192	0.0865	-0.0622	6.9086	0.0075	1.79E+03	-4.18E+05	7.8006
Copper	491	0.1436	-0.0059	4.9765	0.0206	3.85E+03	-3.42E+05	6.7712
ZnP	539	0.0545	0.0793	4.1068	0.003	9.40E+02	-4.62E+05	6.4678
Nickel	614	0.0501	-0.0177	5.3196	0.0025	7.89E+02	-4.87E+05	5.71
Black Oxide	624	0.1396	0.0132	3.117	0.0195	3.98E+03	-3.35E+05	4.514

Table 42: Statistical parameters of IMF 6 at 300 rpm

Coating	*HV*	*RMS*	*Skewness*	*Kurtosis*	*Variance*	*Shannon entropy*	*Log Energy*	*Crest Factor*
Silver	192	0.4908	-0.1571	3.2507	0.0013	2.18E+04	-9.18E+04	1.2719
Copper	491	0.3845	-0.0934	3.4511	0.0018	1.79E+04	-1.24E+05	1.4332
ZnP	539	0.4586	0.1143	2.7605	0.002	2.07E+04	-1.01E+05	1.34
Nickel	614	0.3371	0.027	3.0426	0.0007	1.57E+04	-1.40E+05	1.3129
Black Oxide	624	0.3671	0.0053	3.1491	0.0026	1.70E+04	-1.31E+05	1.617

Table 43: Statistical parameters of IMF 1 at 600 rpm

Coating	*HV*	*RMS*	*Skewness*	*Kurtosis*	*Variance*	*Shannon Entropy*	*Log Energy*	*Crest Factor*
Silver	192	0.5635	-0.0031	63.73	0.3175	-3.07E+04	-2.44E+05	21.6952
Copper	491	0.6907	-0.001	16.3892	0.477	-2.38E+04	-1.63E+05	14.5551
ZnP	539	0.4895	-0.0011	23.8247	0.2396	-9.15E+03	-2.39E+05	14.1663
Nickel	614	0.0572	-0.003	16.791	0.0033	9.17E+02	-4.74E+05	17.4657
Black Oxide	624	0.3346	-0.0008	3.1906	0.1119	1.02E+04	-2.23E+05	5.2739

Table 44: Statistical parameters of IMF 2 at 600 rpm

Coating	*HV*	*RMS*	*Skewness*	*Kurtosis*	*Variance*	*Shannon Entropy*	*Log Energy*	*Crest Factor*
Silver	192	0.824	-0.0084	13.7681	0.679	-5.44E+04	-1.59E+05	9.7533
Copper	491	0.6793	-0.0015	5.321	0.4615	-6.24E+03	-1.45E+05	6.868
ZnP	539	0.3696	0.0018	8.9878	0.1366	6.23E+03	-2.38E+05	10.3832
Nickel	614	0.0692	0.001	16.192	0.0048	1.19E+03	-4.58E+05	15.2598
Black Oxide	624	0.2952	0.0004	3.1938	0.0871	9.36E+03	-2.40E+05	4.5429

Table 45: Statistical parameters of IMF 3 at 600 rpm

Coating	*HV*	*RMS*	*Skewness*	*Kurtosis*	*Variance*	*Shannon Entropy*	*Log Energy*	*Crest Factor*
Silver	192	0.7028	0.0062	14.6203	0.494	-2.75E+04	-1.72E+05	10.8552
Copper	491	0.5875	-0.0075	4.4207	0.3452	3.47E+03	-1.60E+05	7.1354
ZnP	539	0.8865	-0.0002	7.3241	0.7859	-4.72E+04	-1.21E+05	8.4017
Nickel	614	0.0912	-0.0034	10.6744	0.0083	1.85E+03	-4.20E+05	14.4297
Black Oxide	624	0.3531	0.003	3.3901	0.1247	1.03E+04	-2.18E+05	4.6307

Table 46: Statistical parameters of IMF 4 at 600 rpm

Coating	*HV*	*RMS*	*Skewness*	*Kurtosis*	*Variance*	*Shannon Entropy*	*Log Energy*	*Crest Factor*
Silver	192	0.5749	-0.0032	5.7985	0.3305	1.01E+03	-1.72E+05	7.7872
Copper	491	0.285	-0.0051	3.9663	0.0812	8.49E+03	-2.51E+05	5.8306
ZnP	539	0.8598	-0.0017	5.8483	0.7393	-3.43E+04	-1.18E+05	7.8138
Nickel	614	0.1072	0.0047	6.7441	0.0115	2.47E+03	-3.89E+05	9.4908
Black Oxide	624	0.6349	0.0008	3.4052	0.4031	2.56E+03	-1.46E+05	4.8794

Table 47: Statistical parameters of IMF 5 at 600 rpm

Coating	*HV*	*RMS*	*Skewness*	*Kurtosis*	*Variance*	*Shannon Entropy*	*Log Energy*	*Crest Factor*
Silver	192	0.4098	-0.0065	4.6196	0.1679	8.91E+03	-2.09E+05	6.4683
Copper	491	0.3645	-0.0092	3.7827	0.1329	1.00E+04	-2.17E+05	6.1077
ZnP	539	0.5028	-0.0093	5.359	0.2528	5.73E+03	-1.88E+05	9.0597
Nickel	614	0.1282	-0.0173	3.7566	0.0164	3.42E+03	-3.54E+05	5.4057
Black Oxide	624	0.686	-0.0002	3.1002	0.4706	9.06E+01	-1.31E+05	4.3666

Table 48: Statistical parameters of IMF 6 at 600 rpm

Coating	*HV*	*RMS*	*Skewness*	*Kurtosis*	*Variance*	*Shannon Entropy*	*Log Energy*	*Crest Factor*
Silver	192	0.4554	-0.0248	3.2999	0.0093	1.97E+04	-1.07E+05	1.8395
Copper	491	0.3922	0.041	3.311	0.0043	1.79E+04	-1.24E+05	1.7043
ZnP	539	0.4176	0.3074	5.995	0.0092	1.83E+04	-1.19E+05	3.7997
Nickel	614	0.3416	0.0689	3.1202	0.0026	1.57E+04	-1.40E+05	1.6221
Black Oxide	624	0.4594	-0.0045	3.2959	0.0081	2.00E+04	-1.05E+05	2.2225

Table 49: Statistical parameters of IMF 1 at 900 rpm

Coating	*HV*	*RMS*	*Skewness*	*Kurtosis*	*Variance*	*Shannon Entropy*	*Log Energy*	*Crest Factor*
Silver	192	1.1082	0.0012	22.7812	1.228	-1.73E+05	-1.39E+05	12.2114
Copper	491	1.0936	-0.0036	8.6869	1.1959	-1.07E+05	-9.39E+04	10.5799
ZnP	539	0.65	-0.0022	9.1436	0.4225	-9.73E+03	-1.59E+05	9.728
Nickel	614	0.1737	-0.002	21.5595	0.0302	3.62E+03	-3.47E+05	21.4151
Black Oxide	624	0.7747	0.0007	3.1807	0.6001	-9.55E+03	-1.15E+05	4.2343

Table 50: Statistical parameters of IMF 2 at 900 rpm

Coating	*HV*	*RMS*	*Skewness*	*Kurtosis*	*Variance*	*Shannon Entropy*	*Log Energy*	*Crest Factor*
Silver	192	0.7767	0.0028	4.7991	0.6033	-1.75E+04	-1.27E+05	6.4016
Copper	491	0.2772	0.004	3.5065	0.0768	8.61E+03	-2.52E+05	7.2891
ZnP	539	0.6702	0.0013	3.2507	0.4492	9.77E+02	-1.35E+05	5.8372
Nickel	614	0.1692	0.0015	18.1231	0.0286	3.52E+03	-3.54E+05	16.5515
Black Oxide	624	1.2654	0.0019	21.7436	1.6013	-2.49E+05	-1.16E+05	13.1383

Table 51: Statistical parameters of IMF 3 at 900 rpm

Coating	*HV*	*RMS*	*Skewness*	*Kurtosis*	*Variance*	*Shannon Entropy*	*Log Energy*	*Crest Factor*
Silver	192	1.6126	0.0061	6.2299	2.6005	-3.42E+05	-4.10E+04	6.3868
Copper	491	1.3851	-0.0011	3.5264	1.9184	-1.80E+05	-4.61E+04	4.798
ZnP	539	1.2262	-0.0002	3.9545	1.5036	-1.21E+05	-6.24E+04	6.2884
Nickel	614	0.2184	0.0042	9.0939	0.0477	5.29E+03	-3.09E+05	9.6058
Black Oxide	624	0.7661	0.0012	3.2004	0.5868	-8.76E+03	-1.19E+05	4.8477

Table 52: Statistical parameters of IMF 4 at 900 rpm

Coating	*HV*	*RMS*	*Skewness*	*Kurtosis*	*Variance*	*Shannon Entropy*	*Log Energy*	*Crest Factor*
Silver	192	1.1008	0.0135	4.7679	1.2118	-9.17E+04	-8.62E+04	6.5777
Copper	491	1.1888	-0.0002	3.6845	1.4132	-1.08E+05	-6.77E+04	4.6418
ZnP	539	1.466	0.0004	3.3983	2.1491	-2.17E+05	-3.93E+04	4.2566
Nickel	614	0.2145	0.0253	11.5853	0.046	4.97E+03	-3.15E+05	12.4978
Black Oxide	624	1.437	0.0013	3.1161	2.0651	-1.95E+05	-3.71E+04	4.5632

Table 53: Statistical parameters of IMF 5 at 900 rpm

Coating	*HV*	*RMS*	*Skewness*	*Kurtosis*	*Variance*	*Shannon Entropy*	*Log Energy*	*Crest Factor*
Silver	192	1.1386	-0.0061	7.067	1.2963	-1.24E+05	-9.56E+04	6.9403
Copper	491	0.6706	-0.0264	3.6641	0.4498	-1.14E+03	-1.39E+05	5.2673
ZnP	539	1.1693	-0.007	3.4682	1.3673	-9.79E+04	-6.49E+04	4.4124
Nickel	614	0.337	0.1015	5.9586	0.1136	8.76E+03	-2.34E+05	12.3622
Black Oxide	624	1.0889	0.0049	3.0211	1.1856	-6.89E+04	-7.12E+04	3.9696

Table 54: Statistical parameters of IMF 6 at 900 rpm

Coating	*HV*	*RMS*	*Skewness*	*Kurtosis*	*Variance*	*Shannon Entropy*	*Log Energy*	*Crest Factor*
Silver	192	0.5089	-0.0966	4.6351	0.0649	1.58E+04	-1.27E+05	4.1106
Copper	491	0.3911	0.1627	6.6078	0.0184	1.62E+04	-1.40E+05	5.3252
ZnP	539	0.5358	-0.0536	3.2425	0.0254	1.99E+04	-9.36E+04	2.4888
Nickel	614	0.4166	1.5007	13.0792	0.0409	1.40E+04	-1.52E+05	7.9615
Black Oxide	624	0.4198	0.0147	3.1518	0.0471	1.48E+04	-1.59E+05	4.3824

Table 55: Statistical parameters of IMF 1 at 1200 rpm

Coating	*HV*	*RMS*	*Skewness*	*Kurtosis*	*Variance*	*Shannon Entropy*	*Log Energy*	*Crest Factor*
Silver	192	0.9839	-0.0003	4.9368	0.9681	-5.70E+04	-9.51E+04	7.9734
Copper	491	1.7748	0.0085	9.7998	3.15	-4.88E+05	-3.42E+04	11.0052
ZnP	539	0.852	-0.0004	4.2549	0.7259	-2.65E+04	-1.11E+05	6.4216
Nickel	614	0.433	0.0057	12.4155	0.1875	1.29E+03	-2.39E+05	10.5572
Black Oxide	624	1.2065	0.0005	3.062	1.4556	-1.04E+05	-5.72E+04	4.4453

Table 56: **Statistical parameters of IMF 2 at 1200 rpm**

Coating	*HV*	*RMS*	*Skewness*	*Kurtosis*	*Variance*	*Shannon Entropy*	*Log Energy*	*Crest Factor*
Silver	192	1.3398	0.0143	26.8203	1.795	-3.02E+05	-3.02E+05	17.2483
Copper	491	1.0156	0.0031	4.0636	1.0314	-6.10E+04	-9.07E+04	5.9267
ZnP	539	1.0281	-0.0019	7.2462	1.0569	-8.12E+04	-1.01E+05	9.6025
Nickel	614	0.4457	0.0172	13.4801	0.1986	-1.34E+02	-2.42E+05	12.1138
Black Oxide	624	1.8366	-0.0015	3.776	3.3733	-4.46E+05	-1.07E+04	5.856

Table 57: Statistical parameters of IMF 3 at 1200 rpm

Coating	*HV*	*RMS*	*Skewness*	*Kurtosis*	*Variance*	*Shannon Entropy*	*Log Energy*	*Crest Factor*
Silver	192	1.8589	0.0034	3.7271	3.4557	-4.59E+05	-7.97E+03	5.0248
Copper	491	2.4898	-0.0008	3.6409	6.1994	-1.05E+06	3.08E+04	5.5239
ZnP	539	1.3905	-0.0002	4.0756	1.9329	-1.92E+05	-4.98E+04	6.0418
Nickel	614	0.5381	0.03	9.0811	0.2896	-1.27E+03	-1.97E+05	10.3904
Black Oxide	624	1.3036	0.0004	3.2562	1.6994	-1.41E+05	-4.96E+04	5.1265

Table 58: Statistical parameters of IMF 4 at 1200 rpm

Coating	*HV*	*RMS*	*Skewness*	*Kurtosis*	*Variance*	*Shannon Entropy*	*Log Energy*	*Crest Factor*
Silver	192	1.198	0.0037	3.5782	1.4353	-1.08E+05	-6.31E+04	5.1592
Copper	491	2.0225	-0.0004	3.8556	4.0906	-6.00E+05	-2.56E+03	4.641
ZnP	539	2.314	0.0002	3.3702	5.353	-8.50E+05	2.07E+04	4.5203
Nickel	614	0.5238	0.1122	11.8411	0.2744	-4.12E+03	-2.15E+05	11.5845
Black Oxide	624	1.9789	0.0021	3.1926	3.9162	-5.34E+05	3.80E+03	4.5121

Table 59: Statistical parameters of IMF 5 at 1200 rpm

Coating	*HV*	*RMS*	*Skewness*	*Kurtosis*	*Variance*	*Shannon Entropy*	*Log Energy*	*Crest Factor*
Silver	192	1.2332	0.0009	4.0125	1.5207	-1.25E+05	-6.21E+04	5.3837
Copper	491	0.9525	-0.0358	3.5899	0.9072	-4.27E+04	-9.51E+04	5.1184
ZnP	539	2.1308	-0.0015	3.8945	4.5329	-6.96E+05	4.28E+03	4.5484
Nickel	614	0.815	0.3335	11.2156	0.6642	-4.58E+04	-1.54E+05	11.5691
Black Oxide	624	1.3277	-0.0028	3.0424	1.7628	-1.47E+05	-4.50E+04	5.1329

Table 60: Statistical parameters of IMF 6 at 1200 rpm

Coating	*HV*	*RMS*	*Skewness*	*Kurtosis*	*Variance*	*Shannon Entropy*	*Log Energy*	*Crest Factor*
Silver	192	0.5027	0.1068	4.411	0.058	1.60E+04	-1.29E+05	6.6959
Copper	491	0.4878	-0.0612	3.3297	0.0618	1.56E+04	-1.37E+05	3.7485
ZnP	539	1.7499	-0.0087	3.3997	3.0399	-3.76E+05	-1.54E+04	5.2416
Nickel	614	0.8575	2.4291	14.1941	0.6271	-6.40E+04	-1.56E+05	11.9742
Black Oxide	624	0.4698	-0.122	3.1138	0.0957	1.36E+04	-1.60E+05	4.4289

Table 61: Statistical parameters of IMF 1 at 1500 rpm

Coating	*HV*	*RMS*	*Skewness*	*Kurtosis*	*Variance*	*Shannon Entropy*	*Log Energy*	*Crest Factor*
Silver	192	0.9778	-0.0001	7.3501	0.956	-6.69E+04	-1.05E+05	8.4322
Copper	491	0.6199	0.0007	4.015	0.3843	2.97E+03	-1.47E+05	7.1016
ZnP	539	0.5076	-0.0015	4.3418	0.2577	8.15E+03	-1.74E+05	9.0807
Nickel	614	0.7083	0.0013	15.4231	0.5017	-3.04E+04	-1.77E+05	12.0114
Black Oxide	624	1.9	-0.0001	3.3097	3.61	-4.76E+05	-2.57E+03	4.7725

Table 62: Statistical parameters of IMF 2 at 1500 rpm

Coating	*HV*	*RMS*	*Skewness*	*Kurtosis*	*Variance*	*Shannon Entropy*	*Log Energy*	*Crest Factor*
Silver	192	1.0875	0.0034	8.3551	1.1827	-1.12E+05	-1.07E+05	9.9914
Copper	491	0.8957	-0.0014	3.1598	0.8022	-2.69E+04	-9.59E+04	5.5265
ZnP	539	0.8923	0.0054	19.3354	0.7963	-8.52E+04	-1.56E+05	10.5387
Nickel	614	0.7251	0.01	6.57	0.5257	-1.88E+04	-1.56E+05	6.7257
Black Oxide	624	2.8276	-0.0012	3.4671	7.9954	-1.47E+06	4.71E+04	5.8121

Table 63: Statistical parameters of IMF 3 at 1500 rpm

Coating	*HV*	*RMS*	*Skewness*	*Kurtosis*	*Variance*	*Shannon Entropy*	*Log Energy*	*Crest Factor*
Silver	192	1.4462	0.0003	8.5996	2.0916	-2.84E+05	-7.87E+04	8.6056
Copper	491	0.7612	0.0008	3.6447	0.5795	-1.05E+04	-1.23E+05	5.3458
ZnP	539	1.0191	0	15.6397	1.0387	-1.18E+05	-1.35E+05	12.5102
Nickel	614	0.8077	0.0022	5.735	0.6524	-2.73E+04	-1.31E+05	7.7781
Black Oxide	624	2.3186	0.0008	3.6212	5.3759	-8.54E+05	2.21E+04	7.2312

Table 64: Statistical parameters of IMF 4 at 1500 rpm

Coating	*HV*	*RMS*	*Skewness*	*Kurtosis*	*Variance*	*Shannon Entropy*	*Log Energy*	*Crest Factor*
Silver	192	0.7315	0.0003	8.4006	0.535	-2.09E+04	-1.48E+05	10.8105
Copper	491	0.5902	-0.0203	4.3166	0.3484	4.24E+03	-1.56E+05	9.7947
ZnP	539	0.5209	-0.0035	6.2872	0.2713	4.09E+03	-1.82E+05	8.272
Nickel	614	0.6756	0	10.3079	0.4565	-1.89E+04	-1.76E+05	9.5747
Black Oxide	624	1.8171	0.0089	3.3125	3.3018	-4.19E+05	-8.96E+03	4.6152

Table 65: Statistical parameters of IMF 5 at 1500 rpm

Coating	*HV*	*RMS*	*Skewness*	*Kurtosis*	*Variance*	*Shannon Entropy*	*Log Energy*	*Crest Factor*
Silver	192	1.1487	-0.0027	4.2314	1.3196	-1.03E+05	-7.85E+04	5.2013
Copper	491	0.8921	-0.0096	3.9992	0.7958	-3.32E+04	-1.06E+05	5.5059
ZnP	539	0.7283	0.0037	3.6869	0.5305	-7.22E+03	-1.30E+05	5.0813
Nickel	614	0.7406	0.0275	3.7096	0.5485	-8.60E+03	-1.28E+05	5.7351
Black Oxide	624	1.4557	-0.0056	3.0946	2.1176	-2.02E+05	-3.32E+04	5.5974

Table 66: Statistical parameters of IMF 6 at 1500 rpm

Coating	*HV*	*RMS*	*Skewness*	*Kurtosis*	*Variance*	*Shannon Entropy*	*Log Energy*	*Crest Factor*
Silver	192	0.5553	0.0604	3.5011	0.1423	1.12E+04	-1.43E+05	4.2028
Copper	491	0.555	-0.1102	2.8872	0.0464	1.80E+04	-1.02E+05	2.2395
ZnP	539	0.5251	-0.1644	3.1573	0.0594	1.66E+04	-1.21E+05	3.1858
Nickel	614	0.5556	0.1939	3.2425	0.1262	1.14E+04	-1.46E+05	5.8755
Black Oxide	624	0.8736	-0.0182	3.1412	0.7526	-2.33E+04	-9.96E+04	4.5335

Literature suggested that effect of hardness can be seen in RMS value of vibration signal [240]. As per the findings, higher the hardness, greater is the RMS value. However, no such behavior has been observed after calculating statistical values of acquired vibration signals. Later, statistical values obtained after decomposing the signal using VMD were compared in reference to hardness. Even after implementation of EMD, VMD and WPT on vibration signal, no significant trend has been obtained in relation to hardness based on statistical analysis of decomposed signal. Therefore, it can be said that the information in the vibration signal corresponding to hardness of bearing surface is challenging to extract with the given techniques. However, it is obvious that bearing balls after striking with surfaces of different hardness will generate unique frequencies. So, based on identification of relevant frequency bands corresponds to hardness of the surface, it would be possible to estimate the hardness. Though, encouraging results are not obtained with EMD, WPT and VMD. But still there is a possibility to identify frequency bands corresponding to hardness level with some other vibration signal analysis technique.

6.4.3 Study of variation in statistical parameters in reference to grain size

Following same approach as discussed in previous cases, the obtained statistical parameter values of acquired vibration signals are arranged as per the ascending order of grain size of bearing coating as shown in Table 67 to Table 71 for all five speeds.

Table 67: Calculated statistical parameters of acquired vibration signal at 300 rpm

Coating	*GS (nm)*	*RMS*	*Skewness*	*Kurtosis*	*Variance*	*Shannon Entropy*	*Log Energy*	*Crest Factor*
Nickel	22.42	0.3622	0.2099	16.9047	0.0105	1.58E+04	-1.41E+05	7.5891
ZnP	24.16	0.5539	-0.0604	4.7608	0.0759	1.55E+04	-1.16E+05	5.4113
Copper	24.92	0.5303	0.0212	24.0533	0.1352	9.44E+03	-1.50E+05	16.9466
Silver	26.8	0.6030	0.4346	42.8313	0.1241	8.18E+03	-1.09E+05	13.6759
Black Oxide	78.48	0.5062	0.0157	3.5156	0.1241	1.21E+04	-1.56E+05	5.3841

Table 68: Calculated statistical parameters of acquired vibration signal at 600 rpm

Coating	*GS (nm)*	*RMS*	*Skewness*	*Kurtosis*	*Variance*	*Shannon Entropy*	*Log Energy*	*Crest Factor*
Nickel	22.42	0.4543	0.1271	6.8154	0.0843	1.28E+04	-1.59E+05	7.3244
ZnP	24.16	1.6964	0.0712	7.6801	2.7124	-3.98E+05	-3.12E+04	11.8225
Copper	24.92	0.5785	-0.0464	3.8190	0.1429	1.12E+04	-1.34E+05	5.2815
Silver	26.8	0.6039	0.0526	15.2910	0.2197	3.22E+03	-1.44E+05	12.8050
Black Oxide	78.48	1.9627	0.0400	3.5348	3.7290	-5.37E+05	-2.93E+03	4.9784

Table 69: Calculated statistical parameters of acquired vibration signal at 900 rpm

Coating	*GS (nm)*	*RMS*	*Skewness*	*Kurtosis*	*Variance*	*Shannon Entropy*	*Log Energy*	*Crest Factor*
Nickel	22.42	0.6878	0.0661	6.4600	0.3594	-4.90E+03	-1.36E+05	8.5603
ZnP	24.16	1.3640	0.5979	31.6941	1.6630	-2.97E+05	-8.63E+04	17.7376
Copper	24.92	0.8759	-0.0206	3.6320	0.5609	-2.32E+04	-9.76E+04	6.4620
Silver	26.8	1.0419	-0.0032	6.4559	0.9125	-7.11E+04	-8.52E+04	9.3617
Black Oxide	78.48	2.1142	0.0499	3.1541	4.3430	-6.46E+05	1.22E+04	5.1794

Table 70: Calculated statistical parameters of acquired vibration signal at 1200 rpm

Coating	*GS (nm)*	*RMS*	*Skewness*	*Kurtosis*	*Variance*	*Shannon Entropy*	*Log Energy*	*Crest Factor*
Nickel	22.42	0.9157	0.0746	6.8410	0.7158	-4.41E+04	-1.05E+05	9.5801
ZnP	24.16	1.8629	0.2448	19.3549	3.2666	-6.47E+05	-4.42E+04	13.4397
Copper	24.92	1.3137	-0.0104	3.5016	1.5141	-1.45E+05	-4.80E+04	6.5199
Silver	26.8	1.6567	-0.0031	8.0532	2.5606	-3.75E+05	-3.60E+04	11.6506
Black Oxide	78.48	3.3363	0.0890	3.2619	11.0010	-2.27E+06	7.02E+04	5.0021

Table 71: Calculated statistical parameters of acquired vibration signal at 1500 rpm

Coating	*GS (nm)*	*RMS*	*Skewness*	*Kurtosis*	*Variance*	*Shannon Entropy*	*Log Energy*	*Crest Factor*
Nickel	22.42	1.7112	0.0068	7.3779	2.7967	-4.00E+05	-2.98E+04	12.9099
ZnP	24.16	1.9888	0.0469	13.8614	3.7372	-7.07E+05	-2.39E+04	12.2110
Copper	24.92	1.9870	0.0133	3.4406	3.6855	-5.44E+05	3.57E+03	5.9436
Silver	26.8	2.7803	-0.0217	8.4975	7.5545	-1.63E+06	2.14E+04	10.1144
Black Oxide	78.48	4.4616	0.0181	3.5697	19.7852	-4.84E+06	1.06E+05	6.8683

From these results, it is clear that no statistical parameter is showing any trend in reference to grain size. Therefore, in this case also, VMD must be applied which has shown significant results in case of surface roughness. So, after decomposing the signals into six levels using VMD, same statistical values have been calculated again. From these results, it has been observed that considerable trend has been obtained at different speeds in different IMFs. Only the tables of responded IMFs have been presented and discussed further.

Table 72: Calculated statistical parameters of IMF 3 at 300 rpm

Coating	*GS (nm)*	*RMS*	*Skewness*	*Kurtosis*	*Variance*	*Shannon Entropy*	*Log Energy*	*Crest Factor*
Nickel	22.42	0.029	0.0078	14.0081	0.0008	3.08E+02	-5.63E+05	13.1508
ZnP	24.16	0.054	-0.0063	23.4947	0.0029	8.31E+02	-4.78E+05	18.1938
Copper	24.92	0.1488	0.0006	8.5246	0.0222	3.91E+03	-3.38E+05	11.9742
Silver	26.8	0.1543	0.0027	36.5897	0.0238	2.49E+03	-3.83E+05	17.7908
Black Oxide	78.48	0.1577	0.0008	4.2258	0.0249	4.56E+03	-3.22E+05	8.9797

Table 73: Calculated statistical parameters of IMF 4 at 300 rpm

Coating	*GS (nm)*	*RMS*	*Skewness*	*Kurtosis*	*Variance*	*Shannon Entropy*	*Log Energy*	*Crest Factor*
Nickel	22.42	0.0399	-0.005	9.6108	0.0016	5.29E+02	-5.21E+05	11.5277
ZnP	24.16	0.0764	-0.0022	11.8841	0.0058	1.44E+03	-4.36E+05	11.6646
Copper	24.92	0.0859	-0.0082	4.2707	0.0074	1.91E+03	-4.03E+05	7.1574
Silver	26.8	0.1466	0.0008	14.6782	0.0215	3.20E+03	-3.62E+05	10.6533
Black Oxide	78.48	0.1819	-0.0019	3.4225	0.0331	5.51E+03	-3.06E+05	4.9911

From these tables, it can be interpreted that RMS i.e., power content of the signal is closely associated with the grain size of the surface. At all speeds, RMS has shown similar rising trend with the increase in grain diameter except few minor exceptions. At 300 rpm, in IMF 3 and 4, both RMS and variance has shown similar rising trend with the rise in grain size as shown in Table 72 and Table 73. Moreover, in IMF 4, along with RMS and variance, randomness level has also shown increasing trend along with variation in grain size. However, in same IMF 4, log energy continued to decline with the change in coating as shown in Table 73. It shows that bigger grains result in

generation of high-power vibration signals with more randomness and enhanced deviations from the mean value. In order to select best parameter among RMS, variance, Shannon entropy and log energy, chain index has been calculated based on the percentage variation of the values with change in coating. Later, average of these chain index has been taken to better evaluate the variation of statistical values with the increase in grain size.

Table 74: Responded statistical parameters at 300 RPM in IMF 3 with its chain index

Coating	*GS (nm)*	*RMS*	*Chain index*	*Variance*	*Chain index*
Nickel	22.42	0.029		0.0008	
ZnP	24.16	0.054	86.2069	0.0029	262.5
Copper	24.92	0.1488	175.5556	0.0222	665.5172
Silver	26.8	0.1543	3.6962	0.0238	7.2072
Black Oxide	78.48	0.1577	2.2035	0.0249	4.6218
Average chain index			66.91	--	234.96

Table 75: Responded statistical parameters at 300 RPM in IMF 4 with its chain index

Coating	*GS (nm)*	*RMS*	*Chain index*	*Variance*	*Chain index*	*Shannon entropy*	*Chain index*	*Log Energy*	*Chain index*
Nickel	22.42	0.0399		0.0016		5.29E+02		-5.21E+05	
ZnP	24.16	0.0764	91.478	0.0058	262.5	1.43E+03	171.21	-4.36E+05	-16.26
Copper	24.92	0.0859	12.434	0.0074	27.58	1.90E+03	32.78	-4.03E+05	-7.65
Silver	26.8	0.1466	70.663	0.0215	190.54	3.20E+03	67.70	-3.62E+05	-10.15
Black Oxide	78.48	0.1819	24.079	0.0331	53.95	5.51E+03	72.31	-3.05E+05	-15.62
Average chain index			49.66	--	133.64	--	86.00	--	-49.69

From Table 74 and Table 75, it is obvious that at 300 rpm, variance responds much stronger than RMS, Shannon entropy and log energy with the variation in grain size. Therefore, variance appears to be most relevant statistical parameter in reference to the grain size of the bearing coating at low speed. However, after comparing results obtained from both IMF 3 and 4, chain index of variance in IMF 3 is more than IMF 4, so it is better to select IMF 3 based on the higher value of chain index. On the other hand, IMF 4 is best suited to define the variation in grain size if decision is based on

number of parameters responded in a particular frequency band. As in IMF 4, four parameters have responded as compared to two parameters of IMF 3. Therefore, for future work, it is left up to the researcher that in case to go for stronger statistical relationship with grain diameter variation, IMF 3 can be chosen. Contrary, to obtain variation in more than one statistical parameter, IMF 4 can be selected. In both the cases (IMF 3 and 4), variance appears to be most relevant parameter with grain size variation based on chain indexing.

Table 76: Calculated statistical parameters of IMF 6 at 600 rpm

Coating	*GS (nm)*	*RMS*	*Skewness*	*Kurtosis*	*Variance*	*Shannon Entropy*	*Log Energy*	*Crest Factor*
Nickel	22.42	0.3416	0.0689	3.1202	0.0026	1.57E+04	-1.40E+05	1.6221
ZnP	24.16	0.4176	0.3074	5.995	0.0092	1.83E+04	-1.19E+05	3.7997
Copper	24.92	0.3922	0.041	3.311	0.0043	1.79E+04	-1.24E+05	1.7043
Silver	26.8	0.4554	-0.0248	3.2999	0.0093	1.97E+04	-1.07E+05	1.8395
Black Oxide	78.48	0.4594	-0.0045	3.2959	0.0081	2.00E+04	-1.05E+05	2.2225

Table 77: Responded statistical parameters at 600 RPM in IMF 6 with its chain index

Coating	*GS (nm)*	*RMS*	*Chain index*
Nickel	22.42	0.3416	
ZnP	24.16	0.4176	22.24
Copper	24.92	0.3922	-6.08
Silver	26.8	0.4554	16.11
Black Oxide	78.48	0.4594	0.87
Average chain index			8.28

After decomposing vibration signal taken at 600 rpm into six levels, only in IMF 6, RMS has exhibited somewhat rising trend with the increase in grain size as shown in Table 76. However, RMS value dipped while switching coating from zinc phosphate to copper as shown in Table 77. Therefore, at 600 rpm, overall, there is no such statistical parameter found which continued to show rising trend with the increase in grain diameter. The reason behind the same could be overlapping of frequency bands corresponding to grain size with other common frequencies present in the signal at the

given speed. The given VMD decomposition technique may not be able to differentiate the relevant frequency band at 600 rpm.

Table 78: Calculated statistical parameters of IMF 3 at 900 rpm

Coating	*GS (nm)*	*RMS*	*Skewness*	*Kurtosis*	*Variance*	*Shannon Entropy*	*Log Energy*	*Crest Factor*
Nickel	22.42	0.2184	0.0042	9.0939	0.0477	5.29E+03	-3.09E+05	9.6058
ZnP	24.16	1.2262	-0.0002	3.9545	1.5036	-1.21E+05	-6.24E+04	6.2884
Copper	24.92	1.3851	-0.0011	3.5264	1.9184	-1.80E+05	-4.61E+04	4.798
Silver	26.8	1.6126	0.0061	6.2299	2.6005	-3.42E+05	-4.10E+04	6.3868
Black Oxide	78.48	0.7661	0.0012	3.2004	0.5868	-8.76E+03	-1.19E+05	4.8477

Table 79: Responded statistical parameters at 900 RPM in IMF 3 with its chain index

Coating	*GS (nm)*	*RMS*	*Chain index*	*Variance*	*Chain index*
Nickel	22.42	0.2184		0.0477	
ZnP	24.16	1.2262	461.44	1.5036	3052.20
Copper	24.92	1.3851	12.95	1.9184	27.59
Silver	26.8	1.6126	16.42	2.6005	35.56
Black Oxide	78.48	0.7661	-52.49	0.5868	-77.44
Average chain index			109.58	--	759.48

From Table 78 and Table 79 it is obvious that at 900 rpm, both RMS and variance have responded considerably to the variation in grain size. However, while switching from grain size of 22.42 nm to 24.16 nm, there is huge rise in the values of RMS and variance. RMS has shown growth of 461.44% whereas variance has depicted enormous growth of 3052.2% within the grain size variation of 1.74 nm. Although, beyond grain diameter of 24.16, both parameters continued to show rising trend with increasing grain size but overall rate of increase is less than 17% in RMS and less than 36% in variance as per the chain indexing. Another important point to be noted that beyond grain size of silver, i.e., 26.8 nm both parameters discontinued to exhibit rising trend. Contrary, both these parameters depicted downward trend up to grain size of 78.48, i.e., of black oxide

coating. In all the cases, variance continued to be a dominant parameter than RMS with grain size variation. From nickel to silver coating, i.e., for grain size variation of 19.53% (22.42 to 26.8 nm), RMS has shown rise of 163.8% followed by fall of 52% for grain size variation of 192.83% (26.8 to 78.48 nm). Similarly, variance exhibited rise of 1083% for grain size variation of 19.53% (22.42 to 26.8 nm) followed by dip of 77.44% for grain size change of 192.83% (26.8 to 78.48 nm) based on the chain indexing. Therefore, like 600 rpm, at 900 rpm also, there is no statistical parameter found which can depict continuous increasing trend with the rise in grain size.

Table 80: Calculated statistical parameters of IMF 2 at 1200 rpm

Coating	*GS (nm)*	*RMS*	*Skewness*	*Kurtosis*	*Variance*	*Shannon Entropy*	*Log Energy*	*Crest Factor*
Nickel	22.42	0.4457	0.0172	13.4801	0.1986	-1.34E+02	-2.42E+05	12.1138
ZnP	24.16	1.0281	-0.0019	7.2462	1.0569	-8.12E+04	-1.01E+05	9.6025
Copper	24.92	1.0156	0.0031	4.0636	1.0314	-6.10E+04	-9.07E+04	5.9267
Silver	26.8	1.3398	0.0143	26.8203	1.795	-3.02E+05	-3.02E+05	17.2483
Black Oxide	78.48	1.8366	-0.0015	3.776	3.3733	-4.46E+05	-1.07E+04	5.856

Table 81: Responded statistical parameters at 1200 RPM in IMF 2 with its chain index

Coating	*GS (nm)*	*RMS*	*Chain index*	*Shannon entropy*	*Chain index*
Nickel	22.42	0.4457		-1.34E+02	
ZnP	24.16	1.0281	130.67	-8.12E+04	60315.71
Copper	24.92	1.0156	-1.22	-6.10E+04	-24.86
Silver	26.8	1.3398	31.92	-3.02E+05	395.38
Black Oxide	78.48	1.8366	37.08	-4.46E+05	47.34
Average chain index			49.61	--	15183.39

At 1200 rpm, again RMS and Shannon entropy have shown inconsistency in trend with the change in grain size as shown in Table 81. In this case, initially RMS has shown a significant increase of 130.67% up to the grain size of 24.16 nm. From 24.16 nm to 24.92 nm, RMS value dips slightly around 1%. Later, up to the grain size of 78.48 nm, RMS again depicted rising trend. Similarly, Shannon is also showing rising trend up to the grain size of 24.16 nm, however excessive rise of 60315.71% has been identified.

Further, variance also dipped by 24.86% up to grain size of 24.92 nm followed by significant rise of 395.38% till grain size of 26.8 nm. Then, again rise of 47.34% in Shannon has been noted till grain diameter of 78.48 nm. Due to this fluctuating behavior of both responded parameters, RMS, and Shannon entropy, it is difficult to associate any statistical parameter with grain size variation at 1200 rpm also.

Table 82: Calculated statistical parameters of IMF 2 at 1500 rpm

Coating	*GS (nm)*	*RMS*	*Skewness*	*Kurtosis*	*Variance*	*Shannon Entropy*	*Log Energy*	*Crest Factor*
Nickel	22.42	0.7251	0.01	6.57	0.5257	-1.88E+04	-1.56E+05	6.7257
ZnP	24.16	0.8923	0.0054	19.3354	0.7963	-8.52E+04	-1.56E+05	10.5387
Copper	24.92	0.8957	-0.0014	3.1598	0.8022	-2.69E+04	-9.59E+04	5.5265
Silver	26.8	1.0875	0.0034	8.3551	1.1827	-1.12E+05	-1.07E+05	9.9914
Black Oxide	78.48	2.8276	-0.0012	3.4671	7.9954	-1.47E+06	4.71E+04	5.8121

Table 83: Responded statistical parameters at 1500 RPM in IMF 2 with its chain index

Coating	*GS (nm)*	*RMS*	*Chain index*
Nickel	22.42	0.7251	
ZnP	24.16	0.8923	23.05
Copper	24.92	0.8957	0.38
Silver	26.8	1.0875	21.41
Black Oxide	78.48	2.8276	160.00
Average chain index			**51.22**

At 1500 rpm, only RMS has shown consistent rising trend with the increase in grain size as shown in Table 83. Unlike, 600, 900 and 1200 rpm where responded parameters has shown downward trend while changing grain size, there is no downfall found in this case. However, there is significant fluctuation in rate of change of RMS while switching grain size. Initially, RMS has shown percentage variation of 23.05% for the grain size change from 22.42 nm to 24.16 nm (Nickel to ZnP). Further, up to 24.92 nm (Copper), there is very small rise of only 0.38% has been noted. Later, there is revival

in percentage variation and rate of change again touched to 21.41% up to grain diameter of 26.8 nm (Silver). Finally, a sharp rise of 160% has been achieved for the change of grain size from 26.8 to 78.48 % (Black Oxide). Based on the chain indexing, RMS has depicted growth of 51.22% for the grain size growth of 250% (Nickel to Black oxide). Therefore, at 1500 rpm, RMS found to be most reliable parameter for the grain size variation in the surface of bearing element.

Table 84: Responded IMF level, frequency bands, statistical parameters along with average chain index at all speeds

S. No	*RPM*	*IMF level shown response*	*Approximate Frequencies Band (Hz)*	*Responding statistical parameters*	*Average chain index value*
1	300	3 & 4	1410-2570 & 801-1630	RMS, Variance & RMS, Variance, SE	66.91, 234.96 & 49.66, 133.64, 86
2	600	6	0.00507 - 574	Inconsistent trend	NA
3	900	3	1370 – 3090	Inconsistent trend	NA
4	1200	2	2700 - 4820	Inconsistent trend	NA
5	1500	2	2870 - 4790	RMS	51.22

It is also important to note that, though encouraging results were obtained at 300 and 1500 rpm, it is not obvious to obtain results at all speeds between this range. Because at different speeds, range of frequency bands corresponding to particular surface property also varies. As, referring to frequency bands of responded IMFs as shown in Table 84, it is observed that with the rise in speed, frequency bands responsive to variation in grain size are shifting towards higher side. After shifting, it may get overlapped with other common frequencies present in the signal.

6.4.4 Study of variation in statistical parameters in reference to wear resistance

The coated bearings used in this study are also having different levels of wear resistance like other mentioned properties. The evaluated statistical values of the acquired vibration signals of different coated bearing are re-arranged as per the ascending order of the wear rate, opposite to wear resistance. As mentioned earlier in Chapter 5 that experimentally, the value of wear rate is obtained instead of wear resistance. Therefore, in the tables, wear rate is mentioned in descending order, to get wear resistance in increasing order as both are opposite to each other. In reference to wear rate, the results are presented next in tabular form from Table 85 to Table 89.

Table 85: Statistical parameters of original signal at 300 rpm

Coating	*Wear rate*	*RMS*	*Skewness*	*Kurtosis*	*Variance*	*Shannon Entropy*	*Log Energy*	*Crest Factor*
Black Oxide	9.94E-04	0.5062	0.0156	3.5156	0.1240	1.22E+04	-1.57E+05	5.3841
Silver	9.69E-04	0.6030	0.4346	42.8313	0.1241	8.19E+03	-1.10E+05	13.6759
Copper	3.78E-04	0.5303	0.0212	24.0533	0.1351	9.44E+03	-1.50E+05	16.9466
ZnP	2.15E-04	0.5538	-0.0604	4.76077	0.0759	1.55E+04	-1.16E+05	5.4112
Nickel	1.23E-04	0.3622	0.2099	16.9047	0.0105	1.58E+04	-1.41E+05	7.5891

Table 86: Statistical parameters of original signal at 600 rpm

Coating	*Wear rate*	*RMS*	*Skewness*	*Kurtosis*	*Variance*	*Shannon Entropy*	*Log Energy*	*Crest Factor*
Black Oxide	9.94E-04	1.9626	0.0400	3.5347	3.7289	-5.37E+05	-2.93E+03	4.9783
Silver	9.69E-04	0.6039	0.0525	15.291	0.2196	3.22E+03	-1.44E+05	12.8049
Copper	3.78E-04	0.5785	-0.0464	3.8189	0.1429	1.12E+04	-1.34E+05	5.2814
ZnP	2.15E-04	1.6963	0.0711	7.6801	2.7123	-3.98E+05	-3.12E+04	11.8225
Nickel	1.23E-04	0.4542	0.1270	6.8153	0.0843	1.28E+04	-1.60E+05	7.3243

Table 87: Statistical parameters of original signal at 900 rpm

Coating	*Wear rate*	*RMS*	*Skewness*	*Kurtosis*	*Variance*	*Shannon Entropy*	*Log Energy*	*Crest Factor*
Black Oxide	9.94E-04	2.1141	0.0498	3.1541	4.3430	-6.46E+05	1.22E+04	5.1793
Silver	9.69E-04	1.0418	-0.0032	6.4559	0.9125	-7.12E+04	-8.52E+04	9.3617
Copper	3.78E-04	0.8758	-0.0206	3.6319	0.5609	-2.32E+04	-9.76E+04	6.4620
ZnP	2.15E-04	1.3640	0.5979	31.6941	1.6630	-2.98E+05	-8.64E+04	17.7376
Nickel	1.23E-04	0.6878	0.0660	6.4599	0.3593	-4.90E+03	-1.36E+05	8.5603

Table 88: Statistical parameters of original signal at 1200 rpm

Coating	*Wear rate*	*RMS*	*Skewness*	*Kurtosis*	*Variance*	*Shannon Entropy*	*Log Energy*	*Crest Factor*
Black Oxide	9.94E-04	3.3362	0.08897	3.2619	11.0010	-2.27E+06	7.02E+04	5.0021
Silver	9.69E-04	1.6566	-0.0030	8.0532	2.5606	-3.75E+05	-3.60E+04	11.6505
Copper	3.78E-04	1.3136	-0.0104	3.5015	1.5140	-1.45E+05	-4.80E+04	6.5199
ZnP	2.15E-04	1.8629	0.2447	19.3548	3.2665	-6.47E+05	-4.42E+04	13.4397
Nickel	1.23E-04	0.9157	0.0746	6.8409	0.7157	-4.41E+04	-1.05E+05	9.5801

Table 89: Statistical parameters of original signal at 1500 rpm

Coating	*Wear rate*	*RMS*	*Skewness*	*Kurtosis*	*Variance*	*Shannon Entropy*	*Log Energy*	*Crest Factor*
Black Oxide	9.94E-04	4.4616	0.01805	3.5697	19.7851	-4.84E+06	1.06E+05	6.8683
Silver	9.69E-04	2.7802	-0.0217	8.4974	7.5544	-1.63E+06	2.14E+04	10.1144
Copper	3.78E-04	1.9869	0.01334	3.4405	3.6854	-5.45E+05	3.57E+03	5.9435
ZnP	2.15E-04	1.9887	0.04688	13.8614	3.7372	-7.08E+05	-2.39E+04	12.2109
Nickel	1.23E-04	1.7111	0.00682	7.3778	2.7967	-4.00E+05	-2.98E+04	12.9098

From tables, it is clear that not even a single statistical parameter has shown any trend in relevance to variation in wear resistance. Therefore, to explore the signal in detail, it has been decomposed into six levels using VMD technique and same statistical values have been calculated again for all six parts of the signal at all speeds. The results of the responded IMFs at different speeds are presented further.

Table 90: Statistical parameters of IMF 4 at 300 rpm

Coating	*Wear rate*	*RMS*	*Skewness*	*Kurtosis*	*Variance*	*Shannon Entropy*	*Log Energy*	*Crest Factor*
Black Oxide	9.94E-04	0.1819	-0.0019	3.4225	0.0331	5.51E+03	-3.06E+05	4.9911
Silver	9.69E-04	0.1466	0.0008	14.6782	0.0215	3.20E+03	-3.62E+05	10.6533
Copper	3.78E-04	0.0859	-0.0082	4.2707	0.0074	1.91E+03	-4.03E+05	7.1574
ZnP	2.15E-04	0.0764	-0.0022	11.8841	0.0058	1.44E+03	-4.36E+05	11.6646
Nickel	1.23E-04	0.0399	-0.005	9.6108	0.0016	5.29E+02	-5.21E+05	11.5277

After decomposing the signals into six modes and calculating specified statistical parameters at all speeds, it has been observed that at 300 rpm in IMF 4, RMS, Variance, Shannon entropy and log energy have shown downfall trend consistently with the increase in wear resistance. It reflects that amplitude, dispersion, randomness and intensity of the vibration signal have been reduced with the decrease in wear rate. In order to quantify these variations, chain indexing has been done as mentioned in Table 91.

Table 91: Responded statistical parameters at 300 RPM in IMF 4 with its chain index

Coating	*Wear rate*	*RMS*	*Chain index*	*Variance*	*Chain index*	*Shannon entropy*	*Chain index*	*Log Energy*	*Chain index*
Black Oxide	9.94E-04	0.1819		0.0331		5.51E+03		-3.06E+05	
Silver	9.69E-04	0.1466	-19.40	0.0215	-35.04	3.20E+03	-41.96	-3.62E+05	18.52
Copper	3.78E-04	0.0859	-41.40	0.0074	-65.58	1.91E+03	-40.37	-4.03E+05	11.29
ZnP	2.15E-04	0.0764	-11.05	0.0058	-21.62	1.44E+03	-24.69	-4.36E+05	8.28
Nickel	1.23E-04	0.0399	-47.77	0.0016	-72.41	5.29E+02	-63.12	-5.21E+05	19.42
Average chain index			**-29.91**	**--**	**-48.66**	**--**	**-42.54**	**--**	**14.38**

According to chain indexing, it can be stated that for the wear rate variation of 87.62% (black oxide to nickel coating), average amplitude, dispersion, uncertainty, and logarithm of the energy in the data have been reduced by 29.91%, 48.66%, 42.54% and 14.38% respectively. Therefore, Variance found to be most responsive parameter to the change in wear rate at 300 rpm based on the magnitude of chain indexing.

Table 92: Statistical parameters of IMF 3 at 600 rpm

Coating	*Wear rate*	*RMS*	*Skewness*	*Kurtosis*	*Variance*	*Shannon Entropy*	*Log Energy*	*Crest Factor*
Black Oxide	9.94E-04	0.3531	0.003	3.3901	0.1247	-1.03E+04	-2.18E+05	4.6307
Silver	9.69E-04	0.7028	0.0062	14.6203	0.494	-2.75E+04	-1.72E+05	10.8552
Copper	3.78E-04	0.5875	-0.0075	4.4207	0.3452	-3.47E+04	-1.60E+05	7.1354
ZnP	2.15E-04	0.8865	-0.0002	7.3241	0.7859	-4.72E+04	-1.21E+05	8.4017
Nickel	1.23E-04	0.0912	-0.0034	10.6744	0.0083	-5.85E+04	-4.20E+05	14.4297

At 600 rpm in IMF 3, again randomness level has shown considerable response with the rise in wear rate as shown in Table 92 . Like 300 rpm, Shannon entropy has decreased consistently at 600 rpm also. To evaluate the percentage variation, chain indexing has been carried out as shown in Table 93. Based on the chain index, Shannon entropy has shown a strong reaction towards variation in wear rate. Initially for the wear rate decrement of 2.51% (black oxide to silver), Shannon entropy has shown downfall of 166.99%. Later, for the decrease of 61% in wear rate (silver to copper), randomness level has shown fall of 26.18%, which is comparatively less than last case.

Table 93: Responded statistical parameter at 600 RPM in IMF 3 with its chain index

Coating	*Wear rate*	*Shannon entropy*	*Chain index*
Black Oxide	9.94E-04	-1.03E+04	
Silver	9.69E-04	-2.75E+04	166.99
Copper	3.78E-04	-3.47E+04	26.18
ZnP	2.15E-04	-4.72E+04	36.02
Nickel	1.23E-04	-5.85E+04	23.94
Average chain index			63.28

Further, there is significant downfall of 36.02% in orderliness has been registered for the 43% reduction in wear rate (Copper to zinc phosphate). Lastly, Shannon entropy has again shown downward trend with reduction of 103.91% for 23.94% decrement in wear rate (zinc phosphate to nickel). Overall, for the wear rate variation of 87.62% (black oxide to nickel), randomness level has shown fall of 63.28%. Therefore at 600 rpm, it is to be noted that only Shannon entropy has shown a considerable and consistent downfall trend towards the decrement in wear rate, i.e., increase in wear resistance. It depicts that smoother the surface, lesser will be the wear, which further reflected with reduction in randomness of the vibration signal.

Next at 900 rpm, none of the statistical parameter has shown any response to the variation in wear resistance. For exploration, the signal has been decomposed with specified techniques, EMD, WPT and VMD. Each part of the signal has been analyzed individually using statistical parameters but no considerable trend has been obtained. The reason behind the same could be the overlapping of the frequency bands corresponding to wear rate with other dominant frequencies present in the signal. There might be other relevant techniques available to extract those frequency bands at 900 rpm which could be beyond the scope of this research work.

Table 94: Statistical parameters of IMF 4 at 1200 rpm

Coating	*Wear rate*	*RMS*	*Skewness*	*Kurtosis*	*Variance*	*Shannon Entropy*	*Log Energy*	*Crest Factor*
Black Oxide	9.94E-04	1.9789	0.0021	3.1926	3.9162	-5.34E+05	3.80E+03	4.5121
Silver	9.69E-04	1.1980	0.0037	3.5782	1.4353	-1.08E+05	-6.31E+04	5.1592
Copper	3.78E-04	2.0225	-0.0004	3.8556	4.0906	-6.00E+05	-8.56E+04	4.6410
ZnP	2.15E-04	2.3140	0.0002	3.3702	5.3530	-8.50E+05	-2.07E+05	4.5203
Nickel	1.23E-04	0.5238	0.1122	11.8411	0.2744	-4.12E+03	-2.15E+05	11.5845

Further at 1200 rpm in IMF 4, consistent downward trend has been depicted by the log energy as shown in Table 94. No other parameter has shown any trend in reference to variation in wear rate at the given speed. In terms of the percentage variation using chain index, results are presented in Table 95.

Table 95: Responded statistical parameter at 1200 RPM in IMF 4 with its chain index

Coating	*Wear rate*	*Log energy*	*Chain index*
Black Oxide	9.94E-04	3.80E+03	
Silver	9.69E-04	-6.31E+04	1760.53
Copper	3.78E-04	-8.56E+04	35.66
ZnP	2.15E-04	-2.07E+05	141.82
Nickel	1.23E-04	-2.15E+05	3.86
Average chain index			485.47

As per the results, significantly high downfall of 1760.53% in log energy has been noted corresponding to the wear rate decrement of 2.51% (black oxide to silver). Followed by decrease in log energy by 35.66% for the wear rate reduction of 61% (silver to copper). The log energy continued to decrease by 141.82% for further drop-in wear rate by 43% (copper to zinc phosphate). Lastly, for the decrease in wear rate by 3.52% (zinc phosphate to nickel), intensity of the vibration signal i.e., log energy continued to dipped by 3.86%. Overall, for the wear rate fall of 87.62% (black oxide to nickel), log of the energy has fallen by 485.47% as per the average chain indexing at 1200 rpm in IMF 4.

Table 96: Statistical parameters of IMF 1 at 1500 rpm

Coating	*Wear rate*	*RMS*	*Skewness*	*Kurtosis*	*Variance*	*Shannon Entropy*	*Log Energy*	*Crest Factor*
Black Oxide	9.94E-04	1.9	-0.0001	3.3097	3.61	-4.76E+05	-2.57E+03	4.7725
Silver	9.69E-04	0.9778	-0.0001	7.3501	0.956	-6.69E+04	-1.05E+05	8.4322
Copper	3.78E-04	0.6199	0.0007	4.015	0.3843	2.97E+03	-1.47E+05	7.1016
ZnP	2.15E-04	0.5076	-0.0015	4.3418	0.2577	8.15E+03	-1.74E+05	9.0807
Nickel	1.23E-04	0.7083	0.0013	15.4231	0.5017	-3.04E+04	-1.77E+05	12.0114

At 1500 rpm in IMF 1, only log energy has shown consistent rising trend against the variation in wear rate as shown in Table 96. To know about the percentage variation with the change in wear behavior of coating, chain indexing has been calculated as shown in Table 97.

Table 97: Responded statistical parameter at 1500 RPM in IMF 1 with its chain index

Coating	*Wear rate*	*Log energy*	*Chain index*
Black Oxide	9.94E-04	-2.57E+03	
Silver	9.69E-04	-1.05E+05	3972.15
Copper	3.78E-04	-1.47E+05	40.69
ZnP	2.15E-04	-1.74E+05	18.36
Nickel	1.23E-04	-1.77E+05	1.71
Average chain index			1008.23

Initially for the wear rate variation of 2.51% (black oxide to silver), significantly high increase of 3972.15% has been noted in the logarithmic of the signal's energy. Later, when bearing coating got changed from silver to copper (61% fall in wear rate), signal's intensity increased by 40.69%. Next, for the coating variation from copper to zinc phosphate (wear rate decrement of 43%), magnitude of the vibration signals depicted rise of 18.36%. Lastly, from zinc phosphate to nickel coating (wear rate decrease of 42.79%), log of the energy has shown rise of 1.71%. Overall, for the wear rate fall of 87.62% (black oxide to nickel), log of the energy has risen by 1008.23% as per the average chain indexing at 1500 rpm in IMF 1.

Table 98: Responded IMF level, frequency bands, statistical parameters along with average chain index at all speeds

S. No	*RPM*	*IMF level shown response*	*Approximate Frequencies Band (Hz)*	*Responding statistical parameters (SPs)*	*Average chain index value of SPs*
1	300	4	879 - 1360	RMS, Variance, SE & log energy	-29.91, -48.66, -42.54, 14.38
2	600	3	1540 - 2210	SE	63.28
3	900	--	--	None	NA
4	1200	4	1430 - 1870	Log energy	485.47
5	1500	1	4800 - 5520	Log energy	1008.23

Referring to Table 98, it is noted that at low rpm, variation in wear resistance is highlighted by low frequency events by getting response in IMF 4. With the increase in speed up to 600 rpm, responsive frequency bands shifted to higher side i.e., IMF 3. Further, there was no response obtained at 900 rpm. After reaching 1200 rpm, again response is achieved in IMF 4 but in lower frequency band as compared to 600 rpm. However, at 1500 rpm, frequency band responsive to variation in wear resistance has been noted in IMF 1, a higher frequency zone. Unlike, in case of other properties, there is no consistent trend in responsive frequency bands with the increase in speed.

6.4.5 Study of variation in statistical parameters in reference to self-lubricating level

As already discussed earlier, that there is inverse relationship exists between wear rate and self-lubricating level. So, based on the reading obtained from wear analysis, different bearing coatings can be arranged in ascending order of self-lubricating level by arranging the coating with highest wear rate first as shown in Table 99.

Table 99: Different bearing coating arranged in ascending order of self-lubricating level

Coating	*Wear rate*
Black Oxide	9.94E-04
Silver	9.69E-04
Copper	3.78E-04
ZnP	2.15E-04
Nickel	1.23E-04

However, the same approach of arranging coatings as per descending order of wear rate has been followed while analyzing wear resistance of the coating. Therefore, results obtained through statistical analysis of vibration signal in the case of wear resistance are going to be same in the given case of self-lubricating level. Hence, findings of Section 6.4.5 can be referred as it is, to obtain a correlation between self-lubricating level of coating with a suitable statistical parameter of vibration signal at different speeds.

7. Summary and Conclusions.

The goal of this research is to characterize and correlate the material properties of five different bearing coatings with respect to vibration characteristics. These properties included surface roughness, hardness, grain size, and wear resistance. Five different bearing coatings taken up in this work are: Nickel, Silver, Copper, Zinc Phosphate and Black oxide. Different coated bearings were tested at five different speeds, i.e., 300, 600, 900, 1200 and 1500 rpm and the resulting vibration signals were recorded. VMD was then used to break down the recorded signals into IMFs, each of which comprised of narrow frequency bands generated around a significant central frequency. After doing statistical analysis on the raw signal and the decomposed signal, the following conclusions can be drawn property wise, starting with surface roughness:

- Initially, simple statistical analysis of acquired vibration signals is carried out and no correlation with different levels of surface roughness was found at all the RPMs. With an exception at 1500 rpm, where RMS and Shannon entropy have shown considerable trend with average chain index of 29.11 and 98.35 respectively. It is to be noted that only at 1500 pm, effect of variation in surface roughness of mating surfaces can be analyzed by calculating RMS and SE of acquired raw vibration signal. Further, to analyze the signal more precisely and to get response at other speeds, raw signal has been decomposed into six modes using VMD and findings are discussed further after statistical analysis of all modes at different speeds.
- At 300 rpm, statistical parameters have been calculated for all the frequency bands (IMFs) using VMD but none of the statistical parameter has shown any correlation with different levels of R_a. The surface characteristics generated at low rolling speed were either very weak or the frequency band in which characteristics were coming may have overlapped with the fundamental frequencies.
- In the case of 600 RPM, statistical parameters RMS, Variance and Shannon entropy for IMF 6 decomposition level have shown inconsistent rising trend with increase in R_a. In some of the cases, the variation in the statistical parameters was even less than 2%. Therefore, none of statistical parameters can be relied on for analyzing the different levels of surface roughness at 600 RPM.

- The consistent rising trend of statistical parameters RMS, Variance and Shannon entropy for IMF 4 decomposition level is observed at 900 rpm with increase in R_a. However, randomness has shown better sensitivity to the R_a variation as minimum variation of nearly 103% and overall average of 458.18% in chain indexing.
- Variation in randomness is again found to be suitable parameter for depicting the different levels of R_a at 1200 RPM and 1500 RPM in IMF 2. The same rising trend in randomness was observed with increase in R_a. However, other parameters RMS and Variance have shown very less variation in differentiating R_a levels from 0.52 to 0.7 at 1200 RPM and opposite trend at 1500 RPM at same levels. Shannon entropy found to be an optimal parameter to detect variation in surface roughness level of the bearing surface in IMF 4 at 900 rpm and in IMF 2 at 1200 and 1500 rpm based on statistical analysis of vibration signal using VMD. Therefore, for a bearing running between 900 to 1500 RPM, it is possible to estimate its surface roughness level through vibration signature analysis.

Next, in case of hardness, it can be concluded that for thin coatings, it is challenging to identify different level of surface hardness through statistical analysis of vibration signal. No significant patterns have been observed in any of the statistical parameters related to hardness following the completion of statistical analysis on both the original and decomposed signals. The reason behind the same could be inability of EMD, VMD and WPT techniques to extract the specific frequency bands responsive to hardness of the material. Therefore, there is possibility of getting results in response to hardness also with another way to be explored yet.

Further, in case of grain size, the following inferences can be drawn after statistical analysis of the vibration signal:

- Initially, simple statistical analysis of acquired vibration signals is carried out and no correlation with different grain size has been found at all the RPMs.
- At 300 rpm, statistical parameters are calculated for all the frequency bands (IMFs) generated through VMD, RMS and Variance have shown considerable correlation with the variation in grain size in IMF 3. Additionally, RMS, Variance, Shannon

entropy and log energy depicted significant response to grain size variation. However, in IMF 3, Variance found to be more sensitive with average chain index value of 234.96 in comparison to 66.91 of RMS. Similarly in IMF 4, again variance found to be leading parameter among all four responsive parameters with average chain index value of 133.64.

- In the case of 600 RPM, statistical parameters RMS for IMF 6 decomposition level have shown inconsistent rising trend with increase in grain size. In some of the cases, the variation in the statistical parameters is even less than 1%. Therefore, none of statistical parameters can be relied on for analyzing the different grain size at 600 RPM.
- The inconsistent trend of statistical parameters RMS and variance continued at 900 rpm also as found in IMF 4 decomposition level with increase in grain diameter. However, both parameters have shown continuous rise from grain diameter of 22.42 nm (nickel) to 26.8 nm (silver) followed by sharp decline of 52.49% and 77.44% in both parameters. Therefore, none of statistical parameters can be relied on for analyzing the different grain size at 900 RPM also.
- High fluctuations in the values of responded statistical parameters RMS and Shannon entropy has been noted again at 1200 rpm also for depicting the different levels of grain size. After considerable rise of 130.67% and 60315.71% for the grain diameter variation of 22.42 nm (Nickel) to 24.16 nm (ZnP). Both parameters declined by 1.22% and 24.86% corresponding to grain size change of 24.16 nm (ZnP) to 24.92 nm (Copper). Further, significant rising trend found to be continued in both parameters while grain size changing from 24.92 nm (Copper) to 78.48 nm (Black oxide). Due to this inconsistent behavior in variations of statistical parameters, it is not advisable to rely on any parameter for analyzing the different grain size at 1200 RPM too.
- Variation in RMS was again found to be suitable parameter for depicting the different grain sizes at 1500 RPM. The same rising trend in RMS has been observed with increase in grain diameter. However, RMS has shown very less variation in differentiating grain size from 24.16 to 24.92 nm. Then up to grain size of 78.48 nm, a significant rise in RMS has been noted. Overall, RMS have depicted rise of 51.22 % based on average chain index from 22.42 nm (Nickel) to 78.8 nm (Black

Oxide). Therefore, Variance of IMF 3 found to be most optimal parameter to monitor the level of grain size of bearing surface running at 300 rpm. However, RMS in IMF 2 found to be most reliable parameter at 1500 rpm in relevance to grain size variation. Hence, grain size estimation of bearing surface is possible by analyzing its vibration signal.

Next, in case of wear resistance property of bearing coating, the following conclusions can be made after carrying out statistical analysis of the acquired vibration signatures:

- On similar note, after carrying out simple statistical analysis of acquired vibration signals, no correlation with different levels of wear resistance has been found at all the RPMs.
- At 300 rpm, statistical parameters have been calculated for all the frequency bands (IMFs) generated through VMD. RMS, Variance, Shannon entropy (SE) and log energy (LE) have shown considerable correlation with the variation in wear resistance in IMF 4. However, RMS, Variance and SE showed continuous decrement with the increase in wear resistance. Contrary, log energy depicted consistent rise at each level with the increase in wear resistance. Among decrement parameters, Variance found to be more sensitive with average chain index value of 48.66 in comparison to 42.54 of SE and 29.92 of RMS. On the other hand, increment parameter, log energy has shown average chain index value of 14.38.
- In the case of 600 RPM, statistical parameter SE for IMF 3 decomposition level have shown consistent fall with the rise in wear resistance. Therefore, SE with average chain index value of 63.28 can be relied on for analyzing the different levels of wear resistance at 600 RPM.
- At 900 rpm, no trend has been found in any of the statistical parameter with simple statistical analysis towards the change in wear resistance.

- The consistent fall in one of the statistical parameters, Log energy has been noted at 1200 rpm in IMF 4 decomposition level with increase in wear resistance. However, rate of fall is not uniform throughout. Initially, for the wear rate change of 2.51% (Black oxide to silver), log energy value has decreased sharply by 1760.53%. On the other hand, corresponding to wear rate variation of 61% (Silver

to copper), log energy has only fallen by 35.66% comparatively. Overall, LE with average chain index decrement value of 485.47 can be relied on for analyzing the different levels of wear resistance at 1200 RPM.

- Rise in the values of responded statistical parameter, log energy has been noted at 1500 rpm in IMF 1 in relevance to the different levels of wear resistance. However, percentage variation in rising trend is highly fluctuating. In response to change in wear rate by 2.51% (Black oxide to silver), huge rise of 3972.15% has been noted in log energy based on chain index value. Contrary, for the wear rate variation of 42.79% (ZnP to nickel), only 1.71% of rise has been observed in log energy as per chain indexing. Overall, log energy could be suggested as relatable parameter to variations in wear resistance at 1500 rpm with exceptionally high average chain index value of 1008.23. Therefore, it can be concluded that at 300 and 600 rpm, wear resistance variation is linked with Shannon entropy in IMF 4 and IMF 3 respectively. However, at 1200 and 1500 rpm, log energy found to be optimal responded parameter linked with wear resistance level in IMF 4 and IMF 1 respectively generated by VMD applied on acquired vibration signal of coated bearing. Hence, it is feasible to approximate the wear resistance level of bearing in running condition by analyzing its vibration signal, without the need of dismantling to evaluate its surface properties.

Lastly, in case of self-lubricating property of bearing coating, the conclusions obtained in case of wear resistance analysis are equally valid as the order of coatings are same in both cases.

Hence, it is feasible to monitor the deterioration of bearing surface in running condition based on statistical analysis of its vibration signature. As continuous degradation of the surface may lead to formation of any geometric discontinuity like pits, cracks, erosion etc. Therefore, this research work can help in predicting the remaining useful life of bearing precisely by detecting the fault at very incipient stage, thus useful in industry also to avoid unplanned downtime.

Future Scope

Though this research work is limited to bearing applications with few coatings. The same approach can also be utilized to determine deterioration of mating surfaces in other running components like gears, pulleys, or shafts. Therefore, life of the critical components of a machine can also be accurately predicted based on the statistical analysis of their vibration signature.

8. Bibliography

1. Allied Caster equipment company. (2018, February 9). How Ball Bearings Work. https://www.alliedcaster.com/how-ball-bearings-work/
2. Barden precision bearings. (2015, July 29). Bearing Failure: Causes and Cures. https://www.schaeffler.com/remotemedien/media/_shared_media/08_media_library/01_publications/barden/brochure_2/downloads_24/barden_bearing_failures_us_en.pdf
3. NSK Americas. (March 3, 2020). Technical Insight: Product and application engineering information. https://www.nskamericas.com/content/dam/nskcmsr/downloads/americas_bearing/TI%20Bearing%20Life.pdf
4. Denton vacuum (2018, June 29). Differences in Grain Size Between Deposition Methods. https://www.dentonvacuum.com/differences-grain-size-deposition-methods/
5. Figueiredo, R. B., Kawasaki, M., & Langdon, T. G. (2024). The role of grain size in achieving excellent properties in structural materials. Journal of Materials Research and Technology, 30, 3448-3462.
6. Lv, Y., Zhao, W., Zhao, Z., Li, W., & Ng, K. K. (2022). Vibration signal-based early fault prognosis: Status quo and applications. Advanced Engineering Informatics, 52, 101609.
7. Zedler, L., Hager, M. D., Schubert, U. S., Harrington, M. J., Schmitt, M., Popp, J., & Dietzek, B. (2014). Monitoring the chemistry of self-healing by vibrational spectroscopy–current state and perspectives. Materials Today, 17(2), 57-69.
8. Maximus, K., Saifulnizan, J., Ismail, A., Hisyamudin, N., Khir, M. N., Kamarul, A. K., & Awang, M. K. (2018). Hardness and wear rate of Al LM6 hollow cylinder fabricated using horizontal centrifugal casting. In Journal of Physics: Conference Series (Vol. 1049, No. 1, p. 012042). IOP Publishing.
9. India Mart Novus make. (1996, July 22). Basic Pin on Disc Wear Testing Machine with Digital Controller.

https://www.indiamart.com/proddetail/basic-pin-on-disc-wear-testing-machine-with-digital-controller-22861514830.html

10. Crouch, I. G., Cimpoeru, S. J., Li, H., & Shanmugam, D. (2017). Armour steels. In The science of armour materials (pp. 55-115). Woodhead Publishing.
11. Schaeffler Group (n.d.). High performance capacity through the use of bearing. http://www.midpointbearing.com/wp-content/uploads/2017/10/FAG-Bearing-Coatings.pdf
12. Metal Coating Processes. (n.d.). Unit 4 Metal Coating Processes. http://www.ignou.ac.in/upload/Unit-4.pdf
13. TWI Anodising. (n.d.). What is anodising. https://www.twi-global.com/technical-knowledge/faqs/faq-what-is-anodising
14. Metal supermarkets. (2016, August 9). Metal Supermarkets - Steel, Aluminium, Stainless, Hot-Rolled, Cold-Rolled, Alloy, Carbon, Galvanized, Brass, Bronze, Copper. https://www.metalsupermarkets.com/what-is-galvanizing/
15. Yli-Pentti, A. (2014). Electroplating and electroless plating.
16. What is Phosphating. (2019, January 10). Zinc Phosphating Process Details. http://www.phosphating.net/zinc-phosphating.html
17. Xie, Y., Chen, M., Xie, D., Zhong, L., & Zhang, X. (2017). A fast, low temperature zinc phosphate coating on steel accelerated by graphene oxide. Corrosion Science, 128, 1-8.
18. SKF Coatings. (2020, February 1). An introduction to Coatings. https://www.skf.com/binaries/pub12/Images/0901d19680a4e17f-18781-EN---Coating-catalogue_for-digital-use-only_noprint_tcm_12-549101.pdf
19. Surface Treatment experts. (n.d.). Electroplating Services for Rail and Transportation Industry. https://www.sharrettsplating.com/coatings/
20. Surface Treatment experts (n.d.). History of Electroplating. www.sharrettsplating.com/blog/?s=silver+electroplating.
21. Shi, Z., Wu, S., Lin, S., Sun, J., Huang, H., Kong, D., ... & Zhou, C. (2023). Enhanced oxidization and corrosion resistance of silver nanowire based transparent conductor by nickel electroplating to obtain power conversion

efficiency> 18% in perovskite solar cells. Applied Surface Science, 609, 155250.

22. Mäkinen, M., Jauhiainen, E., Matilainen, V. P., Riihimäki, J., Ritvanen, J., Piili, H., & Salminen, A. (2015). Preliminary comparison of properties between Ni-electroplated stainless-steel parts fabricated with laser additive manufacturing and conventional machining. Physics Procedia, 78, 337-346.
23. Savjani, N., Mercadillo, V. O., Hodgeman, D., Paterakis, G., Deng, Y., Vallés, C., ... & Kinloch, I. A. (2023). Tribology of Copper Metal Matrix Composites Reinforced with Fluorinated Graphene Oxide Nanosheets: Implications for Solid Lubricants in Mechanical Switches. ACS Applied Nano Materials.
24. Eslami, M., Saghafian, H., Golestani-fard, F., & Robin, A. (2014). Effect of electrodeposition conditions on the properties of Cu–Si3N4 composite coatings. Applied surface science, 300, 129-140.
25. Mokabber, T., Rastegari, S., & Razavizadeh, H. (2013). Effect of electroplating parameters on properties of Zn–nano-TiO2 composite coatings. Surface engineering, 29(1), 41-45.
26. El Jaouhari, A., Chennah, A., Jaddi, S. B., Ahsaine, H. A., Anfar, Z., Alaoui, Y. T., ... & Bazzaoui, M. (2019). Electrosynthesis of zinc phosphate-polypyrrole coatings for improved corrosion resistance of steel. Surfaces and Interfaces, 15, 224-231.
27. Liu, Y., Ma, G., Zhu, L., Wang, H., Han, C., Li, Z., ... & Huang, Y. (2022). Structure–performance evolution mechanism of the wear failure process of coated spherical plain bearings. Engineering Failure Analysis, 135, 106097.
28. Xue, Y., Wu, C., Shi, X., Zhang, K., & Huang, Q. (2021). High temperature tribological behavior of textured CSS-42L bearing steel filled with Sn-Ag-Cu-Ti3C2. Tribology International, 164, 107205.
29. Xue, Y., Shi, X., Zhou, H., Lu, G., & Zhang, J. (2020). Effects of groove-textured surface combined with Sn–Ag–Cu lubricant on friction-induced vibration and noise of GCr15 bearing steel. Tribology International, 148, 106316.
30. Zhou, H., Shi, X., Lu, G., Chen, Y., Yang, Z., Wu, C., ... & Ibrahim, A. M. M. (2020). Friction and wear behaviors of TC4 alloy with surface microporous

channels filled by Sn-Ag-Cu and Al2O3 nanoparticles. Surface and Coatings Technology, 387, 125552.

31. Liu, X., Shi, X., Lu, G., Deng, X., Zhou, H., Yan, Z., ... & Xue, B. (2019). The synergistic lubricating mechanism of Sn-Ag-Cu and C60 on the worn surface of M50 self-lubricating material at elevated loads. Journal of Alloys and Compounds, 777, 271-284.
32. Lu, G., Shi, X., Zhang, J., Zhou, H., Xue, Y., & Ibrahim, A. M. M. (2020). Effects of surface composite structure with micro-grooves and Sn-Ag-Cu on reducing friction and wear of Ni3Al alloys. Surface and Coatings Technology, 387, 125540
33. Xue, Y., Shi, X., Lu, G., Zhou, H., Chen, Y., & Shu, J. (2020). Tribological behavior of M50-Sn-Ag-Cu composites with curved microchannels. Journal of Materials Engineering and Performance, 29, 2190-2201.
34. Liu, A., Ren, X., Wang, B., Zhang, J., Yang, P., Zhang, J., & An, M. (2014). Complexing agent study via computational chemistry for environmentally friendly silver electrodeposition and the application of a silver deposit. RSC advances, 4(77), 40930-40940.
35. BRIZMER, V., STADLER, K., HAN, B., & MATTA, C. A Study on Tribological Performance of Black Oxide Coating for Bearing Applications.
36. Ooi, S. W., Yan, P., & Vegter, R. H. (2019). Black oxide coating and its effectiveness on prevention of hydrogen uptake. Materials Science and Technology, 35(1), 12-25.
37. Stadler, K., Han, B., Brizmer, V., & Pasaribu, R. (2015). Benefits of using black oxidized bearings in wind applications. Evolution, 2, 25-30.
38. Luyckx, J. (2011, November). Hammering wear impact fatigue hypothesis WEC/irWEA failure mode on roller bearings. In Wind Turbine Tribology Seminar, Renaissance Boulder Flatiron Hotel Broomfield, CO, USA.
39. Reichelt, M., Weirich, T. E., Mayer, J., Wolf, T., Loos, J., Gold, P. W., & Fajfrowski, M. (2006). TEM and nanomechanical studies on tribological surface modifications formed on roller bearings under controlled lubrication conditions. Journal of materials science, 41, 4543-4553.

40. Pasaribu, H. R., & Lugt, P. M. (2012). The composition of reaction layers on rolling bearings lubricated with gear oils and its correlation with rolling bearing performance. Tribology transactions, 55(3), 351-356.
41. Song, R. H., Pyun, S. I., & Oriani, R. A. (1991). The hydrogen permeation through passivating film on iron by modulation method. Electrochimica acta, 36(5-6), 825-831.
42. Evolution Technology magazine SKF (2015). Benefits of Using Black Oxidized Bearings in Wind Applications. https://evolution.skf.com/benefits-of-using-black-oxidized-bearings-in-wind-applications/
43. Holweger, W., & Loos, J. (2011). Interaction of Rolling Bearing Fatigue Life with New Material Phenomenons of Special Applications. In Proc. of the 14th Heavy Drive Train Conference (pp. 223-238).
44. Uyama, H. (2011). The mechanism of white structure flaking in rolling bearings. In National renewable energy laboratory wind turbine tribology seminar.
45. Strandell, I., Fajers, C., & Lund, T. (2010, September). Corrosion—one root cause for premature failures. In 37th Leeds-Lyon symposium on tribology.
46. Plaza, E. G., & López, P. N. (2017). Surface roughness monitoring by singular spectrum analysis of vibration signals. Mechanical systems and signal processing, 84, 516-530.
47. Plaza, E. G., & López, P. N. (2018). Application of the wavelet packet transform to vibration signals for surface roughness monitoring in CNC turning operations. Mechanical Systems and Signal Processing, 98, 902-919.
48. Jiang, F., Zhu, Z., & Li, W. (2018). An improved VMD with empirical mode decomposition and its application in incipient fault detection of rolling bearing. IEEE Access, 6, 44483-44493
49. Dragomiretskiy, K., & Zosso, D. (2013). Variational mode decomposition. IEEE transactions on signal processing, 62(3), 531-544.
50. Feng, Z., Zhang, D., & Zuo, M. J. (2017). Adaptive mode decomposition methods and their applications in signal analysis for machinery fault diagnosis: a review with examples. IEEE access, 5, 24301-24331.

51. Wang, Y., Markert, R., Xiang, J., & Zheng, W. (2015). Research on variational mode decomposition and its application in detecting rub-impact fault of the rotor system. Mechanical Systems and Signal Processing, 60, 243-251.
52. Aneesh, C., Kumar, S., Hisham, P. M., & Soman, K. P. (2015). Performance comparison of variational mode decomposition over empirical wavelet transform for the classification of power quality disturbances using support vector machine. Procedia Computer Science, 46, 372-380.
53. Li, H., Liu, T., Wu, X., & Chen, Q. (2020). An optimized VMD method and its applications in bearing fault diagnosis. Measurement, 166, 108185.
54. Cui, H., Guan, Y., & Chen, H. (2021). Rolling element fault diagnosis based on VMD and sensitivity MCKD. IEEE Access, 9, 120297-120308.
55. Franco Jr, A. R., Pintaúde, G., Sinatora, A., Pinedo, C. E., & Tschiptschin, A. P. (2004). The use of a Vickers indenter in depth sensing indentation for measuring elastic modulus and Vickers hardness. Materials Research, 7, 483-491.
56. Deng, H., Shi, H., & Tsuruoka, S. (2010). Influence of coating thickness and temperature on mechanical properties of steel deposited with Co-based alloy hardfacing coating. Surface and Coatings Technology, 204(23), 3927-3934.
57. Lima, M. M., Godoy, C., Modenesi, P. J., Avelar-Batista, J. C., Davison, A., & Matthews, A. (2004). Coating fracture toughness determined by Vickers indentation: an important parameter in cavitation erosion resistance of WC–Co thermally sprayed coatings. Surface and Coatings Technology, 177, 489-496.
58. Iwamoto, T., & Mackenzie, J. D. (1995). Ormosil coatings of high hardness. Journal of materials science, 30, 2566-2570.
59. Gogolinskii, K. V., Syasko, V. A., Umanskii, A. S., Nikazov, A. A., & Bobkova, T. I. (2019). Mechanical properties measurements with portable hardness testers: advantages, limitations, prospects. In Journal of Physics: Conference Series (Vol. 1384, No. 1, p. 012012). IOP Publishing.
60. Junek, M., Janovec, J., & Duchacek, P. (2017). Dependence of ultrasonic contact impedance hardness on Young's modulus of elasticity of creep-resistant steels. Acta IMEKO, 6(1), 27-32.

61. Pakos, R. (2002). Ultrasonic hardness measurements. Welding international, 16(2), 116-119.
62. Kumar, T. A., Anne, G., Prasanna, N. D., & Muralidhara, M. K. (2014). Effect of electromagnetic induction and heat treatment on the mechanical and wear properties of LM25 alloy. Procedia materials science, 5, 550-557.
63. Scheffer, C., & Heyns, P. S. (2001). Wear monitoring in turning operations using vibration and strain measurements. Mechanical systems and signal processing, 15(6), 1185-1202.
64. Li, K. M., Song, K. J., Guan, J., Yang, F., & Liu, J. (2020). Tribocorrosion behavior of a Ti6Al4V alloy electromagnetic induction nitride layer in a fluorine-containing solution. Surface and Coatings Technology, 386, 125506.
65. He, M., Li, X., Cao, Z., Dong, S., Liu, T., & Wang, Q. (2017). Effect of heat treatment on the microstructure and properties of Cu–0.6 Cr–0.2 Zr alloy induction coil in electromagnetic steel-teeming system. Vacuum, 146, 130-135.
66. Liu, X., Fang, K., Xu, D., Zhang, L., & Fang, H. (2012). Control of Welding Cold Cracking with Trailing Electromagnetic Induction Heating in High Strength Steel Weldment. Journal of Computational and Theoretical Nanoscience, 9(9), 1352-1356.
67. Thomazella, R., Lopes, W. N., Aguiar, P. R., Alexandre, F. A., Fiocchi, A. A., & Bianchi, E. C. (2019). Digital signal processing for self-vibration monitoring in grinding: A new approach based on the time-frequency analysis of vibration signals. Measurement, 145, 71-83.
68. Dimla, Snr, D. E. (2002). The correlation of vibration signal features to cutting tool wear in a metal turning operation. The International Journal of Advanced Manufacturing Technology, 19, 705-713.
69. Abu-Mahfouz, I. (2003). Drilling wear detection and classification using vibration signals and artificial neural network. International Journal of Machine Tools and Manufacture, 43(7), 707-720.
70. Alonso, F. J., & Salgado, D. R. (2008). Analysis of the structure of vibration signals for tool wear detection. Mechanical systems and signal processing, 22(3), 735-748.

71. Gegner, J., Schlier, L., & Nierlich, W. (2009). Evidence and analysis of thermal static strain aging in the deformed surface zone of finish-machined hardened steel. Powder Diffraction, 24(S1), S45-S50.
72. Portogallo, M., Simoni, S., Vignoli, G., & Bertoldi, W. (2022). Analysis of the vibration modes of impact geoplates and implications for bedload flux and grain size measurements. Water Resources Research, 58(9), e2022WR032116.
73. Ahn, B., Lee, S. S., Hong, S. T., Kim, H. C., & Kang, S. J. L. (1999). Application of the acoustic resonance method to evaluate the grain size of low carbon steels. NDT & E International, 32(2), 85-89.
74. Li, Z., & Itakura, K. (2021). Modeling and simulation of the effect of rock grain sizes on vibration characteristics when rock drilling. In IOP Conference Series: Earth and Environmental Science (Vol. 861, No. 4, p. 042031). IOP Publishing.
75. Lazarová, E., Kruľáková, M., Krúpa, V., Labaš, M., & Feriančiková, K. (2022). Regime and rock identification in disintegration by drilling based on vibration signal differentiation. International Journal of Rock Mechanics and Mining Sciences, 149, 104984.
76. Feng, K., Smith, W. A., Borghesani, P., Randall, R. B., & Peng, Z. (2021). Use of cyclostationary properties of vibration signals to identify gear wear mechanisms and track wear evolution. Mechanical Systems and Signal Processing, 150, 107258.
77. Stadler, K., Brizmer, V., Matta, C., & Han, B. (2017). Different performance aspects of black oxide coating for bearing applications. In Conference for Wind Power Drives 2017: Tagungsband zur Konferenz (Vol. 3, p. 291). BoD–Books on Demand.
78. Cambow, R., Singh, M., & Singh, A. (2023). A study on properties of bearing coatings and their degradation measurement: Challenges and solutions. In AIP Conference Proceedings (Vol. 2800, No. 1). AIP Publishing.
79. Cambow, R., & Singh, M. (2024). Analysis of different coatings for properties on ball bearing using vibration signal. In AIP Conference Proceedings (Vol. 2962, No. 1). AIP Publishing.

80. Cambow, R., Singh, M., Bagha, A. K., & Singh, H. (2018). To compare the effect of different level of self-lubrication for bearings using statistical analysis of vibration signal. Materials Today: Proceedings, 5(14), 28364-28373.
81. SKF (n.d.). 6205 Deep groove ball bearing. https://www.skf.com/in/products/rolling-bearings/ball-bearings/deep-groove-ball-bearings/productid-6205
82. Handbook, A. S. M. (1994). Surface engineering. ASM International, Handbook Committee, 5(s 346).
83. Chung, P. P., Wang, J., & Durandet, Y. (2019). Deposition processes and properties of coatings on steel fasteners—A review. Friction, 7, 389-416.
84. Plante, T., Nejadpak, A., & Yang, C. X. (2015). Vibration analysis: Fault detection and failure prediction. In Proc. IEEE AUTOTESTCON (p. 5).
85. Mitutoyo America Corporation. (2015). Portable surface roughness tester SURFTEST SJ-410 Series. https://www.mitutoyo.com/webfoo/wp-content/uploads/2110_SJ-410.pdf
86. Verma, J., Nagdeve, L., & Kumar, H. (2022). Tribological investigations into pin-on-disc tribometer under dry sliding conditions at various temperature ranges. Proceedings of the Institution of Mechanical Engineers, Part E: Journal of Process Mechanical Engineering, 236(1), 178-186.
87. Geochemical Instrumentation and Analysis. (2007, May 17). Scanning Electron Microscopy. https://serc.carleton.edu/research_education/geochemsheets/techniques/SEM.html
88. Struers Ensuring Certainity. (n.d.). How To Do Etching. https://www.struers.com/en/Knowledge/Etching#etchingabout
89. Kumar, S., Lokesha, M., Kumar, K., & Srinivas, K. R. (2018). Vibration based fault diagnosis techniques for rotating mechanical components. In IOP Conference Series: Materials Science and Engineering (Vol. 376, No. 1, p. 012109). IOP Publishing.
90. Arjunan, A., Baroutaji, A., Robinson, J., & Olabi, A. G. (2021). Smart tribological coating.

91. Renevier, N. M., Hamphire, J., Fox, V. C., Witts, J., Allen, T., & Teer, D. G. (2001). Advantages of using self-lubricating, hard, wear-resistant MoS2-based coatings. Surface and Coatings Technology, 142, 67-77.
92. Liu, K., Yan, H., Zhang, P., Zhao, J., Yu, Z., & Lu, Q. (2020). Wear behaviors of TiN/WS2+ hBN/NiCrBSi self-lubricating composite coatings on TC4 alloy by laser cladding. Coatings, 10(8), 747.
93. Kumar, A., Jayakumar, T., Palanichamy, P., & Raj, B. (1999). Influence of grain size on ultrasonic spectral parameters in AISI type 316 stainless steel. Scripta Materialia, 40(3), 333-340..
94. Junior, R. F. R., dos Santos Areias, I. A., & Gomes, G. F. (2021). Fault detection and diagnosis using vibration signal analysis in frequency domain for electric motors considering different real fault types. Sensor Review, 41(3), 311-319.
95. Vernekar, K., Kumar, H., & Gangadharan, K. V. (2014). Gear fault detection using vibration analysis and continuous wavelet transform. Procedia Materials Science, 5, 1846-1852.
96. Kafeel, A., Aziz, S., Awais, M., Khan, M. A., Afaq, K., Idris, S. A., ... & Mostafa, S. M. (2021). An Expert System for Rotating Machine Fault Detection Using Vibration Signal Analysis. Sensors, 21(22), 7587.
97. Li, H., Wang, C., Chen, C., & Yan, G. (2011). Review of vibration signals trend forecasting methods. Procedia Environmental Sciences, 10, 837-842.
98. Maheswari, R. U., & Umamaheswari, R. (2017). Trends in non-stationary signal processing techniques applied to vibration analysis of wind turbine drive train–A contemporary survey. Mechanical Systems and Signal Processing, 85, 296-311.
99. Caesarendra, W., & Tjahjowidodo, T. (2017). A review of feature extraction methods in vibration-based condition monitoring and its application for degradation trend estimation of low-speed slew bearing. Machines, 5(4), 21.
100. Zhang, S., & Ganesan, R. (1997). Multivariable trend analysis using neural networks for intelligent diagnostics of rotating machinery.

101. Hong, K., Huang, H., & Zhou, J. (2014). Winding condition assessment of power transformers based on vibration correlation. IEEE Transactions on Power Delivery, 30(4), 1735-1742.
102. Rivas, E., Burgos, J. C., & Garcia-Prada, J. C. (2009). Condition assessment of power OLTC by vibration analysis using wavelet transform. IEEE Transactions on Power Delivery, 24(2), 687-694.
103. Hong, S., Zhou, Z., Zio, E., & Hong, K. (2014). Condition assessment for the performance degradation of bearing based on a combinatorial feature extraction method. Digital Signal Processing, 27, 159-166.
104. Abouhnik, A., & Albarbar, A. (2012). Wind turbine blades condition assessment based on vibration measurements and the level of an empirically decomposed feature. Energy Conversion and Management, 64, 606-613.
105. Yang, Q., Ruan, J., Zhuang, Z., & Huang, D. (2019). Condition evaluation for opening damper of spring operated high-voltage circuit breaker using vibration time-frequency image. IEEE Sensors Journal, 19(18), 8116-8126.
106. Rafiei, M. H., & Adeli, H. (2018). A novel unsupervised deep learning model for global and local health condition assessment of structures. Engineering Structures, 156, 598-607.
107. Delgado-Arredondo, P. A., Morinigo-Sotelo, D., Osornio-Rios, R. A., Avina-Cervantes, J. G., Rostro-Gonzalez, H., & de Jesus Romero-Troncoso, R. (2017). Methodology for fault detection in induction motors via sound and vibration signals. Mechanical Systems and Signal Processing, 83, 568-589.
108. Hong, L., & Dhupia, J. S. (2014). A time domain approach to diagnose gearbox fault based on measured vibration signals. Journal of Sound and Vibration, 333(7), 2164-2180.
109. Aherwar, A. (2012). An investigation on gearbox fault detection using vibration analysis techniques: A review. Australian Journal of Mechanical Engineering, 10(2), 169-183.
110. Amanuel, T., Ghirmay, A., Ghebremeskel, H., Ghebrehiwet, R., & Bahlibi, W. (2021). Design of Vibration Frequency Method with Fine-Tuned Factor for Fault Detection of Three Phase Induction Motor. Journal of Innovative Image Processing (JIIP), 3(01), 52-65.

111. Taghizadeh-Alisaraei, A., & Mahdavian, A. (2019). Fault detection of injectors in diesel engines using vibration time-frequency analysis. Applied Acoustics, 143, 48-58.
112. Yao, R., & Pakzad, S. N. (2012). Autoregressive statistical pattern recognition algorithms for damage detection in civil structures. Mechanical Systems and Signal Processing, 31, 355-368.
113. Sohn, H., Farrar, C. R., Hunter, N. F., & Worden, K. (2001). Structural health monitoring using statistical pattern recognition techniques. J. Dyn. Sys., Meas., Control, 123(4), 706-711.
114. Silva, S. D., Dias Júnior, M., & Lopes Junior, V. (2007). Damage detection in a benchmark structure using AR-ARX models and statistical pattern recognition. Journal of the Brazilian Society of Mechanical Sciences and Engineering, 29, 174-184.
115. Cheung, A., Cabrera, C., Sarabandi, P., Nair, K. K., Kiremidjian, A., & Wenzel, H. (2008). The application of statistical pattern recognition methods for damage detection to field data. Smart materials and structures, 17(6), 065023.
116. Stepanic, P., Latinovic, I. V., & Djurovic, Z. (2009). A new approach to detection of defects in rolling element bearings based on statistical pattern recognition. The International Journal of Advanced Manufacturing Technology, 45, 91-100.
117. Wang, P., & Vachtsevanos, G. (2001). Fault prognostics using dynamic wavelet neural networks. AI EDAM, 15(4), 349-365.
118. Widodo, A., & Yang, B. S. (2011). Machine health prognostics using survival probability and support vector machine. Expert Systems with Applications, 38(7), 8430-8437.
119. Thoppil, N. M., Vasu, V., & Rao, C. S. P. (2021). Deep learning algorithms for machinery health prognostics using time-series data: A review. Journal of Vibration Engineering & Technologies, 1-23.
120. Wang, Y., Xiang, J., Markert, R., & Liang, M. (2016). Spectral kurtosis for fault detection, diagnosis and prognostics of rotating machines: A review with applications. Mechanical Systems and Signal Processing, 66, 679-698.

121. Parker Jr, B. E., Nigro, T. M., Carley, M. P., Barron, R. L., Ward, D. G., Poor, H. V., ... & DuBois, T. A. (1993, September). Helicopter gearbox diagnostics and prognostics using vibration signature analysis. In Applications of Artificial Neural Networks IV (Vol. 1965, pp. 531-542). SPIE.
122. Schwabacher, M. (2005). A survey of data-driven prognostics. Infotech@ Aerospace, 7002.
123. Sutrisno, E., Oh, H., Vasan, A. S. S., & Pecht, M. (2012). Estimation of remaining useful life of ball bearings using data driven methodologies. In 2012 ieee conference on prognostics and health management (pp. 1-7). IEEE.
124. Benkedjouh, T., Medjaher, K., Zerhouni, N., & Rechak, S. (2013). Remaining useful life estimation based on nonlinear feature reduction and support vector regression. Engineering Applications of Artificial Intelligence, 26(7), 1751-1760.
125. Yang, B., Liu, R., & Zio, E. (2019). Remaining useful life prediction based on a double-convolutional neural network architecture. IEEE Transactions on Industrial Electronics, 66(12), 9521-9530.
126. Ahmadzadeh, F., & Lundberg, J. (2014). Remaining useful life estimation. International Journal of System Assurance Engineering and Management, 5, 461-474.
127. Lei, Y., Li, N., Gontarz, S., Lin, J., Radkowski, S., & Dybala, J. (2016). A model-based method for remaining useful life prediction of machinery. IEEE Transactions on reliability, 65(3), 1314-1326.
128. She, D., & Jia, M. (2021). A BiGRU method for remaining useful life prediction of machinery. Measurement, 167, 108277.
129. Zhu, J., Chen, N., & Peng, W. (2018). Estimation of bearing remaining useful life based on multiscale convolutional neural network. IEEE Transactions on Industrial Electronics, 66(4), 3208-3216.
130. Kong, X., Cai, C. S., & Hu, J. (2017). The state-of-the-art on framework of vibration-based structural damage identification for decision making. Applied Sciences, 7(5), 497.

131. Kumar, A., & Kumar, R. (2019). Role of signal processing, modeling and decision making in the diagnosis of rolling element bearing defect: a review. Journal of Nondestructive Evaluation, 38(1), 5.
132. Kuntoğlu, M., Aslan, A., Pimenov, D. Y., Usca, Ü. A., Salur, E., Gupta, M. K., & Sharma, S. (2020). A review of indirect tool condition monitoring systems and decision-making methods in turning: Critical analysis and trends. Sensors, 21(1), 108.
133. Wu, S. J., Gebraeel, N., Lawley, M. A., & Yih, Y. (2007). A neural network integrated decision support system for condition-based optimal predictive maintenance policy. IEEE Transactions on Systems, Man, and Cybernetics-Part A: Systems and Humans, 37(2), 226-236.
134. Teti, R. (2015). Advanced IT methods of signal processing and decision making for zero defect manufacturing in machining. Procedia Cirp, 28, 3-15.
135. Zhang, S., Zhou, J., Wang, E., Zhang, H., Gu, M., & Pirttikangas, S. (2022). State of the art on vibration signal processing towards data-driven gear fault diagnosis. IET Collaborative Intelligent Manufacturing.
136. Dang, H. V., Tran-Ngoc, H., Nguyen, T. V., Bui-Tien, T., De Roeck, G., & Nguyen, H. X. (2020). Data-driven structural health monitoring using feature fusion and hybrid deep learning. IEEE Transactions on Automation Science and Engineering, 18(4), 2087-2103.
137. Martin-Diaz, I., Morinigo-Sotelo, D., Duque-Perez, O., & Romero-Troncoso, R. D. J. (2016). Advances in classifier evaluation: Novel insights for an electric data-driven motor diagnosis. IEEE Access, 4, 7028-7038.
138. Mey, O., & Neufeld, D. (2022). Explainable AI Algorithms for Vibration Data-Based Fault Detection: Use Case-Adadpted Methods and Critical Evaluation. Sensors, 22(23), 9037.
139. Sayyad, S., Kumar, S., Bongale, A., Kamat, P., Patil, S., & Kotecha, K. (2021). Data-driven remaining useful life estimation for milling process: sensors, algorithms, datasets, and future directions. IEEE Access, 9, 110255-110286.

140. Zhang, W., Yang, D., & Wang, H. (2019). Data-driven methods for predictive maintenance of industrial equipment: A survey. IEEE Systems Journal, 13(3), 2213-2227.
141. Cerrada, M., Sánchez, R. V., Li, C., Pacheco, F., Cabrera, D., de Oliveira, J. V., & Vásquez, R. E. (2018). A review on data-driven fault severity assessment in rolling bearings. Mechanical Systems and Signal Processing, 99, 169-196.
142. Farrar, C. R., & Worden, K. (2012). Structural health monitoring: a machine learning perspective. John Wiley & Sons.
143. Salawu, O. S. (1997). Detection of structural damage through changes in frequency: a review. Engineering structures, 19(9), 718-723.
144. Bhowmik, B., Tripura, T., Hazra, B., & Pakrashi, V. (2019). First-order eigen-perturbation techniques for real-time damage detection of vibrating systems: Theory and applications. Applied Mechanics Reviews, 71(6).
145. Bhowmik, B., Krishnan, M., Hazra, B., & Pakrashi, V. (2019). Real-time unified single-and multi-channel structural damage detection using recursive singular spectrum analysis. Structural Health Monitoring, 18(2), 563-589.
146. Iakovidis, I., Cross, E. J., & Worden, K. (2018). A principled multiresolution approach for signal decomposition. In Journal of Physics: Conference Series (Vol. 1106, No. 1, p. 012001). IOP Publishing.
147. Huang, N. E., Shen, Z., Long, S. R., Wu, M. C., Shih, H. H., Zheng, Q., ... & Liu, H. H. (1998). The empirical mode decomposition and the Hilbert spectrum for nonlinear and non-stationary time series analysis. Proceedings of the Royal Society of London. Series A: mathematical, physical and engineering sciences, 454(1971), 903-995.
148. Gokhale, M. Y., & Khanduja, D. K. (2010). Time domain signal analysis using wavelet packet decomposition approach. Int'l J. of Communications, Network and System Sciences, 3(03), 321.
149. Barbosh, M., Singh, P., & Sadhu, A. (2020). Empirical mode decomposition and its variants: A review with applications in structural health monitoring. Smart Materials and Structures, 29(9), 093001.

150. Isham, M. F., Leong, M. S., Lim, M. H., & Zakaria, M. K. (2019). A review on variational mode decomposition for rotating machinery diagnosis. In MATEC Web of Conferences (Vol. 255, p. 02017). EDP Sciences.
151. Figueiredo, E., Park, G., Farrar, C. R., Worden, K., & Figueiras, J. (2011). Machine learning algorithms for damage detection under operational and environmental variability. Structural Health Monitoring, 10(6), 559-572.
152. Rilling, G., Flandrin, P., Gonçalves, P., & Lilly, J. M. (2007). Bivariate empirical mode decomposition. IEEE signal processing letters, 14(12), 936-939.
153. Rehman, N., & Mandic, D. P. (2010). Multivariate empirical mode decomposition. Proceedings of the Royal Society A: Mathematical, Physical and Engineering Sciences, 466(2117), 1291-1302.
154. McNeill, S. I. (2016). Decomposing a signal into short-time narrow-banded modes. Journal of Sound and Vibration, 373, 325-339.
155. Civera, M., & Surace, C. (2021). A comparative analysis of signal decomposition techniques for structural health monitoring on an experimental benchmark. Sensors, 21(5), 1825.
156. Maheshwari, S., & Kumar, A. (2014). Empirical mode decomposition: theory & applications. International Journal of Electronic Engineering, 873-878.
157. Empirical Mode Decomposition (n.d.). What Is Empirical Mode Decomposition? https://in.mathworks.com/discovery/empirical-mode-decomposition.html
158. Yang, J. N., Lei, Y., Pan, S., & Huang, N. (2003). System identification of linear structures based on Hilbert–Huang spectral analysis. Part 1: normal modes. Earthquake engineering & structural dynamics, 32(9), 1443-1467.
159. Shi, Z. Y., & Law, S. S. (2007). Identification of linear time-varying dynamical systems using Hilbert transform and empirical mode decomposition method.
160. Yu, D. J., & Ren, W. X. (2005). EMD-based stochastic subspace identification of structures from operational vibration measurements. Engineering Structures, 27(12), 1741-1751.

161. Chen, J. U. N. (2009). Application of empirical mode decomposition in structural health monitoring: some experience. Advances in Adaptive Data Analysis, 1(04), 601-621.
162. Lei, Y., Lin, J., He, Z., & Zuo, M. J. (2013). A review on empirical mode decomposition in fault diagnosis of rotating machinery. Mechanical systems and signal processing, 35(1-2), 108-126.
163. Liu, J., Wang, X., Yuan, S., & Li, G. (2006). On Hilbert-Huang transform approach for structural health monitoring. Journal of Intelligent Material Systems and Structures, 17(8-9), 721-728.
164. Huang, N. E. (2014). Hilbert-Huang transform and its applications (Vol. 16). World Scientific.
165. Wu, Z., & Huang, N. E. (2014). Statistical significance test of intrinsic mode functions. In Hilbert–Huang Transform and Its Applications (pp. 149-169).
166. Colominas, M. A., Schlotthauer, G., & Torres, M. E. (2014). Improved complete ensemble EMD: A suitable tool for biomedical signal processing. Biomedical Signal Processing and Control, 14, 19-29.
167. Wu, Z., & Huang, N. E. (2009). Ensemble empirical mode decomposition: a noise-assisted data analysis method. Advances in adaptive data analysis, 1(01), 1-41.
168. Wickerhauser, M. V. (1991). INRIA lectures on wavelet packet algorithms. Yale Univ., Department of Mathematics.
169. Soman, K. P. (2010). Insight into wavelets: from theory to practice. PHI Learning Pvt. Ltd.
170. Fu, S., Muralikrishnan, B., & Raja, J. (2003). Engineering surface analysis with different wavelet bases. J. Manuf. Sci. Eng., 125(4), 844-852.
171. Mojsilovic, A., Popovic, M. V., & Rackov, D. M. (2000). On the selection of an optimal wavelet basis for texture characterization. IEEE Transactions on image processing, 9(12), 2043-2050.
172. Safavian, L. S., Kinsner, W., & Turanli, H. (2005). Aquantitative comparison of different mother wavelets for characterizing transients in power systems. In Canadian Conference on Electrical and Computer Engineering, 2005. (pp. 1461-1464). IEEE.

173. Wang, S. Y., Liu, X., Yianni, J., Aziz, T. Z., & Stein, J. F. (2004). Extracting burst and tonic components from surface electromyograms in dystonia using adaptive wavelet shrinkage. Journal of neuroscience methods, 139(2), 177-184.
174. Ahuja, N., Lertrattanapanich, S., & Bose, N. K. (2005). Properties determining choice of mother wavelet. IEE Proceedings-Vision, Image and Signal Processing, 152(5), 659-664.
175. Flanders, M. (2002). Choosing a wavelet for single-trial EMG. Journal of neuroscience methods, 116(2), 165-177.
176. Faisal, M. F., & Mohamed, A. (2008). Comparing the performance of various mother wavelet functions in detecting actual 3-phase voltage sags. In 2008 IEEE 2nd International Power and Energy Conference (pp. 657-661). IEEE.
177. Ahadi, M., & Bakhtiar, M. S. (2010). Leak detection in water-filled plastic pipes through the application of tuned wavelet transforms to acoustic emission signals. Applied Acoustics, 71(7), 634-639.
178. Tang, B., Liu, W., & Song, T. (2010). Wind turbine fault diagnosis based on Morlet wavelet transformation and Wigner-Ville distribution. Renewable Energy, 35(12), 2862-2866.
179. Saito, N. (1994). Simultaneous noise suppression and signal compression using a library of orthonormal bases and the minimum description length criterion. In Wavelet Analysis and Its Applications (Vol. 4, pp. 299-324). Academic Press.
180. Hamid, E. Y., Mardiana, R., & Kawasaki, Z. I. (2001). Wavelet-based compression of power disturbances using the minimum description length criterion. In 2001 Power Engineering Society Summer Meeting. Conference Proceedings (Cat. No. 01CH37262) (Vol. 3, pp. 1772-1777). IEEE.
181. Khan, M. A. S. K., Radwan, T. S., & Rahman, M. A. (2006). Wavelet packet transform based protection of three-phase IPM motor. In 2006 IEEE International Symposium on Industrial Electronics (Vol. 3, pp. 2122-2127). IEEE.

182. Khan, M. A. S., & Rahman, M. A. (2010). A novel neuro-wavelet-based self-tuned wavelet controller for IPM motor drives. IEEE Transactions on Industry Applications, 46(3), 1194-1203.
183. Yang, L., Judd, M. D., & Bennoch, C. J. (2004). Denoising UHF signal for PD detection in transformers based on wavelet technique. In The 17th Annual Meeting of the IEEE Lasers and Electro-Optics Society, 2004. LEOS 2004. (pp. 166-169). IEEE.
184. Li, W. (2009). Research on extraction of partial discharge signals based on wavelet analysis. In 2009 International Conference on Electronic Computer Technology (pp. 545-548). IEEE.
185. Singh, B. N., & Tiwari, A. K. (2006). Optimal selection of wavelet basis function applied to ECG signal denoising. Digital signal processing, 16(3), 275-287.
186. Zhang, L., Bao, P., & Wu, X. (2005). Multiscale LMMSE-based image denoising with optimal wavelet selection. IEEE Transactions on circuits and systems for video technology, 15(4), 469-481.
187. Tsui, P. P., & Basir, O. A. (2006). Wavelet basis selection and feature extraction for shift invariant ultrasound foreign body classification. Ultrasonics, 45(1-4), 1-14.
188. Yan, R. (2007). Base wavelet selection criteria for non-stationary vibration analysis in bearing health diagnosis. University of Massachusetts Amherst.
189. Rafiee, J., & Tse, P. W. (2009). Use of autocorrelation of wavelet coefficients for fault diagnosis. Mechanical Systems and Signal Processing, 23(5), 1554-1572.
190. Rafiee, J., Rafiee, M. A., & Tse, P. W. (2010). Application of mother wavelet functions for automatic gear and bearing fault diagnosis. Expert systems with applications, 37(6), 4568-4579.
191. Rafiee, J., Tse, P. W., Harifi, A., & Sadeghi, M. H. (2009). A novel technique for selecting mother wavelet function using an intelli gent fault diagnosis system. Expert Systems with Applications, 36(3), 4862-4875.
192. Morsi, W. G., & El-Hawary, M. E. (2008). The most suitable mother wavelet for steady-state power system distorted waveforms. In 2008 canadian

conference on electrical and computer engineering (pp. 000017-000022). IEEE.

193. Cheng, H. D., Min, R., & Zhang, M. (2010). Automatic wavelet base selection and its application to contrast enhancement. Signal Processing, 90(4), 1279-1289.
194. Phinyomark, A., Limsakul, C., & Phukpattaranont, P. (2009). Evaluation of wavelet function based on robust emg feature extraction. In 7th PSU Engineering Conference (p. 277281).
195. Rafiee, J., Rafiee, M. A., Prause, N., & Schoen, M. P. (2011). Wavelet basis functions in biomedical signal processing. Expert systems with Applications, 38(5), 6190-6201.
196. Kankar, P. K., Sharma, S. C., & Harsha, S. P. (2011). Fault diagnosis of ball bearings using continuous wavelet transform. Applied Soft Computing, 11(2), 2300-2312.
197. Heidari, M., Homaei, H., Golestanian, H., & Heidari, A. (2016). Fault diagnosis of gearboxes using wavelet support vector machine, least square support vector machine and wavelet packet transform. Journal of Vibroengineering, 18(2), 860-875.
198. Zhang, X., Feng, N., Wang, Y., & Shen, Y. (2015). Acoustic emission detection of rail defect based on wavelet transform and Shannon entropy. Journal of Sound and Vibration, 339, 419-432.
199. Yang, Q., & Wang, J. (2015). Multi-level wavelet shannon entropy-based method for single-sensor fault location. Entropy, 17(10), 7101-7117.
200. Deák, K., Mankovits, T., & Kocsis, I. (2017). Optimal Wavelet Selection for the Size Estimation of Manufacturing Defects of Tapered Roller Bearings with Vibration Measurement using Shannon Entropy Criteria. Journal of Mechanical Engineering/Strojniški Vestnik, 63(1).
201. Chaitanya, B. K., Yadav, A., Pazoki, M., & Abdelaziz, A. Y. (2021). A comprehensive review of islanding detection methods. Uncertainties in Modern Power Systems, 211-256.

202. Dominique, Z., & Konstantin, D. (2014). Variational mode decomposition. IEEE Transactions on Signal Processing A Publication of the IEEE Signal Processing Society, 62, 531-544.
203. Bertsekas, D. P. (1976). Multiplier methods: A survey. Automatica, 12(2), 133-145.
204. Nocedal, J., & Wright, S. J. (Eds.). (1999). Numerical optimization. New York, NY: Springer New York.
205. Hestenes, M. R. (1969). Multiplier and gradient methods. Journal of optimization theory and applications, 4(5), 303-320.
206. Rockafellar, R. T. (1973). A dual approach to solving nonlinear programming problems by unconstrained optimization. Mathematical programming, 5(1), 354-373..
207. Bertsekas, D. P. (1982). Lagrange Multiplier Methods in Constrained Optimization.
208. Fu, W., Zhou, J., & Zhang, Y. (2015). Fault diagnosis for rolling element bearings with VMD time-frequency analysis and SVM. In 2015 Fifth International Conference on Instrumentation and Measurement, Computer, Communication and Control (IMCCC) (pp. 69-72). IEEE.
209. Wang, S., Zou, X., Zeng, L., Song, J., Zhou, L., Ding, M., & Yuchi, M. (2022). Combination of variational mode decomposition and coherent factor for ultrasound computer tomography. Technology and Health Care, 30(S1), 163-171.
210. Boyd, S., Parikh, N., Chu, E., Peleato, B., & Eckstein, J. (2011). Distributed optimization and statistical learning via the alternating direction method of multipliers. Foundations and Trends® in Machine learning, 3(1), 1-122.
211. Ren, H., Liu, W., Shan, M., & Wang, X. (2019). A new wind turbine health condition monitoring method based on VMD-MPE and feature-based transfer learning. Measurement, 148, 106906.
212. Yang, H., Liu, S., & Zhang, H. (2017). Adaptive estimation of VMD modes number based on cross correlation coefficient. Journal of Vibroengineering, 19(2), 1185-1196.

213. Chen, Z., Li, Y., Cao, R., Ali, W., Yu, J., & Liang, H. (2019). A new feature extraction method for ship-radiated noise based on improved CEEMDAN, normalized mutual information and multiscale improved permutation entropy. Entropy, 21(6), 624.
214. Lu, J., Yue, J., Zhu, L., & Li, G. (2020). Variational mode decomposition denoising combined with improved Bhattacharyya distance. Measurement, 151, 107283.
215. Liu, H., & Chen, C. (2019). Data processing strategies in wind energy forecasting models and applications: A comprehensive review. Applied Energy, 249, 392-408.
216. Gu, W., & Zhou, L. (2020). Evaluation on filter performance of variational mode decomposition and its application in separating closely spaced modes. Shock and Vibration, 2020, 1-16.
217. Li, H., Liu, T., Wu, X., & Chen, Q. (2020). Application of optimized variational mode decomposition based on kurtosis and resonance frequency in bearing fault feature extraction. Transactions of the Institute of Measurement and Control, 42(3), 518-527.
218. Yang, R., Zhang, Z., & Chen, Y. (2022). Analysis of vibration signals for a ball bearing-rotor system with raceway local defects and rotor eccentricity. Mechanism and Machine Theory, 169, 104594.
219. Kumar, A., Tang, H., Vashishtha, G., & Xiang, J. (2022). Noise subtraction and marginal enhanced square envelope spectrum (MESES) for the identification of bearing defects in centrifugal and axial pump. Mechanical Systems and Signal Processing, 165, 108366.
220. Kumar, R., & Singh, M. (2013). Outer race defect width measurement in taper roller bearing using discrete wavelet transform of vibration signal. Measurement, 46(1), 537-545.
221. Singh, M., & Kumar, R. (2013). Thrust bearing groove race defect measurement by wavelet decomposition of pre-processed vibration signal. Measurement, 46(9), 3508-3515.

222. Plaza, E. G., López, P. N., & González, E. B. (2019). Efficiency of vibration signal feature extraction for surface finish monitoring in CNC machining. Journal of Manufacturing Processes, 44, 145-157.
223. Jena, D., Singh, M., & Kumar, R. (2012). Radial ball bearing inner race defect width measurement using analytical wavelet transform of acoustic and vibration signal. Measurement Science Review, 12(4), 141-148.
224. Cambow, R., & Singh, M. (2021). Comparison of roughness level in Ball bearing using statistical analysis of vibration signal. In AIP Conference Proceedings (Vol. 2352, No. 1, p. 020084). AIP Publishing LLC
225. Boyd, S., Parikh, N., Chu, E., Peleato, B., & Eckstein, J. (2011). Distributed optimization and statistical learning via the alternating direction method of multipliers. Foundations and Trends® in Machine learning, 3(1), 1-122.
226. Plaza, E. G., & López, P. N. (2017). Surface roughness monitoring by singular spectrum analysis of vibration signals. Mechanical systems and signal processing, 84, 516-530.
227. Plaza, E. G., & López, P. N. (2018). Application of the wavelet packet transform to vibration signals for surface roughness monitoring in CNC turning operations. Mechanical Systems and Signal Processing, 98, 902-919.
228. Wu, T. Y., & Lei, K. W. (2019). Prediction of surface roughness in milling process using vibration signal analysis and artificial neural network. The International Journal of Advanced Manufacturing Technology, 102(1-4), 305-314.
229. Li, S., Li, S., Liu, Z., & Vladimirovich, P. A. (2022). Roughness prediction model of milling noise-vibration-surface texture multi-dimensional feature fusion for N6 nickel metal. Journal of Manufacturing Processes, 79, 166-176.
230. Boyd, Stephen, Neal Parikh, Eric Chu, Borja Peleato, and Jonathan Eckstein. "Distributed Optimization and Statistical Learning via the Alternating Direction Method of Multipliers." Foundations and Trends® in Machine Learning. Vol 3, Number 1, 2011, pp. 1–122.
231. Kondhalkar, G. E., & Diwakar, G. (2020). Crest factor measurement by experimental vibration analysis for preventive maintenance of bearing. In ICRRM 2019–System Reliability, Quality Control, Safety, Maintenance and

Management: Applications to Civil, Mechanical and Chemical Engineering (pp. 133-138). Springer Singapore.

232. Van Hecke, B., Qu, Y., & He, D. (2015). Bearing fault diagnosis based on a new acoustic emission sensor technique. Proceedings of the Institution of Mechanical Engineers, Part O: Journal of Risk and Reliability, 229(2), 105-118.
233. Sugumaran, V., Muralidharan, V., & Ramachandran, K. I. (2007). Feature selection using decision tree and classification through proximal support vector machine for fault diagnostics of roller bearing. Mechanical systems and signal processing, 21(2), 930-942.
234. Dron, J. P., & Bolaers, F. (2004). Improvement of the sensitivity of the scalar indicators (crest factor, kurtosis) using a de-noising method by spectral subtraction: application to the detection of defects in ball bearings. Journal of Sound and Vibration, 270(1-2), 61-73.
235. Bastami, A. R., & Vahid, S. (2021). A comprehensive evaluation of the effect of defect size in rolling element bearings on the statistical features of the vibration signal. Mechanical Systems and Signal Processing, 151, 107334.
236. Rahman, M., Khanam, F., Ahmad, M., & Uddin, M. S. (2020). Multiclass EEG signal classification utilizing Rényi min-entropy-based feature selection from wavelet packet transformation. Brain informatics, 7(1), 1-11.
237. Singh, M., & Kumar, R. (2013). Thrust bearing groove race defect measurement by wavelet decomposition of pre-processed vibration signal. Measurement, 46(9), 3508-3515.
238. Sharma, A., Amarnath, M., & Kankar, P. K. (2016). Feature extraction and fault severity classification in ball bearings. Journal of Vibration and Control, 22(1), 176-192.
239. Brkovic, A., Gajic, D., Gligorijevic, J., Savic-Gajic, I., Georgieva, O., & Di Gennaro, S. (2017). Early fault detection and diagnosis in bearings for more efficient operation of rotating machinery. Energy, 136, 63-71.
240. Bameri, A., Cheraghi Seifabad, M., & Hoseinie, S. H. (2021). Laboratorial studies for the prediction of rock texture and hardness using vibration

measurement while drilling. Bulletin of Engineering Geology and the Environment, 80, 8311-8318.

241. Vasudev, H., Singh, P., Thakur, L., & Bansal, A. (2020). Mechanical and microstructural characterization of microwave post processed Alloy-718 coating. Materials Research Express, 6(12), 1265f5.

Appendix

Statistical parameters of non-responsive decomposed levels at 600 rpm

Table A1: Statistical parameters of IMF 1 at 600 rpm

Coating	*Ra*	*RMS*	*Skewness*	*Kurtosis*	*Variance*	*Shannon Entropy*	*Log Energy*	*Crest Factor*
Nickel	0.29	0.0572	-0.0030	16.7910	0.0033	9.1660E+02	-4.7358E+05	17.4657
Copper	0.52	0.6907	-0.0010	16.3892	0.4770	-2.3808E+04	-1.6267E+05	14.5551
ZnP	0.7	0.4895	-0.0011	23.8247	0.2396	-9.1546E+03	-2.3932E+05	14.1663
Silver	2.65	0.5635	-0.0031	63.7300	0.3175	-3.0721E+04	-2.4359E+05	21.6952
Black Oxide	3.22	0.3346	-0.0008	3.1906	0.1119	1.0248E+04	-2.2318E+05	5.2739

Table A2: Statistical parameters of IMF 2 at 600 rpm

Coating	*R_a*	*RMS*	*Skewness*	*Kurtosis*	*Variance*	*Shannon Entropy*	*Log Energy*	*Crest Factor*
Nickel	0.29	0.0692	0.0010	16.1920	0.0048	1.1904E+03	-4.5757E+05	15.2598
Copper	0.52	0.6793	-0.0015	5.3210	0.4615	-6.2368E+03	-1.4467E+05	6.8680
ZnP	0.7	0.3696	0.0018	8.9878	0.1366	6.2314E+03	-2.3825E+05	10.3832
Silver	2.65	0.8240	-0.0084	13.7681	0.6790	-5.4443E+04	-1.5870E+05	9.7533
Black Oxide	3.22	0.2952	0.0004	3.1938	0.0871	9.3610E+03	-2.3978E+05	4.5429

Table A3: Statistical parameters of IMF 3 at 600 rpm

Coating	*R_a*	*RMS*	*Skewness*	*Kurtosis*	*Variance*	*Shannon Entropy*	*Log Energy*	*Crest Factor*
Nickel	0.29	0.0912	-0.0034	10.6744	0.0083	1.8468E+03	-4.1990E+05	14.4297
Copper	0.52	0.5875	-0.0075	4.4207	0.3452	3.4689E+03	-1.5995E+05	7.1354
ZnP	0.7	0.8865	-0.0002	7.3241	0.7859	-4.7177E+04	-1.2063E+05	8.4017
Silver	2.65	0.7028	0.0062	14.6203	0.4940	-2.7488E+04	-1.7243E+05	10.8552
Black Oxide	3.22	0.3531	0.0030	3.3901	0.1247	1.0308E+04	-2.1836E+05	4.6307

Table A4: Statistical parameters of IMF 4 at 600 rpm

Coating	*R_a*	*RMS*	*Skewness*	*Kurtosis*	*Variance*	*Shannon entropy*	*Log Energy*	*Crest Factor*
Nickel	0.29	0.1072	0.0047	6.7441	0.0115	2.4669E+03	-3.8915E+05	9.4908
Copper	0.52	0.2850	-0.0051	3.9663	0.0812	8.4945E+03	-2.5133E+05	5.8306
ZnP	0.7	0.8598	-0.0017	5.8483	0.7393	-3.4287E+04	-1.1772E+05	7.8138
Silver	2.65	0.5749	-0.0032	5.7985	0.3305	1.0091E+03	-1.7165E+05	7.7872
Black Oxide	3.22	0.6349	0.0008	3.4052	0.4031	2.5629E+03	-1.4573E+05	4.8794

Table A5: Statistical parameters of IMF 5 at 600 rpm

Coating	*R_a*	*RMS*	*Skewness*	*Kurtosis*	*Variance*	*Shannon entropy*	*Log Energy*	*Crest Factor*
Nickel	0.29	0.1282	-0.0173	3.7566	0.0164	3.4173E+03	-3.5394E+05	5.4057
Copper	0.52	0.3645	-0.0092	3.7827	0.1329	1.0001E+04	-2.1739E+05	6.1077
ZnP	0.7	0.5028	-0.0093	5.3590	0.2528	5.7325E+03	-1.8823E+05	9.0597
Silver	2.65	0.4098	-0.0065	4.6196	0.1679	8.9103E+03	-2.0939E+05	6.4683
Black Oxide	3.22	0.6860	-0.0002	3.1002	0.4706	9.0577E+01	-1.3109E+05	4.3666

Statistical parameters of non-responsive decomposed levels at 900 rpm

Table A6: Statistical parameters of IMF 1 at 900 rpm

Coating	*R_a*	*RMS*	*Skewness*	*Kurtosis*	*Variance*	*Shannon entropy*	*Log Energy*	*Crest Factor*
Nickel	0.29	0.1737	-0.0020	21.5595	0.0302	3.6243E+03	-3.4747E+05	21.4151
Copper	0.52	1.0936	-0.0036	8.6869	1.1959	-1.0675E+05	-9.3884E+04	10.5799
ZnP	0.7	0.6500	-0.0022	9.1436	0.4225	-9.7256E+03	-1.5947E+05	9.7280
Silver	2.65	1.1082	0.0012	22.7812	1.2280	-1.7291E+05	-1.3893E+05	12.2114
Black Oxide	3.22	0.7747	0.0007	3.1807	0.6001	-9.5547E+03	-1.1535E+05	4.2343

Table A7: Statistical parameters of IMF 2 at 900 rpm

Coating	*R_a*	*RMS*	*Skewness*	*Kurtosis*	*Variance*	*Shannon entropy*	*Log Energy*	*Crest Factor*
Nickel	0.29	0.1692	0.0015	18.1231	0.0286	3.5166E+03	-3.5408E+05	16.5515
Copper	0.52	0.2772	0.0040	3.5065	0.0768	8.6090E+03	-2.5158E+05	7.2891
ZnP	0.7	0.6702	0.0013	3.2507	0.4492	9.7675E+02	-1.3453E+05	5.8372
Silver	2.65	0.7767	0.0028	4.7991	0.6033	-1.7476E+04	-1.2654E+05	6.4016
Black Oxide	3.22	1.2654	0.0019	21.7436	1.6013	-2.4901E+05	-1.1563E+05	13.1383

Table A8: Statistical parameters of IMF 3 at 900 rpm

Coating	R_a	*RMS*	*Skewness*	*Kurtosis*	*Variance*	*Shannon entropy*	*Log Energy*	*Crest Factor*
Nickel	0.29	0.2184	0.0042	9.0939	0.0477	5.2933E+03	-3.0890E+05	9.6058
Copper	0.52	1.3851	-0.0011	3.5264	1.9184	-1.8000E+05	-4.6136E+04	4.7980
ZnP	0.7	1.2262	-0.0002	3.9545	1.5036	-1.2099E+05	-6.2420E+04	6.2884
Silver	2.65	1.6126	0.0061	6.2299	2.6005	-3.4241E+05	-4.0969E+04	6.3868
Black Oxide	3.22	0.7661	0.0012	3.2004	0.5868	-8.7646E+03	-1.1850E+05	4.8477

Table A9: Statistical parameters of IMF 5 at 900 rpm

Coating	R_a	*RMS*	*Skewness*	*Kurtosis*	*Variance*	*Shannon entropy*	*Log Energy*	*Crest Factor*
Nickel	0.29	0.3370	0.1015	5.9586	0.1136	8.7615E+03	-2.3380E+05	12.3622
Copper	0.52	0.6706	-0.0264	3.6641	0.4498	-1.1448E+03	-1.3942E+05	5.2673
ZnP	0.7	1.1693	-0.0070	3.4682	1.3673	-9.7949E+04	-6.4930E+04	4.4124
Silver	2.65	1.1386	-0.0061	7.0670	1.2963	-1.2383E+05	-9.5551E+04	6.9403
Black Oxide	3.22	1.0889	0.0049	3.0211	1.1856	-6.8900E+04	-7.1154E+04	3.9696

Table A10: Statistical parameters of IMF 6 at 900 rpm

Coating	R_a	*RMS*	*Skewness*	*Kurtosis*	*Variance*	*Shannon entropy*	*Log Energy*	*Crest Factor*
Nickel	0.29	0.4166	1.5007	13.0792	0.0409	1.3984E+04	-1.5236E+05	7.9615
Copper	0.52	0.3911	0.1627	6.6078	0.0184	1.6210E+04	-1.3994E+05	5.3252
ZnP	0.7	0.5358	-0.0536	3.2425	0.0254	1.9874E+04	-9.3626E+04	2.4888
Silver	2.65	0.5089	-0.0966	4.6351	0.0649	1.5848E+04	-1.2693E+05	4.1106
Black Oxide	3.22	0.4198	0.0147	3.1518	0.0471	1.4769E+04	-1.5891E+05	4.3824

Statistical parameters of non-responsive decomposed levels at 1200 rpm

Table A11: Statistical parameters of IMF 1 at 1200 rpm

Coating	R_a	*RMS*	*Skewness*	*Kurtosis*	*Variance*	*Shannon entropy*	*Log Energy*	*Crest Factor*
Nickel	0.29	0.4330	0.0057	12.4155	0.1875	1.2889E+03	-2.3882E+05	10.5572
Copper	0.52	1.7748	0.0085	9.7998	3.1500	-4.8774E+05	-3.4239E+04	11.0052
ZnP	0.7	0.8520	-0.0004	4.2549	0.7259	-2.6508E+04	-1.1140E+05	6.4216
Silver	2.65	0.9839	-0.0003	4.9368	0.9681	-5.7031E+04	-9.5149E+04	7.9734
Black Oxide	3.22	1.2065	0.0005	3.0620	1.4556	-1.0370E+05	-5.7202E+04	4.4453

Table A12: Statistical parameters of IMF 3 at 1200 rpm

Coating	R_a	*RMS*	*Skewness*	*Kurtosis*	*Variance*	*Shannon entropy*	*Log Energy*	*Crest Factor*
Nickel	0.29	0.5381	0.0300	9.0811	0.2896	-1.2651E+03	-1.9667E+05	10.3904
Copper	0.52	2.4898	-0.0008	3.6409	6.1994	-1.0482E+06	3.0774E+04	5.5239
ZnP	0.7	1.3905	-0.0002	4.0756	1.9329	-1.9191E+05	-4.9780E+04	6.0418
Silver	2.65	1.8589	0.0034	3.7271	3.4557	-4.5936E+05	-7.9692E+03	5.0248
Black Oxide	3.22	1.3036	0.0004	3.2562	1.6994	-1.4101E+05	-4.9610E+04	5.1265

Table A13: Statistical parameters of IMF 4 at 1200 rpm

Coating	R_a	*RMS*	*Skewness*	*Kurtosis*	*Variance*	*Shannon entropy*	*Log Energy*	*Crest Factor*
Nickel	0.29	0.5238	0.1122	11.8411	0.2744	-4.1184E+03	-2.1505E+05	11.5845
Copper	0.52	2.0225	-0.0004	3.8556	4.0906	-5.9990E+05	-2.5561E+03	4.6410
ZnP	0.7	2.3140	0.0002	3.3702	5.3530	-8.4965E+05	2.0682E+04	4.5203
Silver	2.65	1.1980	0.0037	3.5782	1.4353	-1.0797E+05	-6.3103E+04	5.1592
Black Oxide	3.22	1.9789	0.0021	3.1926	3.9162	-5.3390E+05	3.8002E+03	4.5121

Table A14: Statistical parameters of IMF 5 at 1200 rpm

Coating	R_a	*RMS*	*Skewness*	*Kurtosis*	*Variance*	*Shannon entropy*	*Log Energy*	*Crest Factor*
Nickel	0.29	0.8150	0.3335	11.2156	0.6642	-4.5793E+04	-1.5351E+05	11.5691
Copper	0.52	0.9525	-0.0358	3.5899	0.9072	-4.2671E+04	-9.5141E+04	5.1184
ZnP	0.7	2.1308	-0.0015	3.8945	4.5329	-6.9552E+05	4.2795E+03	4.5484
Silver	2.65	1.2332	0.0009	4.0125	1.5207	-1.2510E+05	-6.2066E+04	5.3837
Black Oxide	3.22	1.3277	-0.0028	3.0424	1.7628	-1.4683E+05	-4.5002E+04	5.1329

Table A15: Statistical parameters of IMF 6 at 1200 rpm

Coating	R_a	*RMS*	*Skewness*	*Kurtosis*	*Variance*	*Shannon entropy*	*Log Energy*	*Crest Factor*
Nickel	0.29	0.8575	2.4291	14.1941	0.6271	-6.3952E+04	-1.5579E+05	11.9742
Copper	0.52	0.4878	-0.0612	3.3297	0.0618	1.5625E+04	-1.3681E+05	3.7485
ZnP	0.7	1.7499	-0.0087	3.3997	3.0399	-3.7583E+05	-1.5434E+04	5.2416
Silver	2.65	0.5027	0.1068	4.4110	0.0580	1.6026E+04	-1.2934E+05	6.6959
Black Oxide	3.22	0.4698	-0.1220	3.1138	0.0957	1.3625E+04	-1.5993E+05	4.4289

Statistical parameters of non-responsive decomposed levels at 1500 rpm

Table A16: Statistical parameters of IMF 1 at 1500 rpm

Coating	*R_a*	*RMS*	*Skewness*	*Kurtosis*	*Variance*	*Shannon entropy*	*Log Energy*	*Crest Factor*
Nickel	0.29	0.7083	0.0013	15.4231	0.5017	-3.0447E+04	-1.7743E+05	12.0114
Copper	0.52	0.6199	0.0007	4.0150	0.3843	2.9707E+03	-1.4736E+05	7.1016
ZnP	0.7	0.5076	-0.0015	4.3418	0.2577	8.1509E+03	-1.7443E+05	9.0807
Silver	2.65	0.9778	-0.0001	7.3501	0.9560	-6.6939E+04	-1.0474E+05	8.4322
Black Oxide	3.22	1.9000	-0.0001	3.3097	3.6100	-4.7648E+05	-2.5721E+03	4.7725

Table A17: Statistical parameters of IMF 3 at 1500 rpm

Coating	*R_a*	*RMS*	*Skewness*	*Kurtosis*	*Variance*	*Shannon entropy*	*Log Energy*	*Crest Factor*
Nickel	0.29	0.8077	0.0022	5.7350	0.6524	-2.7283E+04	-1.3097E+05	7.7781
Copper	0.52	0.7612	0.0008	3.6447	0.5795	-1.0536E+04	-1.2280E+05	5.3458
ZnP	0.7	1.0191	0.0000	15.6397	1.0387	-1.1810E+05	-1.3489E+05	12.5102
Silver	2.65	1.4462	0.0003	8.5996	2.0916	-2.8401E+05	-7.8651E+04	8.6056
Black Oxide	3.22	2.3186	0.0008	3.6212	5.3759	-8.5431E+05	2.2130E+04	7.2312

Table A18: Statistical parameters of IMF 4 at 1500 rpm

Coating	*R_a*	*RMS*	*Skewness*	*Kurtosis*	*Variance*	*Shannon entropy*	*Log Energy*	*Crest Factor*
Nickel	0.29	0.6756	0.0000	10.3079	0.4565	-1.8855E+04	-1.7602E+05	9.5747
Copper	0.52	0.5902	-0.0203	4.3166	0.3484	4.2419E+03	-1.5602E+05	9.7947
ZnP	0.7	0.5209	-0.0035	6.2872	0.2713	4.0937E+03	-1.8157E+05	8.2720
Silver	2.65	0.7315	0.0003	8.4006	0.5350	-2.0947E+04	-1.4811E+05	10.8105
Black)xide	3.22	1.8171	0.0089	3.3125	3.3018	-4.1854E+05	-8.9574E+03	4.6152

Table A19: Statistical parameters of IMF 5 at 1500 rpm

Coating	*R_a*	*RMS*	*Skewness*	*Kurtosis*	*Variance*	*Shannon entropy*	*Log Energy*	*Crest Factor*
Nickel	0.29	0.7406	0.0275	3.7096	0.5485	-8.5981E+03	-1.2752E+05	5.7351
Copper	0.52	0.8921	-0.0096	3.9992	0.7958	-3.3231E+04	-1.0578E+05	5.5059
ZnP	0.7	0.7283	0.0037	3.6869	0.5305	-7.2233E+03	-1.3032E+05	5.0813
Silver	2.65	1.1487	-0.0027	4.2314	1.3196	-1.0252E+05	-7.8504E+04	5.2013
Black Oxide	3.22	1.4557	-0.0056	3.0946	2.1176	-2.0159E+05	-3.3216E+04	5.5974

Table A20: Statistical parameters of IMF 6 at 1500 rpm

Coating	R_a	*RMS*	*Skewness*	*Kurtosis*	*Variance*	*Shannon entropy*	*Log Energy*	*Crest Factor*
Nickel	0.29	0.5556	0.1939	3.2425	0.1262	1.1436E+04	-1.4626E+05	5.8755
Copper	0.52	0.5550	-0.1102	2.8872	0.0464	1.7960E+04	-1.0249E+05	2.2395
ZnP	0.7	0.5251	-0.1644	3.1573	0.0594	1.6633E+04	-1.2105E+05	3.1858
Silver	2.65	0.5553	0.0604	3.5011	0.1423	1.1197E+04	-1.4289E+05	4.2028
Black Oxide	3.22	0.8736	-0.0182	3.1412	0.7526	-2.3335E+04	-9.9639E+04	4.5335

Table A21:Frequency bands of responsive IMFs (surface roughness)

S. No	*RPM*	*Responsive IMF*	*Approximate Frequencies Band (Hz)*
1	300	None	None
2	600	6	0.0058-431
3	900	4	567-2100
4	1200	2	2250-4490
5	1500	2	3010-4590

Coating wise information of frequency bands and relative energy

Table A22: IMF wise frequency band and percentage of relative energy for nickel coated bearing at all speeds

Speed	**600 rpm**		**900 rpm**		**1200 rpm**		**1500 rpm**	
Modes gained by VMD	**Frequency Band (Hz)**	**Relative energy (%)**	**Frequency Band (Hz)**	**Relative energy (%)**	**Frequency Band (Hz)**	**Relative energy (%)**	**Frequency Band (Hz)**	**Relative energy (%)**
Mode1	4480-5400	2.02	4590-5430	6.78	4510-5390	7.87	4510-5370	16.30
Mode2	2930-3760	2.95	3180-4060	6.43	3110-3980	8.33	3010-3760	14.84
Mode3	1870-2650	5.12	2280-2960	10.71	2230-2900	12.15	2300-2880	21.20
Mode4	904-1540	7.08	1400-2080	10.34	1360-2020	11.51	1390-2030	17.09
Mode5	405-870	10.13	579-1070	25.52	607-1130	27.87	584-1140	17.83
Mode 6	0.00511-0.0972	71.86	0.00654-226	38.99	0.034-372	30.85	0.00846-325	10.03

Table A23: IMF wise frequency band and percentage of relative energy for copper coated bearing at all speeds

Speed	600 rpm		900 rpm		1200 rpm		1500 rpm	
Modes gained by VMD	Frequency Band (Hz)	Relative energy (%)	Frequency Band (Hz)	Relative energy (%)	Frequency Band (Hz)	Relative energy (%)	Frequency Band (Hz)	Relative energy (%)
Mode1	4680-5280	27.71	4530-5410	7.35	4560-5280	20.01	4790-5300	16.24
Mode2	1950-2400	26.81	2780-3620	5.46	2270-2830	6.55	3860-4590	9.45
Mode3	1510-1910	20.05	1800-2310	11.23	1880-2180	39.38	2130-2560	14.37
Mode4	905-1440	4.72	1270-1760	16.05	1450-1830	25.99	1860-2110	34.42
Mode5	479-824	7.72	685-1140	25.38	592-1190	5.76	1430-1780	18.28
Mode 6	0.00515-0.0978	8.93	0.00523-0.0994	32.84	0.00675-565	1.51	490-1130	4.62

Table A24: IMF wise frequency band and percentage of relative energy for zinc phosphate coated bearing at all speeds

Speed	600 rpm		900 rpm		1200 rpm		1500 rpm	
Modes gained by VMD	Frequency Band (Hz)	Relative energy (%)	Frequency Band (Hz)	Relative energy (%)	Frequency Band (Hz)	Relative energy (%)	Frequency Band (Hz)	Relative energy (%)
Mode1	2270-2910	10.12	2310-3030	6.54	3020-3690	4.30	2990-3610	5.68
Mode2	1490-1910	5.77	1520-1880	9.34	2250-2740	6.26	2280-2790	4.93
Mode3	1210-1420	33.19	1180-1430	23.27	1540-1940	11.45	1710-2000	12.39
Mode4	840-1030	31.23	844-1040	33.27	1210-1500	31.70	1390-1660	11.15
Mode5	400-710	10.68	576-786	21.16	862-1080	26.88	1140-1380	28.97
Mode 6	0.00528-101	7.37	0.00549-290	4.44	604-818	18.13	709-1030	35.68

Table A25: IMF wise frequency band and percentage of relative energy for silver coated bearing at all speeds

Speed	600 rpm		900 rpm		1200 rpm		1500 rpm	
Modes gained by VMD	Frequency Band (Hz)	Relative energy (%)	Frequency Band (Hz)	Relative energy (%)	Frequency Band (Hz)	Relative energy (%)	Frequency Band (Hz)	Relative energy (%)
Mode1	2310-2710	14.37	2280-2690	12.53	3080-5000	5.68	1640-2440	3.00
Mode2	1590-1770	30.73	1590-1790	31.98	2700-3380	7.56	1420-1640	10.76
Mode3	1390-1590	22.35	1410-1590	26.54	2150-2560	26.69	1160-1320	18.32
Mode4	892-1200	14.96	1070-1290	12.37	1400-1990	13.21	972-1110	28.41
Mode5	452-849	7.60	714-1030	13.23	813-1260	32.52	773-972	21.58
Mode 6	0.00524-0.0995	9.39	0.00667-375	2.64	0.00808-353	13.46	226-485	17.78

Table A26: IMF wise frequency band and percentage of relative energy for black oxide coated bearing at all speeds

Speed	600 rpm		900 rpm		1200 rpm		1500 rpm	
Modes gained by VMD	Frequency Band (Hz)	Relative energy (%)	Frequency Band (Hz)	Relative energy (%)	Frequency Band (Hz)	Relative energy (%)	Frequency Band (Hz)	Relative energy (%)
Mode1	4410-5330	8.11	4400-5280	11.58	4940-5560	13.53	4760-5510	15.27
Mode2	3160-4000	6.31	3270-4020	8.67	3970-4740	13.50	3690-4510	13.97
Mode3	2130-2830	9.03	2320-2990	11.33	2490-3280	15.80	2540-3160	22.75
Mode4	1580-2050	29.20	1630-2100	39.86	1700-2240	36.41	1760-2260	33.83
Mode5	783-1250	34.09	909-1290	22.88	924-1460	16.39	1050-1600	8.97
Mode 6	0.006-431	11.41	0.00682-575	3.40	0.00883-608	2.05	424-1040	3.23

List of Publications

S. No	Journal indexing (Scopus/ UGC/Web of Science)	Status of Paper	Journal Name	Title of the Paper	Volume, Issue Number & page number	ISSN Number, Impact Factor/SJR
1	Scopus	Published	Journal of Vibration Engineering & Technologies	Comparative analysis of wear resistance for bearing coating using VMD of Vibration Signal	https://doi.org/10.1007/s42417-024-01404-1	ISSN 2523-3939, 0.46
2	Scopus	Published	Physica Scripta	Comparative analysis of surface roughness level for bearing coating using VMD of vibration signal	Volume 99, Number 8	ISSN 1402-4896, 0.42
3	Scopus	Submitted	Engineering Research Express	Comparative analysis of grain size for bearing coating using VMD of vibration signal	Yet to be Issued	ISSN 2631-8695

List of Conferences

S. No.	Journal indexing (Scopus/ UGC/Web of Science)	Status of Paper	Journal Name	Title of the Paper	Volume, Issue Number & page number	ISSN Number, Impact Factor/SJR
1	Scopus	Published	Material Today Proceedings	To compare the effect of different level of self- lubrication for bearings using statistical analysis of vibration signal	Volume 5, Issue 14, Part 2	22147853, 0.445
2	Scopus	Published	Material Today Proceedings	Comparison of roughness level in ball bearing using statistical analysis of vibration signal	Volume 47, Part 17	22147853, 0.445
3	Scopus	Published	AIP Conference Proceedings	A Study on Properties of Bearing Coatings and their Degradation Measurement: Challenges and Solutions	Volume 2800, Issue 1	020103, 0.164
4	Scopus	Published	AIP Conference Proceedings	Analysis of Different Coatings for Properties on Ball Bearing Using Vibration Signal	Volume 2962, Issue 1	020044, 0.164